Kimmo Kerkkänen

DYNAMIC ANALYSIS OF BELT-DRIVES USING THE ABSOLUTE NODAL COORDINATE FORMULATION

Thesis for the degree of Doctor of Science (Technology) to be presented with due permission for public examination and criticism in the auditorium 1381 at Lappeenranta University of Technology, Lappeenranta, Finland on the 28th of April, 2006, at noon.

Acta Universitatis
Lappeenrantaensis
238

Supervisor
Professor Aki Mikkola
Department of Mechanical Engineering
Lappeenranta University of Technology
Finland

Reviewers
Dr. Oleg Dmitrochenko
Department of Mechanical Engineering
University of Illinois at Chicago
USA

Professor Nobuyuki Kobayashi
Department of Mechanical Engineering
Aoyama Gakuin University
Japan

Opponents
Dr. Oleg Dmitrochenko
Department of Mechanical Engineering
University of Illinois at Chicago
USA

Professor Emeritus Eero-Matti Salonen
Department of Engineering Physics and Mathematics
Helsinki University of Technology
Finland

ISBN 952-214-193-3
ISBN 952-214-194-1 (PDF)
ISSN 1456-4491

Lappeenrannan teknillinen yliopisto
Digipaino 2006

ABSTRACT

Kimmo Kerkkänen

Dynamic analysis of belt-drives using the absolute nodal coordinate formulation

Lappeenranta 2006

121 p.

Acta Universitatis Lappeenrantaensis 238

Diss. Lappeenranta University of Technology

ISBN 952-214-193-3, ISBN 952-214-194-1 (PDF), ISSN 1456-4491

Belt-drive systems have been and still are the most commonly used power transmission form in various applications of different scale and use. The peculiar features of the dynamics of the belt-drives include highly nonlinear deformation, large rigid body motion, a dynamical contact through a dry friction interface between the belt and pulleys with sticking and slipping zones, cyclic tension of the belt during the operation and creeping of the belt against the pulleys. The life of the belt-drive is critically related on these features, and therefore, a model which can be used to study the correlations between the initial values and the responses of the belt-drives is a valuable source of information for the development process of the belt-drives.

Traditionally, the finite element models of the belt-drives consist of a large number of elements that may lead to computational inefficiency. In this research, the beneficial features of the absolute nodal coordinate formulation are utilized in the modeling of the belt-drives in order to fulfill the following requirements for the successful and efficient analysis of the belt-drive systems: the exact modeling of the rigid body inertia during an arbitrary rigid body motion, the consideration of the effect of the shear deformation, the exact description of the highly nonlinear deformations and a simple and realistic description of the contact.

The use of distributed contact forces and high order beam and plate elements based on the absolute nodal coordinate formulation are applied to the modeling of the belt-drives in two- and three-dimensional cases. According to the numerical results, a realistic behavior of the belt-drives can be obtained with a significantly smaller number of elements and degrees of freedom in comparison to the previously published finite element models of belt-drives. The results of the examples demonstrate the functionality and suitability of the absolute nodal coordinate formulation for the computationally efficient and realistic modeling of belt-drives.

This study also introduces an approach to avoid the problems related to the use of the continuum mechanics approach in the definition of elastic forces on the absolute nodal coordinate formulation. This approach is applied to a new computationally efficient two-dimensional shear deformable beam element based on the absolute nodal coordinate formulation. The proposed beam element uses a linear displacement field neglecting higher-order terms and a reduced number of nodal coordinates, which leads to fewer degrees of freedom in a finite element.

Keywords: Belt-drive, finite element, flexible multibody dynamics, multibody application

UDC 621.852 : 531.391.1 : 519.62/.64 : 51.001.57 : 004.942

ACKNOWLEDGEMENTS

The research work of this thesis has been carried out during the years 2003…2005 in the Institute of Mechatronics and Virtual Engineering at the Department of Mechanical Engineering of Lappeenranta University of Technology. The studies introduced in this thesis are part of a larger research project financed by the Academy of Finland and partly by the National Technology Agency of Finland (TEKES).

It is my pleasure to express a deep gratitude to the several persons related to the years spent at the university as a researcher: To my supervisor, Professor Aki Mikkola for your extremely valuable, constant and inexhaustible support and encouragement while guiding me to the world of virtual engineering. To the members of our researcher team, Dr. Jussi Sopanen, Dr. Kari Dufva and M.Sc. Marko Matikainen, for your amazing and respectable dedication to the work, from which I time to time became motivated or anguished. To Dr. Daniel García-Vallejo from University of Seville, for the fruitful co-operation and for the uncompromising and educational attitude to the science. You all made this possible. I would also like to thank the whole personnel of the department and an excellent translator Tiina Kauranen for your effect to the intelligibility of the language of the thesis.

The reviewers Dr. Oleg Dmitrochenko from the University of Illinois at Chicago and Professor Nobuyuki Kobayashi from the Aoyama Gakuin University are warmly and gratefully remembered for their careful attitude to the review process and for many insightful and constructive comments and advices.

A great appreciation for the financial encouragement is deserved by the Research Foundation of Lappeenranta University of Technology, South Carelian Regional fund of Finnish Cultural Foundation, Foundation of Jenny and Antti Wihuri, Foundation of Lahja and Lauri Hotinen and City of Lappeenranta.

Outi, my dearest. It is an undeserved delight and honor to share the life with you. Thank you for everything you are. My parents and parents-in-law, there are many features in you I would like to see in me. You have given me many valuable tools for the studies and life, thank you for them. All my unique, widely talented and mirthful friends, without you I would not be me. The multiform activities with you were an essential source of the energy required to complete this work. It is an indescribable joy and privilege to have friends like you.

In the future working life, my dream is not only to use my brains, but also my heart.

This thesis is dedicated to my wife Outi, to my parents Elma and Alpo, to my parents-in-law Liisa and Matti and finally to the most thrilling place on the Earth, the Jänisjoki River in Tohmajärvi.

Lappeenranta, 17th of March 2006 Kimmo Kerkkänen

CONTENTS

NOMENCLATURE

Abbreviations

ANCF	Absolute Nodal Coordinate Formulation
CPU	Central Processing Unit

Symbols

$a_0, \ldots, a_5$	polynomial coefficients
A	area of the element cross-section
$\mathbf{A}_\psi$	transformation matrix due to the rotation of the centerline
$\mathbf{A}_\gamma$	transformation matrix due to the shear deformation
$b_0, \ldots, b_5$	polynomial coefficients
$\mathbf{b}_\psi$	unit vector perpendicular to the element centerline and to vector $\mathbf{n}_\psi$
c	constant of integration
c_p	damping coefficient per unit length of the penalty force
C^m	continuity on shape functions and their derivates up to order m
$\mathbf{C}$	vector of linearly independent constraint equations
$\mathbf{C}_\mathbf{e}$	Jacobian matrix
d	penetration between contact surfaces
$\mathbf{D}$	deformation gradient
$\bar{\mathbf{D}}$	gradient of the displacement vector
$e_1, \ldots, e_{12}$	nodal coordinates
$\mathbf{e}$	vector of the nodal coordinates
E	Young’s modulus
$\mathbf{E}$	matrix of elastic coefficients of the material
$\mathbf{f}_n$	distributed normal contact force
$\mathbf{f}_t$	distributed tangential contact force
F	force applied to a node

F_n	force per unit length in the normal direction
F_t	force per unit length in the tangential direction
g	gravity
G	shear modulus *or* mass flow rate
h	height of the beam in the initial configuration *or* thickness of the plate element
i	integer coefficient
I	node I *or* mass moment of inertia
$\mathbf{I}$	identity matrix
$\tilde{\mathbf{I}}$	skew symmetric matrix of the identity matrix
J	node J
$\mathbf{J}$	gradient of the position vector
$\mathbf{J}_0$	constant transformation matrix
k	elastic modulus with units of force *or* absolute value of the curvature
k_p	stiffness coefficient per unit length of the penalty force
k_s	shear correction factor
l	length of the beam or element in the initial configuration
l_{belt}	length of the belt in the initial configuration
l_{s}	span length
m	mass of the structure
M	moment load
$\mathbf{M}$	mass matrix
n	number of elements
$\mathbf{n}$	unit normal vector at the contact surface
$\mathbf{n}_{\psi}$	unit vector perpendicular to the element centerline
$\mathbf{N}$	vector that defines the position of a contact point on the element
O_i	center location of the pulley i
P	arbitrary particle
$\mathbf{p}$	unit vector along the pulley axis
q	shear force
$\mathbf{q}$	vector of the generalized coordinates

$\mathbf{Q}$	vector of the generalized forces
$\mathbf{Q}_c$	vector of the generalized contact forces
$\mathbf{Q}_d$	vector that arises by differentiating the constraint equations twice with respect to time
$\mathbf{Q}_e$	vector of the generalized elastic forces
$\mathbf{Q}_k$	vector of the generalized external forces
$\mathbf{Q}_r$	vector of the generalized rigid body forces
$\mathbf{r}$	global location of an arbitrary particle
$\mathbf{r}_c$	global location of the centerline of the element
$\mathbf{r}_O$	global location of the center of the pulley
$\mathbf{r}_s$	vector that defines the orientation of the cross-section of the element
R_i	radius of circular constraint *i*
s	location of a portion of the belt.
$S_1, \ldots, S_6$	shape functions
$\mathbf{S}$	element shape function matrix
$\mathbf{S}_0$	element shape function matrix evaluated at the centerline of the element
t	time
$\mathbf{t}$	unit tangent vector at the contact surface
$\mathbf{t}_o$	unit vector along the length of an infinitesimal portion of the belt
$\mathbf{t}_\psi$	unit tangent vector at the element centerline
T	kinetic energy *or* axial strain
T_a	opposing torque
T_s	acceleration time
u	displacement of the driving pulley
u_x	beam axial extension
$\mathbf{u}$	displacement vector
U	strain energy
U^ε	strain energy due to axial elongation of element
U^κ	strain energy function due to bending stiffness
v	velocity *or* speed

v_s	slope of the creep-rate dependent friction curve
v_t	relative tangential velocity
$\mathbf{v}$	vector contained in the cross-section of the element *or* velocity vector
V	volume of the element *or* potential energy
w	width of the element in the initial configuration *or* vertical displacement
δW	virtual work of the contact forces
x	local coordinate
X	global coordinate
$\mathbf{x}$	vector of the local coordinates
y	local coordinate
Y	global coordinate
z	local coordinate
Z	global coordinate

Greek Letters

α_1	axial stiffness parameter
α_2	bending stiffness parameter
β_i	angular displacement of pulley *i or* angle
γ	shear angle
ε	Green strain
ε^A	Almansi strain
ε_{xx}^a	axial strain component
ε_l	elongation of the centerline of the element
ε_{xx}^m	normal strain in *x*-direction
ε_{yy}^m	normal strain in *y*-direction
ε_{xy}^m	normal strain in *xy*-plane
ε^t	true strain
$\boldsymbol{\varepsilon}$	vector of three components of Green Lagrange strain tensor

$\boldsymbol{\varepsilon}^{e}$	Eulerian or Almansi strain tensor
$\boldsymbol{\varepsilon}^{lin}$	strain tensor of linear strain-displacement relationship
$\boldsymbol{\varepsilon}^{m}$	Green Lagrange strain tensor
ζ	non-dimensional quantity
η	non-dimensional quantity
θ	rotational degree of freedom *or* angular displacement *or* bending angle of a portion of the element
$\ddot{\theta}$	angular acceleration
κ	curvature
λ	Lame's constant
$\boldsymbol{\lambda}$	vector of Lagrange multipliers
μ	Lame's constant *or* friction coefficient
ν	Poisson's ratio
ξ	non-dimensional quantity
ρ	material density
ω	angular velocity
ω_{driver}	angular velocity of the driver pulley
ω_{driven}	angular velocity of the driven pulley
ω_{S}	steady state angular velocity

Subscripts and superscripts

$A,\ldots,D$	nodes of the plate element
e	absolute nodal coordinate
I	node I
J	node J
n	node *or* normal direction
o	reference state
p	pulley
P	particle P

q	partial derivative with respect to generalized coordinates
r	rigid body coordinate *or* rigid body
t	differentiation with respect time *or* tangential direction
T	transposition of vector or matrix
x	partial derivative with respect to *x or* local coordinate
y	partial derivative with respect to *y or* local coordinate
z	local coordinate

1 INTRODUCTION

The structurally and materially versatile selection of belt-drives has been used for more than 200 years to transmit power between rotational machine elements. Belt-drives are still being used in various ranges of applications including domestic appliances as well as automotive technology, Figure 1.1, due to the following advantages in comparison to alternative forms of power transmission: low price, quietness, cleanliness, no requirements for lubrication, absorption of shock loads, wide selection of speed ratios, small power loss, simple installation and maintenance, possibility for relatively long distances between driver and driven shafts and visual warning of failure. These mechanical systems involve pulleys and belts, Figure 1.2, which dynamically contact each other through a dry friction interface. The tension of the belt transitions ranges from low to high and *vice versa* during the operation. The life of the belt-drive depends critically on the tension magnitudes in the belt spans. Another significant factor in the life of the belt-drive is the sliding wear of the belt caused by creeping against the pulley. In the long run, this wear may deteriorate the surface of the belt leading to changes in the friction characteristics of the belt. As a result, noisy operation and other problems may occur. For these reasons, a detailed and computationally efficient model of the belt-drive, which is capable of accurately predicting the belt dynamics and the contribution of the contact forces between the belt and pulley, is beneficial in the product development process.

Figure 1.1 Examples of belt-drive applications.

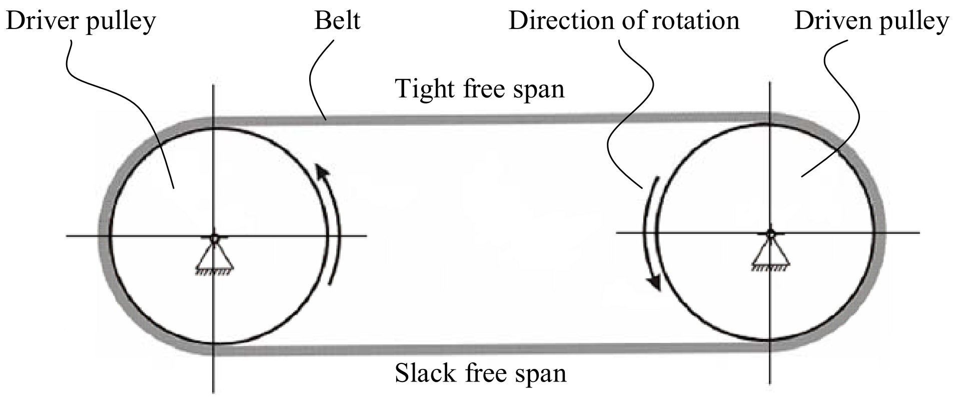

Figure 1.2 Sketch of a simple belt-drive structure.

The traditional research of belt-drives can be divided into belt-drive mechanics studies and dynamic response studies of serpentine belt-drives used for front-end accessory drives in the automotive industry as suggested by Leamy and Wasfy [1]. The studies of belt mechanics can be further subcategorized to be based on the traditional creep theory or the shear theory [2]. In the creep theory, the belt is assumed to be elastically extensible and the frictional forces due to slip motion are determined by a Coulomb law. In the shear theory, the belt is modeled as inextensible adopting shear deformation. According to Alciatore *et al*. [2], the creep theory can be applied to homogenous belts such as leather flat belts, while the shear theory applies to steel-reinforced belts such as the most standard V-belts.

An extensive review of the belt-drive mechanics is given by Fawcett [3] while the classical creep theory is reviewed by Johnson [4]. The inclusion of belt inertia for the string model with creep theory is introduced by Bechtel *et al*. [5]. During the past three decades, many authors have contributed to the theory of belt-drive mechanics including, for example, studies of the belt shear effects [6], radial compliance effects [6] and the power loss expression [7]. In Reference [8] the effect of belt velocity on normal and tangential belt forces and centrifugal forces on belt tension is studied by Kim and Marshek. In the study, it is analytically shown that the effective belt tension decreases if belt velocity is increased and the distribution of the normal and tangential forces is dependent on belt velocity. In Reference [9] Kim and Marshek and in Reference [10] Kim *et al*. studied a concentrated force applied to the pulley and the friction characteristics for a concentrated load for a flat belt drive. In the studies of References [9, 10], it is shown by analytical and experimental results that the use of a varying coefficient of friction gives more accurate results than the use of the Euler formula about the ratio for tight and slack side tensions of the belt sliding against the pulley with a constant coefficient of friction. The changes of normal and tangential forces are found to be approximately linear rather than exponential as predicted by Euler's equation. The dynamic response of automotive serpentine belt-drives to crankshaft excitation has been researched in many analytical and numerical studies during the past fifteen years. These studies mainly concern the rotational response of the pulleys and the transverse response of the axially moving string-like belt with a simplified description of the belt-pulley contact [11…16]. Kong and Parker [17, 18] extended these studies by modeling the belt as a moving beam with bending stiffness enabling the study of the effects of design variables on belt-pulley coupling.

Kong and Parker modeled the belt as a moving Euler-Bernoulli beam including bending stiffness, elastic extension, Coulomb friction and belt inertia while excluding rotary inertia and shear deformation [19]. According to the results of Kong and Parker, for thick and low tension belts the role of bending stiffness should not be neglected due to its significant effect on wrap angles, power efficiency, the span tensions and the maximum transmissible moment on the steady motion of the belt.

According to the authors of Reference [1], belt-drive mechanics studies have not often considered the dynamic excitation while the frictional belt-pulley modeling in the serpentine belt-drive studies has been typically idealized. As a result, the connection between belt-drive mechanics and the dynamic response of serpentine belt-drives has been weak due to the nature of the modeling methods. The problem has been studied by Leamy *et al.* in References. [20…22], where the simplified dynamic models for low and high rotational speeds are introduced. In Reference [1] Leamy and Wasfy have proposed a general dynamic finite element model of belt-drive systems. In the study, the flat belt is modeled using truss elements including detailed frictional contact [1, 23]. The finite elements use only Cartesian coordinates of the nodes as degrees of freedom, and all degrees of freedom are defined directly in a global inertial reference frame. The contact forces are applied only at the nodes leading to a large number of degrees of freedom when the accurate representation of the circular boundaries of the pulleys is considered. The equations of motion are formulated using a total Lagrangian formulation. The effect of bending stiffness on the dynamic and steady state responses of belt-drives can be accounted for using three node beam elements based on the torsional-spring formulation [24, 25]. The authors of References [1, 23, 25] demonstrate that the results of the proposed models and analytical values are in good agreement for discretizations with 38 three node beam elements, 154 degrees of freedom, or 100 truss elements, 202 degrees of freedom, per half pulley.

The analysis of the angular velocity loss of a flat belt system is presented in Reference [26] by Chen and Shieh. The three dimensional finite element procedure of Reference [27] is modified in order to model the flexibility of the belt in a more convenient way leading to more accurate prediction of the angular velocity loss. The tension and rubber layers of the belt are modeled using three-dimensional two-node bar and eight-node brick elements, respectively. The model used in the analyses included 480 brick and 180 bar elements. By this combination, the angular velocity loss with different values of the dynamic friction coefficient, traction coefficient and material properties, such as the shear modulus of the rubber layer and the strain stiffness of the tension member, is studied in detail.

A finite element model of the belt-drive with a V-ribbed belt is introduced by Yu *et al.* [28] where the mechanics of contact between a belt rib and pulley groove with a composite, hyper elastic material model is studied. In the study, the composite material is implemented by dividing the cross-section of the rib into six elements of different material properties. The work cycle of the belt-drive is limited to a rotation of 180 degrees, which enables the use of a longer length for the elements in the free strands between the pulleys and a shorter length for the elements which could be in contact with the pulley groove. Using this modeling approach, nonlinear strain-displacement relationship can be omitted. The inclusion of contact is determined using an overlap criterion for the nodes of special interface elements, which are attached to the shorter elements. The belt of a total length of 754 mm includes 60 longer and 1560 shorter eight-node brick elements and 1040 interface elements. The model is particularly used to figure out the patterns of sticking and slipping between the belt and pulleys in entry and exit regions.

Three-dimensional finite element studies of frictional contact for flat and V-belt transmission systems are carried out by Shieh and Chen [27]. In the study, the belt consists of a composite structure where in the case of a flat belt a tension member is between a top rubber cover and a rubber layer, and in a V-belt the tension member is inside the rubber layer. In the development of the used finite element technique, Shieh and Chen have utilized a special transformation matrix that enables the mismatching of contact nodes and decreasing of system unknowns. In addition, the incremental Wilson displacement modes [29] are used to improve the accuracy of low-order eight-node brick elements, which originally can be inadequate in pure bending. According to the study, these features improve the accuracy of the contact forces especially at the inlet and exit regions of the contact area. The belt of a total length of 987 mm is analyzed using a quadrant of the belt due to the symmetry of geometry leading to 304 (flat belt) and 960 (V-belt) brick elements. The analysis is carried out using the classical Coulomb's frictional law, and the effect of friction coefficients on the contact forces and the deformation of the cross-section of the V-belt are studied. In Reference [30] the centrifugal force term is included in the finite element procedure introduced in Reference [27] for studying the effect of angular velocity on frictional contact forces of the V-belt drive system. In addition, the results related to the deformation of the V-belt and the relationship between the distribution of friction angles and a dynamic friction coefficient are presented.

References [2, 5, 7, 8, 16, 18, 19] include analytical studies of the belt-drives, References [9, 10, 11, 12, 13] consist of both analytical and experimental studies, Reference [14] includes numerical, analytical and experimental studies, References [24, 28] include numerical and experimental studies, numerical and analytical studies are presented in References [6, 17, 20, 23] while References [1, 15, 25, 26, 27, 30] consider the issue only from the numerical point of view.

1.1 Scope of the Work and Outline of the Dissertation

The objectives of this study are to develop a computationally efficient two-dimensional shear deformable beam element based on the absolute nodal coordinate formulation and find out the applicability of the absolute nodal coordinate formulation to modeling belt-drive systems as two-and three-dimensional cases. In the studies of belt-drives, the main objective is the satisfaction of the following requirements: Exact modeling of the rigid body motion resulting in zero strains. This requirement is due to the fact that a piece of the belt, i.e. an element undergoes large relative translation and rotations. The effect of the shear deformation must be considered as pointed out in Reference [6]. The third requirement is related to the description of highly nonlinear deformations that have to be described in order to obtain a reasonable number of elements in the model. The last essential requirement for the formulation used to model belt-drive systems is a simple and effective description of the contact between the belt and the pulleys [31].

It is shown in Chapter 2 that the use of continuum mechanics with higher order elements leads to computationally inappropriate results. For this reason, a new computationally efficient two-dimensional shear deformable beam element that is based on the use of the linear interpolation with the absolute nodal coordinate formulation is introduced in Chapter 2.

In Chapter 3, a two-dimensional belt-drive system is introduced by using the distributed contact forces and high order belt-like elements based on the absolute nodal coordinate formulation. It is shown by numerical examples in Chapter 3 that with the contributions to the contact model shown in this study, there is no need to use a high number of nodes for realistic representation of the boundary of the pulley, and the realistic behavior of the belt-drives can be obtained with a significantly smaller number of degrees of freedom in comparison to the previously published finite element models of belt-drives.

Chapter 4 presents more general formulations for the nonlinear dynamic finite element analysis of belt-drives by presenting three dimensional finite element absolute nodal coordinate beam and plate elements, which are applicable for the modeling of the belt-drives. The plate element is based on a thin plate theory and it provides additional degrees of freedom that may be important in the future in the study of three-dimensional dynamics phenomena. Bending stiffness can be varied in the element formulations, thereby allowing studying the effect of bending on the nonlinear dynamics of the belt-drive system. In Chapter 4, an analytical formulation for the belt drive with the assumptions is also discussed, and the finite element solution using the plate elements is compared with the solution obtained using a simplified analytical technique.

1.2 Contribution of the Dissertation

The following original contributions are introduced in this dissertation:

1. In this study, a new two-dimensional shear deformable beam element based on the absolute nodal coordinate formulation is proposed. Linear polynomials are used to interpolate both the transverse and longitudinal components of the displacement, which is different from other absolute nodal coordinate based beam elements where cubic polynomials are used in the longitudinal direction. The phenomenon known as shear locking is avoided through the adoption of selective integration within the numerical integration method. As shown in this study, accurate linear and nonlinear static deformations, as well as realistic dynamic behavior including the capturing of the centrifugal stiffening effect, can be achieved with a smaller computational effort by using the proposed element than by using existing shear deformable two-dimensional beam elements.

2. This study introduces a novel method to model belt-drive systems by utilizing the considerable useful features of the distributed contact forces and high order belt-like elements based on the absolute nodal coordinate formulation. The requirements for the successful and efficient analysis of the belt-drive system including the exact modeling of the rigid body inertia during an arbitrary rigid body motion, the consideration of the effect of the shear deformation, the exact description of the highly nonlinear deformations and a simple and realistic description of the contact are fulfilled by the methods presented in this study. With the contributions to the contact model shown in this study, there is no need to use a high number of nodes for realistic representation of the boundary of the pulley and the realistic behavior of the belt-drives can be obtained with a significantly smaller number of degrees of freedom in comparison to the previously published finite element models of belt-drives.

The original scientific contributions have been or will be published in the following research papers:

1. Kerkkänen, K. S., Sopanen, J. T., and Mikkola, A. M., 2005, “A Linear Beam Finite Element Based on the Absolute Nodal Coordinate Formulation", *Journal of Mechanical Design*, **127**, pp. 621-630.

2. Kerkkänen, K. S., García-Vallejo, D., and Mikkola, A. M., 2006, ”Modeling of Belt-Drives Using a Large Deformation Finite Element Formulation”, *Nonlinear Dynamics*, **43**, pp. 239-256.

3. Dufva, K. E., Kerkkänen, K. S., Maqueda, L., and Shabana, A. A., “Nonlinear Dynamics of Three-Dimensional Belt-Drives Using the Finite Element Method”, *Nonlinear Dynamics*, in review.

2 ABSOLUTE NODAL COORDINATE FORMULATION

The description of nonlinear deformations is a challenging and frequently studied research topic in the area of multibody dynamics. The goal of these studies is to obtain more realistic simulation models for applications such as belts and cables. Nonlinear deformation in multibody dynamics can be treated using, for example, the absolute nodal coordinate formulation [32…34] or the large rotation vector formulation [35]. The absolute nodal coordinate formulation has many advantages, which include the exact description of an arbitrary rigid body motion, a constant mass matrix and a capability of modeling nonlinear deformations. The most distinctive feature of the formulation is that slopes, i.e. position gradient coordinates, and displacements are used as the nodal coordinates instead of finite or infinitesimal rotations. The effect of the shear deformation was included in the absolute nodal coordinate formulation first by Omar and Shabana [36]. The absolute nodal coordinate formulation has been successfully applied to three-dimensional beams [37, 38] and shells [39]. Despite numerous studies into the usability and accuracy of the absolute nodal coordinate formulation [40, 41] its accuracy and appropriateness studies are still under way.

When using the absolute nodal coordinate formulation, the elastic forces can be obtained using either a continuum mechanics approach [38] or by employing a local element coordinate system [42]. Use of the continuum mechanics approach with the nonlinear strain-displacement relationship gives a much simpler and general expression for the elastic forces than use of the element local coordinate system and the linear strain-displacement relationship [36]. However, if the continuum mechanics approach is applied to higher order elements in the absolute nodal coordinate formulation, some problems, as stated by Sopanen and Mikkola [41] and García-Vallejo, Mikkola and Escalona [43], may exist. These problems are Poisson's locking due to the residual transverse normal stresses in bending, curvature thickness locking due to the element shrinking in bending, shear locking due to the element's inability to describe constant shear strain if the bending moment is linearly varied, and inaccurate description of bending. The first three of these phenomena can be seen as a prediction of overly stiff bending behavior of the element. In addition, despite the use of a cubic polynomial along x, the bending moment distribution along the longitudinal coordinate x is constant [44]. This observation demonstrates that the element has the feature of exhibiting linear bending behavior and it is useless and computationally wasteful to use the interpolation polynomials of a different order for different directions with the continuum mechanics approach. The term linear bending behavior refers in this study to the fact the bending moment distribution along the longitudinal coordinate of the beam is constant as in the beam element that uses linear interpolation polynomials.

As pointed out by Hughes [45], elements that are based on theories which accommodate transverse shear strain and require only C^0 –continuity are increasingly being favored over elements that require C^1 –continuity. The reason for this is clear: the demand for C^1 –continuity generally leads to more complicated formulations and consequently to inefficient computation. Particularly, it is not wise to use elements requiring C^1 –continuity if they behave similarly to elements requiring only C^0 –continuity. Therefore, this study focuses on shear deformable formulations, such as the Timoshenko beam, which require only C^0 –continuity for shape functions. Based on these features, it is natural to use linear interpolation.

In order to obtain a computationally more appropriate element for the absolute nodal coordinate formulation, this study proposes a simplified linear element. The better efficiency of the proposed element as compared to the previously introduced absolute nodal coordinate finite elements [34, 36] is achieved by simpler implementation due to the use of linear interpolation polynomials and a reduced amount of slope coordinates. The smaller number of nodal coordinates leads to reduced degrees of freedom in the finite element leading to computational advantages in structural analysis.

It is important to note that beam element formulations that omit shear deformation, such as the Bernoulli beam, often employ curvature in the description of elastic forces. These formulations use derivations of the displacement field in the description of rotational deformation. In such cases linear interpolation will lead to difficulties in the moment description. On the other hand, beam formulations that account for shear deformation, such as the Timoshenko beam, are not based on the curvature in the description of rotational deformation. Instead, rotational deformation is described by a rotational coordinate that is interpolated in the element. In this case the rotational coordinate is independent from the position description. The proposed element does not employ the curvature in the calculations of elastic forces and, accordingly, the proposed linear element is able to carry bending loading.

In the following, a continuum mechanics based element is briefly reviewed in order to shed light on the proposed element.

2.1 Continuum Mechanics Based Elements in the Absolute Nodal Coordinate Formulation

Using the absolute nodal coordinate formulation, the global position vector **r** of an arbitrary particle in a planar element, shown in Figure 2.1, can be written as

$$\mathbf{r} = \mathbf{S}(x, y)\mathbf{e}, \tag{2.1}$$

where **S** is the element shape function matrix, *x* and *y* are the local coordinates of the element and **e** is the vector of the nodal coordinates. Due to the use of local parameterization, the *x* coordinate is associated to the longitudinal axis of the element and the *y* coordinate to the transversal axis of the element.

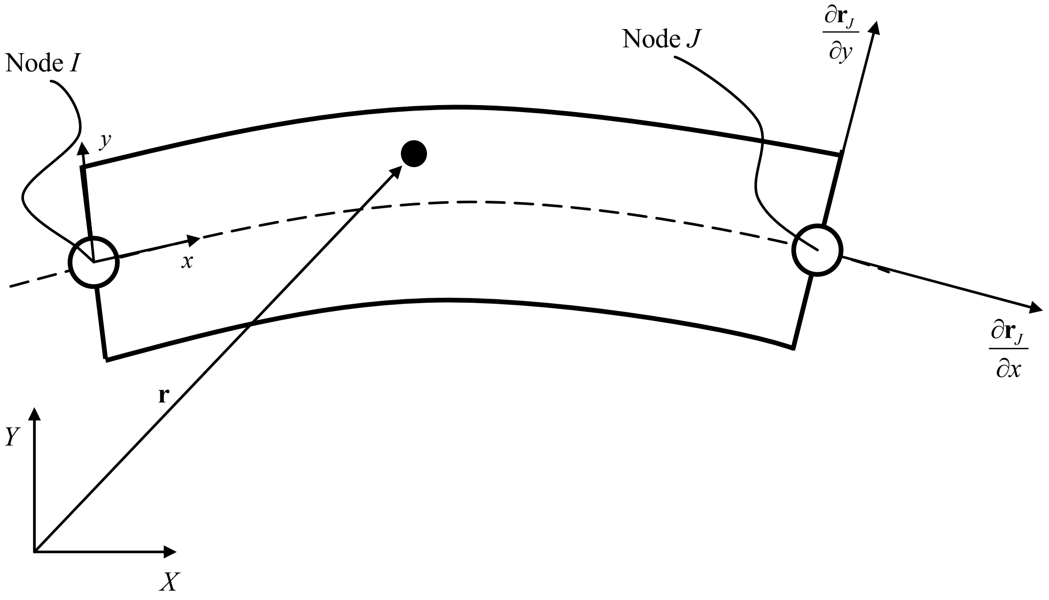

Figure 2.1 Description of a particle in the absolute nodal coordinate formulation.

The assumed displacement field of the existing two-dimensional shear deformable element proposed by Omar and Shabana can be defined in a global coordinate system by using the following polynomial expression [36]:

$$\mathbf{r} = \begin{bmatrix} r_1 \\ r_2 \end{bmatrix} = \begin{bmatrix} a_0 + a_1 x + a_2 y + a_3 xy + a_4 x^2 + a_5 x^3 \\ b_0 + b_1 x + b_2 y + b_3 xy + b_4 x^2 + b_5 x^3 \end{bmatrix}. \tag{2.2}$$

As can be seen from Equation (2.2), there is a cubic interpolation polynomial in the longitudinal direction and it includes 12 unknown polynomial coefficients. Consequently, six nodal coordinates are needed for each node of a two-noded (*I, J*) beam element. In this case the nodal coordinates $\mathbf{e}_I$, can be written as

$$\mathbf{e}_I = \begin{bmatrix} \mathbf{r}_I^T & \dfrac{\partial \mathbf{r}_I^T}{\partial x} & \dfrac{\partial \mathbf{r}_I^T}{\partial y} \end{bmatrix}^T , \tag{2.3}$$

where $\mathbf{r}_I$ is the global position vector of node *I* and vectors $\partial \mathbf{r}_I^T / \partial x$ and $\partial \mathbf{r}_I^T / \partial y$ are the slopes of node *I*. As illustrated in Figure 2.1, vector $\partial \mathbf{r}_J^T / \partial x$ defines the global orientation of the centerline of the beam, and vector $\partial \mathbf{r}_J^T / \partial y$ defines the orientation of the height coordinate of the cross-section of the beam [36], [41].

To prove that the element of Omar and Shabana [36] has the feature of exhibiting linear bending behavior, i.e. constant bending moment distribution along the longitudinal coordinate, the strain distributions in the beam element are studied using cubic interpolation polynomials along the longitudinal coordinate. In this example, only linear strain components are studied. It is important to note, however, that adding the nonlinear components for strain expressions does not solve the inherit problem related to element formulation proposed by Omar and Shabana. The strains can be defined using the deformation gradient $\mathbf{D}$ or the displacement vector gradient $\bar{\mathbf{D}}$. By assuming that the element is initially straight and coincident with the global coordinate system, the displacement gradient can be written as follows:

$$\bar{\mathbf{D}} = \frac{\partial \mathbf{u}}{\partial \mathbf{x}}, \tag{2.4}$$

where the local coordinate vector $\mathbf{x} = \begin{bmatrix} x & y \end{bmatrix}^T$ and the displacement vector $\mathbf{u}$ is defined as:

$$\mathbf{u} = \mathbf{r} - \begin{bmatrix} x & y \end{bmatrix}^T. \tag{2.5}$$

The strain tensor that describes the linear strain-displacement relationship can be written as follows:

$$\boldsymbol{\varepsilon}^{lin} = \frac{1}{2}\left(\bar{\mathbf{D}}^T + \bar{\mathbf{D}}\right). \tag{2.6}$$

Note that the nonlinear terms, i.e. the second order terms, would be insignificant in the case of small deformations. The strain tensor of $\boldsymbol{\varepsilon}^{lin}$ is symmetric, and therefore, only three strain components are needed for identification. Components for linear strain terms can be written in vector form as

$$\boldsymbol{\varepsilon}^{lin} = \begin{bmatrix} \varepsilon_{xx}^{lin} & \varepsilon_{yy}^{lin} & 2\varepsilon_{xy}^{lin} \end{bmatrix}^T. \tag{2.7}$$

By using the shape functions of Omar and Shabana [36] and the nodal coordinate vector $\mathbf{e}$, which can be written for a two-node two-dimensional beam element as

$$\mathbf{e} = \begin{bmatrix} \mathbf{e}_I{}^T & \mathbf{e}_J{}^T \end{bmatrix}^T = \begin{bmatrix} \mathbf{r}_I^T & \dfrac{\partial \mathbf{r}_I^T}{\partial x} & \dfrac{\partial \mathbf{r}_I^T}{\partial y} & \mathbf{r}_J^T & \dfrac{\partial \mathbf{r}_J^T}{\partial x} & \dfrac{\partial \mathbf{r}_J^T}{\partial y} \end{bmatrix}^T = \left[e_1, e_2, ..., e_{12}\right]^T, \tag{2.8}$$

the strain component ε_{xx}^{lin} can be written as follows:

$$\begin{aligned}\varepsilon_{xx}^{lin} = &\left(-\frac{6x}{l^2}+\frac{6x^2}{l^3}\right)e_1+\left(1-\frac{4x}{l}+\frac{3x^2}{l^2}\right)e_3-\frac{ye_5}{l}+ \\ &+\left(\frac{6x}{l^2}-\frac{6x^2}{l^3}\right)e_7+\left(-\frac{2x}{l}+\frac{3x^2}{l^2}\right)e_9+\frac{ye_{11}}{l}-1\end{aligned}, \tag{2.9}$$

where l is the length of the element. This strain component is the longitudinal strain of the element. Components that depend on the y coordinate are strains due to bending and components that depend only on x are axial strains. It can be seen that bending strain does not depend on the longitudinal coordinate, x, of the beam. This fact demonstrates that the element of Omar and Shabana exhibits linear bending behavior even though the third order interpolation polynomial is used. On the other hand, axial strain is unnecessarily described using quadratic polynomials. In summary, the use of the element of Omar and Shabana requires extra computation, which can be avoided using the proposed element with linear interpolation polynomials.

2.1.1 Kinematics of the Proposed Element

In this section, the kinematics of the proposed beam element is introduced. The proposed beam element uses linear polynomials instead of cubic polynomials to interpolate both the transverse and longitudinal components of displacement. The use of linear polynomials leads to eight unknown polynomial coefficients and for this reason the slope coordinates $\partial \mathbf{r}^T / \partial x$ can be neglected. It is important to reiterate that the reduced amount of nodal coordinates leads to a smaller number of degrees of freedom in each node of the finite element.

The assumed displacement field of the two-dimensional shear deformable element can be defined in a global coordinate system using the following linear polynomial expression:

$$\mathbf{r} = \begin{bmatrix} r_1 \\ r_2 \end{bmatrix} = \begin{bmatrix} a_0 + a_1 x + a_2 y + a_3 xy \\ b_0 + b_1 x + b_2 y + b_3 xy \end{bmatrix}. \tag{2.10}$$

Four nodal coordinates can be chosen for each node of a two-noded beam element as follows:

$$\mathbf{e}_I = \begin{bmatrix} \mathbf{r}_I^T & \dfrac{\partial \mathbf{r}_I^T}{\partial y} \end{bmatrix}^T . \tag{2.11}$$

The element shape function matrix **S** can be expressed by using the nodal coordinates and the interpolating polynomial of Equation (2.10) as follows:

$$\mathbf{S} = \begin{bmatrix} S_1\mathbf{I} & S_2\mathbf{I} & S_3\mathbf{I} & S_4\mathbf{I} \end{bmatrix}. \tag{2.12}$$

In Equation (2.12), **I** is a 2 × 2 identity matrix and the element shape functions $S_1 \ldots S_4$ can be written as

$$S_1 = 1 - \xi , \qquad S_2 = l(\eta - \xi\eta) , \qquad S_3 = \xi , \qquad S_4 = l\xi\eta ,$$

where l is the length of the element in the initial configuration and the non-dimensional quantities, ξ and η, are defined as

$$\xi = \frac{x}{l} , \qquad \eta = \frac{y}{l} .$$

The shape functions contain only one quadratic term, xy, while the remaining shape functions are products of one-dimensional linear polynomials. It is clear, that using this formulation the proposed linear beam element can not guarantee the continuity of longitudinal slopes at nodes. However, this is a general feature of C^0 elements which require only the continuity of the displacement but not the continuity of its derivatives. For this reason, the element is able to predict the accurate position of the structure only at the nodes, which has to be taken into account when the element is used.

2.2 The Elastic Forces of the Beam Element

The definition of the elastic forces for the absolute nodal coordinate beam element can be obtained by using a continuum mechanics approach [36, 40]. In this study, a nonlinear strain-displacement relationship is employed for the elastic forces. By utilizing the fact that vector **r** defines an arbitrary particle on the element in the global coordinate system, the deformation gradient can be defined as

$$\mathbf{D} = \frac{\partial(\mathbf{Se})}{\partial \mathbf{x}}\left[\frac{\partial(\mathbf{Se}_0)}{\partial \mathbf{x}}\right]^{-1} = \mathbf{J}\mathbf{J}_0^{-1}. \tag{2.13}$$

In Equation (2.13), the vectors of the nodal coordinates in the deformed and initial configuration are presented by **e** and $\mathbf{e}_0$. Matrix **J** is the position vector gradient and matrix $\mathbf{J}_0$ a constant transformation matrix. If the element has an arbitrary initial configuration, matrix $\mathbf{J}_0$ must be taken into account in the formulation of the elastic forces. Matrix $\mathbf{J}_0$ is the identity matrix in the case of a straight element with the initially coincident local and global coordinate systems.

The Green Lagrange strain tensor $\boldsymbol{\varepsilon}^m$ can be written using the right Cauchy-Green deformation tensor as follows:

$$\boldsymbol{\varepsilon}^m = \frac{1}{2}\left(\mathbf{D}^T\mathbf{D} - \mathbf{I}\right). \tag{2.14}$$

The strain tensor of $\boldsymbol{\varepsilon}^m$ is symmetric, and therefore, only three strain components are needed to identify it. These components can be written in vector form as

$$\boldsymbol{\varepsilon} = \left[\varepsilon_{xx}^m \quad \varepsilon_{yy}^m \quad 2\varepsilon_{xy}^m\right]^T. \tag{2.15}$$

Using matrix **E**, which contains the elastic coefficients of the material, the expression of the strain energy can be written as follows:

$$U = \frac{1}{2}\int_V \boldsymbol{\varepsilon}^T \mathbf{E} \boldsymbol{\varepsilon} \, dV. \tag{2.16}$$

Matrix **E** can be expressed for an isotropic homogenous material in terms of Lame's constants, λ and μ, as follows:

$$\mathbf{E} = \begin{bmatrix} \lambda + 2\mu & \lambda & 0 \\ \lambda & \lambda + 2\mu & 0 \\ 0 & 0 & \mu \end{bmatrix}. \qquad (2.17)$$

In Equation (2.17), $\lambda = E\nu / [(1+\nu)(1-2\nu)]$ and $\mu = E / [2(1+\nu)]$, where E is Young's modulus of elasticity and ν Poisson's ratio of the material.

The kinematical coupling of strain components ε_{xx}^{m}, ε_{yy}^{m}, and ε_{xy}^{m} may lead to Poisson's locking especially in the case of thin beams undergoing bending [41, 46]. Poisson's locking is caused by residual transverse normal stresses that contribute to the axial strain. This problem is known to exist for instance in the solid-shell elements, where a linear displacement assumption is used in thickness direction [47]. In the element of Omar and Shabana and in the proposed element, the displacement interpolations are linear in the transverse direction *y*. The transverse normal strain ε_{yy}^{m}, which is constant over the cross-section, is coupled via Poisson's ratio with the axial strain ε_{xx}^{m}, which varies linearly over the cross-section. This leads to linearly varying transverse normal stress over the cross-section that causes an overly stiff behavior in bending. This problem, which is known as Poisson's locking, is accentuated in the case of a thin beam where all strain components except the axial become zero.

By neglecting Poisson's effect, which is the source of Poisson's locking in the element of Omar and Shabana, the strain energy *U* can be written using Young's modulus of elasticity *E* and the shear modulus *G* as follows [48]:

$$U = \frac{1}{2} \int_{V} \left(E\varepsilon_{xx}^{m^2} + E\varepsilon_{yy}^{m^2} + 4k_s G\varepsilon_{xy}^{m^2} \right) dV . \qquad (2.18)$$

It is important to note that Poisson's ratio ν is still contributing to the value of the shear modulus G as follows:

$$G = \frac{E}{2(1+\nu)} . \tag{2.19}$$

In order to obtain the correct shear strain energy, the shear correction factor k_s is needed to minimize the error between the constant and the known true parabolic shear strain contributions.

The vector of the elastic forces, $\mathbf{Q}_e$, can be defined as the derivative of the strain energy expression with respect to the element nodal coordinate vector as follows:

$$\mathbf{Q}_e = -\left(\frac{\partial U}{\partial \mathbf{e}}\right)^T . \tag{2.20}$$

It is important to note that the linear interpolation leads to difficulties in terms of the continuity of shear forces for the beam formulations that use derivations of the displacement field over the longitudinal coordinate in the description of rotational deformation. When employing the derivation of the displacement field, the shear force q is described using the third derivative of vertical displacement as follows:

$$q = \int_A G \frac{\partial^3 w}{\partial x^3}\, dA , \tag{2.21}$$

where w is a vertical displacement. In the proposed element, the rotational coordinate is independent from the position description while the curvature is not used in the calculations of elastic forces. Consequently, the calculation of shear forces is employed using the following equation:

$$q = \int_A G \varepsilon_{xy}\, dA . \tag{2.22}$$

Only the first derivative of the position vector is needed to evaluate the shear strain while no higher degree derivatives are required to solve the shear force. Shear strain in the proposed element when using the linear strain-displacement relationship can be written as follows:

$$\begin{aligned} &I\text{ node: } \varepsilon_{xy|y=0,x=0} = -\frac{1}{2}\frac{e_2}{l} + \frac{1}{2}\frac{e_6}{l} + \frac{1}{2}e_3, \\ &J\text{ node: } \varepsilon_{xy|y=0,x=L} = -\frac{1}{2}\frac{e_2}{l} + \frac{1}{2}\frac{e_6}{l} + \frac{1}{2}e_7. \end{aligned} \tag{2.23}$$

On the other hand, the shear strain of the proposed element when using the nonlinear strain-displacement relationship can be written as follows:

$$\begin{aligned} &I\text{ node: } \varepsilon_{xy|y=0,x=0} = \frac{1}{2}\left(-\frac{e_1}{l} + \frac{e_5}{l}\right)e_3 + \frac{1}{2}\left(-\frac{e_2}{l} + \frac{e_6}{l}\right)e_4, \\ &J\text{ node: } \varepsilon_{xy|y=0,x=L} = \frac{1}{2}\left(-\frac{e_1}{l} + \frac{e_5}{l}\right)e_7 + \frac{1}{2}\left(-\frac{e_2}{l} + \frac{e_6}{l}\right)e_8. \end{aligned} \tag{2.24}$$

It is important to note that in the case of the Mindlin beam element [49], which also uses the linear shape functions, the shear strain is:

$$\begin{aligned} &I\text{ node: } \varepsilon_{xy|y=0,x=0} = \frac{-w_1 + w_2 - l\theta_2}{l}, \\ &J\text{ node: } \varepsilon_{xy|y=0,x=L} = \frac{-w_1 + w_2 - l\theta_1}{l}, \end{aligned} \tag{2.25}$$

where θ is a rotation of a node of the element. From Equation (2.25), the analogy to the proposed element with the linear strain-displacement relationship can be observed and the shear force of the Mindlin beam element is also evaluated using Equation (2.22). It can be seen from Equations

(2.23), (2.24) and (2.25), that the shear strain depends on the coordinates of both nodes of the elements. For this reason, the continuity of the shear force between the adjacent elements is not guaranteed in the cases of the proposed linear beam element and the Mindlin beam element if external forces are applied to the elements. This is a general feature of the C^0 –continuous beam elements which does not prevent the convergence.

The mass matrix given by the absolute nodal coordinate formulation is constant and symmetric. Using the element shape function given by Equation (2.12), the mass matrix **M** can be written as

$$\mathbf{M} = \int_V \rho\, \mathbf{S}^T \mathbf{S}\, dV , \tag{2.26}$$

where ρ and V are the material density and volume of the finite element, respectively.

2.2.1 Selective Integration of the Strain Energy

The shape functions of the proposed two-dimensional shear deformable beam element include only one quadratic term, *xy*. Therefore, the element is able to exhibit only a rectangular deformation shape. This characteristic results in parasitic shear strain under pure bending. Consequently, the element stores excess shear strain energy. Due to this feature, the bending moment needed for a given bending deformation is higher than the correct value [49]. It is important to point out that the element of Omar and Shabana is able to exhibit pure bending deformation without the parasite shear strain excluding the case of the linearly varying bending moment [41]. This is due to the fact that cubic interpolation polynomials are capable of describing the correct deformed shape under pure bending. In pure bending, shown in Figure 2.2 *a*, the strain components of the rectangular block are:

$$\varepsilon_{xx}^m = -\frac{\theta_1 y}{l_1}, \qquad \varepsilon_{yy}^m = \nu \frac{\theta_1 y}{l_1}, \qquad \varepsilon_{xy}^m = 0 .$$

In the case of the block in Figure 2.2 *b*, the element strains are:

$$\varepsilon_{xx}^{m} = -\frac{\theta_2 y}{l_2}, \qquad \varepsilon_{yy}^{m} = 0, \qquad \varepsilon_{xy}^{m} = -\frac{\theta_2 x}{l_2}.$$

As can be seen in Figure 2.2 *b*, the top and bottom sides of the block remain straight. Strain in the *x*-direction is still exact while strain in the *y*-direction is exact only if Poisson's ratio *v* is zero. However, it is important to note that the shear strain component is non-zero. For this reason, the proposed element generates the shear strain in bending. This feature combined with exact integration with equal and especially with linear interpolation for all directions of the elements leads to stiff behavior, which is known as shear locking [50, 51]. Due to shear locking, the bending of the element is penalized by high strain energy of the unwanted shear mode.

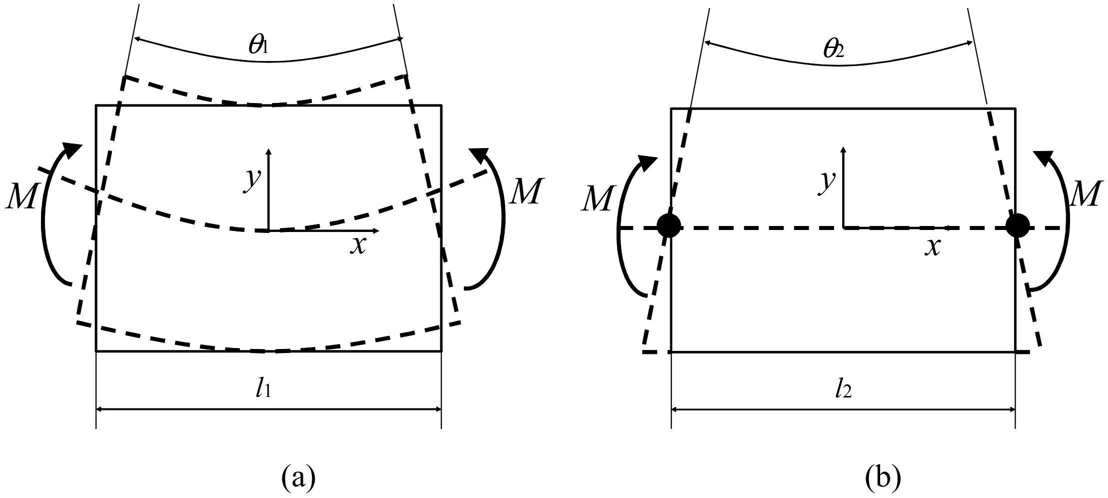

Figure 2.2 (a) The correct deformation mode of a rectangular block in pure bending.
(b) The shear locking of the element results in the incorrect deformation mode of a rectangular block in pure bending.

If the exact integration of all the integrals of the strain energy is used, the model is not able to receive analytical values of displacement, even if hundreds of elements are used. Especially in cases of thin beam structures, element shear locking results in overly small displacement in comparison with the exact values.

The shear locking can be avoided using many different approaches. Among these approaches are, for instance, mixed formulations and reduced integrations. To avoid the accompanying defects of spurious shear strain in the proposed element, selective integration is adopted within the numerical integration method for its simplicity and computational efficiency. It was perceived that the use of one Gauss point to evaluate the contribution of shear strain in the equation of strain energy, whereas two Gauss points are used to evaluate the contribution of normal strains, led to problems in convergence when the number of elements in the dynamic model was increased. Decreasing the height of the beam and setting the value of Poisson's ratio to 0.3 instead of zero improved the convergence of the beam element. When a small number of proposed elements was used, the model had a tendency to converge larger deformations in comparison to the other models.

These results can be explained as a consequence of using a low number of integration points in the selective integration of the strain components of the element. The use of a low number of integration points has a softening effect and may also introduce some spurious modes, such as zero-energy deformation or hourglass modes. The spurious modes incorporated by the stiffness matrix of the element can deactivate the resistance to nodal loads. As a result, spurious zero energy modes are activated in the element [49]. The convergence problem was solved by increasing the number of Gauss points from one to two when evaluating terms, which are functions of y, of the shear strain in the strain energy equation. The disadvantage of this method is that only rectangular cross-sections of the elements are easy to model.

In the final form, integration in closed form is used to evaluate the contribution of normal and shear strains over the cross-section of the element while the numerical integration method with one Gauss point is used to evaluate the contribution of strains in the axial direction. Due to this technique, the cross-section of the beam can be arbitrary. Integration in closed form does not work with the rational functions and this mathematical fact makes the use of the technique above with initially curved elements difficult.

2.3 Equations of Motion

Using the constant mass matrix and the elastic force vector, which includes a nonlinear strain-displacement relationship when continuum mechanics is used, the equations of motion of the deformable finite element can be written as [32]

$$\mathbf{M}\ddot{\mathbf{e}} = \mathbf{Q}_e + \mathbf{Q}_k \ , \tag{2.27}$$

where $\mathbf{Q}_k$ is the vector of the generalized external nodal forces. Since the mass matrix is constant, the vector of the accelerations $\ddot{\mathbf{e}}$ of Equation (2.27) can be efficiently solved using numerical procedures on the following equation:

$$\ddot{\mathbf{e}} = \mathbf{M}^{-1}(\mathbf{Q}_e + \mathbf{Q}_k) \, . \tag{2.28}$$

The kinematic constraints that depend on the nodal coordinates and possibly on time in the multibody system can be written in vector form as [52]

$$\mathbf{C}(\mathbf{e}, t) = \mathbf{0} \, , \tag{2.29}$$

where **C** is the vector of linearly independent constraint equations, **e** the nodal coordinate vector and *t* time. The equation of motion that accounts for the constraints can be defined using Lagrange's equation in matrix form by employing an augmented formulation as follows:

$$\mathbf{M}\ddot{\mathbf{e}} + \mathbf{C}_{\mathbf{e}}^T \boldsymbol{\lambda} = \mathbf{Q}_e + \mathbf{Q}_k \, . \tag{2.30}$$

In Equation (2.30), $\mathbf{C}_{\mathbf{e}}^T$ is the Jacobian matrix that is the partial derivative of the constraint vector with respect to the nodal coordinate vector, and $\boldsymbol{\lambda}$ is the vector of Lagrange multipliers. Note that a quadratic velocity vector is zero in the elements based on the absolute nodal coordinate formulation. The unknowns $\boldsymbol{\lambda}$ and $\ddot{\mathbf{e}}$ of Equation (2.30) can be determined by differentiating the constraints of Equation (2.29) twice with respect to time:

$$\mathbf{C_e}\ddot{\mathbf{e}} = -\mathbf{C}_{tt} - (\mathbf{C_e}\dot{\mathbf{e}})_{\mathbf{e}}\dot{\mathbf{e}} - 2\mathbf{C}_{\mathbf{e}t}\dot{\mathbf{e}} = \mathbf{Q}_d \quad , \tag{2.31}$$

and writing a system of differential and algebraic equations in matrix form as follows:

$$\begin{bmatrix} \mathbf{M} & \mathbf{C}_{\mathbf{e}}^T \\ \mathbf{C}_{\mathbf{e}} & \mathbf{0} \end{bmatrix} \begin{bmatrix} \ddot{\mathbf{e}} \\ \boldsymbol{\lambda} \end{bmatrix} = \begin{bmatrix} \mathbf{Q} \\ \mathbf{Q}_d \end{bmatrix}, \tag{2.32}$$

where $\mathbf{Q} = \mathbf{Q}_e + \mathbf{Q}_k$. It is important to note that Equation (2.32) can be easily extended to the systems of interconnected rigid and flexible bodies as follows [32]:

$$\begin{bmatrix} \mathbf{M}_r & \mathbf{0} & \mathbf{C}_{\mathbf{q}_r}^T \\ \mathbf{0} & \mathbf{M}_e & \mathbf{C}_{\mathbf{e}}^T \\ \mathbf{C}_{\mathbf{q}_r} & \mathbf{C}_{\mathbf{e}} & \mathbf{0} \end{bmatrix} \begin{bmatrix} \ddot{\mathbf{q}}_r \\ \ddot{\mathbf{e}} \\ \boldsymbol{\lambda} \end{bmatrix} = \begin{bmatrix} \mathbf{Q}_r \\ \mathbf{Q} \\ \mathbf{Q}_d \end{bmatrix}, \tag{2.33}$$

where **M** refers to a mass sub-matrix, subscripts *r* and *e* refer to rigid body and absolute nodal coordinates, respectively, and $\mathbf{Q}_r$ is the generalized forces associated with the rigid body coordinates. It is important to note that this kind of combination of different formulations may lead to a nonlinear description of inertia.

2.4 Numerical Results of the Linear Beam Element

In this section, the performance of the proposed shear deformable beam element is studied in static and dynamic problems. In the static problems, the simple beam structures of Figure 2.3 and Figure 2.4 are studied. The cross-section of the beam is rectangular and the length of the beam 2.0 m. The material of the structure is assumed to be isotropic, the Young's modulus of the material is $2.07 \cdot 10^{11}$ N/m^2 and the mass density 7850 kg/m^3. The results of the examples for the proposed beam element are compared to those of the analytical solutions and/or to the solutions obtained using a commercial finite element code ANSYS as well as a two-dimensional shear deformable beam element proposed by Omar and Shabana [36]. The strain energy of the proposed beam element is calculated using Equation (2.18) by employing a shear correction factor $k_s = 5/6$. Equation (2.16) is used to determine the strain energy in the case of the element proposed by Omar and Shabana.

For both element types, integration in closed form is used to evaluate the contribution of normal and shear strains over the cross-section of the element. The numerical integration method with one Gauss point is used for the proposed element to evaluate the contribution of strains in the axial direction, while four Gauss points are used for the element of Omar and Shabana. This is due to the fact that the element proposed by Omar and Shabana uses third order polynomial expansion.

In the first example, the linear deformations are considered using the simply supported beam structure shown in Figure 2.3. The boundary conditions are given to eliminate the horizontal and vertical displacements of the first node and the vertical displacement of the last node. The cross-section of the beam is a 0.1-m-sided square and a vertical load, $F = 1000$ N, is applied to the mid-point of the beam. The vertical displacements of the midpoint are studied using different numbers of elements for two values of the Poisson's ratio, 0.0 and 0.3. In the analytical solution, in the BEAM188 model in ANSYS [53], which uses linear interpolation and large rotation theory, and in the BEAM3 model in ANSYS, the effect of the shear deformation is considered. The results of the first example are shown in Table 2.1 and Table 2.2.

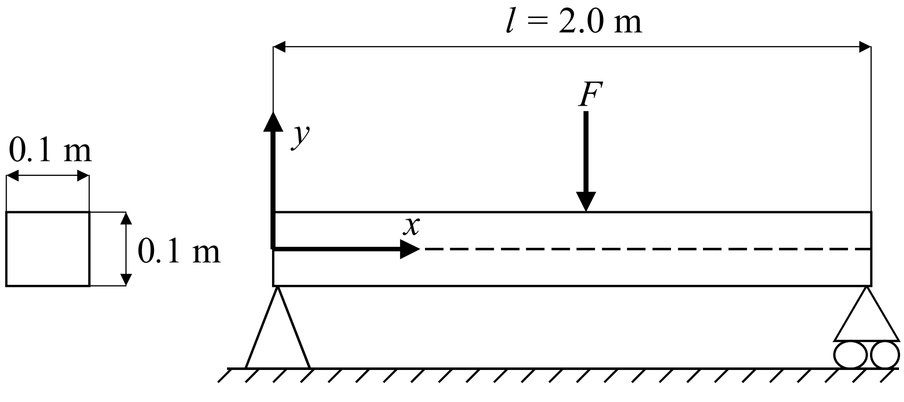

Figure 2.3 A simply supported beam for linear deformations.

Table 2.1 The vertical positions of the mid-point of the beam for a Poisson's ratio of 0.0.

Number of elements	Mid-point vertical position [mm]			**The difference between the analytical result and the result of the proposed element [%]**
	ANSYS: BEAM188	**The ANCF 2D beam element of Omar and Shabana**	**Proposed ANCF 2D beam element**	
2	-0.076623	-0.072893	-0.073043	24.453
4	-0.092050	-0.091034	-0.091159	6.213
8	-0.095060	-0.095578	-0.095688	1.554
16	-0.096871	-0.096717	-0.096821	0.388
32	-0.097112	-0.097005	-0.097104	0.097
64	-0.097172	-0.097078	-0.097174	0.025
The analytical result: -0.097198, ANSYS BEAM3: -0.097021				

Table 2.2 The vertical positions of the mid-point of the beam for a Poisson's ratio of 0.3.

Number of elements	Mid-point vertical position [mm]			**The difference between the analytical result and the result of the proposed element [%]**
	ANSYS: BEAM188	**The ANCF 2D beam element of Omar and Shabana**	**Proposed ANCF 2D beam element**	
2	-0.077871	-0.054388	-0.073217	24.740
4	-0.092491	-0.067879	-0.091333	6.118
8	-0.096146	-0.071262	-0.095862	1.463
16	-0.097060	-0.072112	-0.096995	0.298
32	-0.097288	-0.072327	-0.097278	0.007
64	-0.097345	-0.072382	-0.097348	0.065
The analytical result: -0.097285, ANSYS BEAM3: -0.097142				

It can be seen in Table 2.1 that in the case of zero Poisson's ratio, the behavior of all the linear elements is very similar. The beam element of Omar and Shabana predicts the most underestimated displacement in comparison with the analytical result. In every element model, the bending moment is constant, and for this reason, these elements give more accurate results when the number of elements is increased. The difference indicator between the results of the proposed element and the analytical result proves the convergence of the proposed element by illustrating that the difference decreases when the number of elements is increased.

Table 2.2 shows that when the Poisson's ratio of the material is non-zero, the model by Omar and Shabana suffers from residual transverse normal stresses [41], which leads to notably smaller deformations in comparison with the results of the other models. The proposed beam element as well as the BEAM188 element converges to slightly larger deformations than the analytical solution, which demonstrates slightly excessive flexible behavior.

In addition, the results of Table 2.1 and Table 2.2 demonstrate that if less than 32 elements are used, the BEAM3 model, the results of which are independent from the number of elements, predicts deformations more accurately in comparison with the other models. However, it is important to point out that the BEAM3 model is based on the linear theory of small deformations and infinitesimal rotations and it is not applicable to the prediction of large deformations of nonlinear analysis due to convergence problems. The proposed element is developed especially for large rotations and deformations and the example of small deformations is presented only to verify the convergence of the element.

In the second example, large nonlinear deformations of the simple cantilever structure shown in Figure 3 are considered and compared to the nonlinear solution of the BEAM188 model in ANSYS [41, 53]. The other end of the beam is clamped by boundary conditions that eliminate the horizontal and vertical displacement and slopes $\partial r_1 / \partial y$ and $\partial r_2 / \partial y$ of the first node. The vertical displacements of the endpoint are examined using different numbers of elements for the two different cantilever models: In the first model (Model 1), the beam has a 0.1-m-sided square cross-section and the value of the Poisson's ratio is 0.3, whereas in the second model (Model 2), the height h of the beam is increased from 0.1 m to 0.5 m while the Poisson's ratio is 0.0. A vertical force, $F = -5.0 \cdot 10^8 \cdot h^3$ N, is applied to the free end of the cantilever. The results of the second problem are shown in Table 2.3 and Table 2.4.

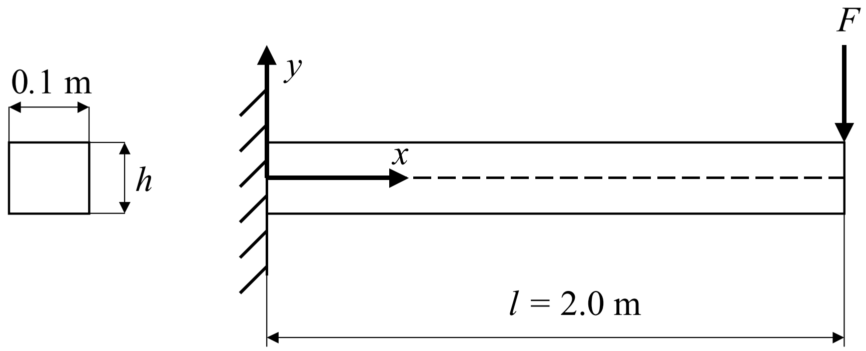

Figure 2.4 The cantilever beam model for nonlinear deformations.

Table 2.3 The positions of the beam endpoint in Model 1.

Number of elements	Tip Position (x, y), [m]		
	The ANCF 2D beam element of Omar and Shabana	**Proposed ANCF 2D beam element**	**ANSYS: BEAM188**
2	1.95536, -0.37731	1.88480 -0.62126	1.87080, -0.65671
4	1.91970, -0.50932	1.86351 -0.66320	1.85918, -0.67485
8	1.91344, -0.53035	1.85696 -0.67691	1.85618, -0.67947
16	1.91276, -0.53267	1.85537 -0.68018	1.85540, -0.68069
32	1.91264, -0.53309	1.85500 -0.68091	1.85520, -0.68100
64	1.91262, -0.53319	1.85491 -0.68109	1.85515, -0.68108

As can be seen in Table 2.3, in the case of Model 1 the beam element of Omar and Shabana seems to suffer from residual transverse normal stresses leading to overly small displacements. The predicted displacements of the proposed model and the BEAM188 model are very similar with the exception of the case of two elements.

Table 2.4 The positions of the beam endpoint in Model 2.

Number of elements	Tip Position (*X*, *Y*), [m]		
	The ANCF 2D beam element of Omar and Shabana	**Proposed ANCF 2D beam element**	**ANSYS: BEAM188**
2	1.86909, -0.64098	1.87307 -0.65134	1.86749, -0.67783
4	1.84841, -0.69436	1.85001 -0.69591	1.85551, -0.69700
8	1.84498, -0.70341	1.84412 -0.70709	1.85246, -0.70179
16	1.84407, -0.70573	1.84271 -0.70970	1.85169, -0.70299
32	1.84378, -0.70643	1.84237 -0.71034	1.85150, -0.70329
64	1.84367, -0.70667	1.84228 -0.71050	1.85145, -0.70337

According Table 2.4, the results of the proposed element and the element of Omar and Shabana are in good agreement, but the BEAM188 model slightly underestimates displacements in comparison to the other models. It is important to note that, in this problem, computer times in iterations with the proposed element were two times shorter than with the element of Omar and Shabana.

Generally, the results in the cases of linear and non-linear deformations are in good agreement. It is clear that neither the proposed elements nor the element of Omar and Shabana achieve good results with one element. A good accuracy with one element in the case of linear deformations can be achieved in simple cases, as shown by Dufva *et al*. [54]. Generally speaking, this is not the initial objective of the finite element method due to its approximate nature. The use of elements as simple as possible is popular due to their straightforward implementation and computational efficiency. The fact is that there are two approaches, the *h*-method and the *p*-method, to improve the accuracy in problems within finite element programs. The idea of the *h*-method is to increase the number of elements. In the *p*-method, the accuracy of the results is increased by increasing the complexity, usually the order of the interpolation polynomials, of the element. The utility of the proposed element is related to computational efficiency within the *h*-method. For non-linear deformations, the discrepancies between the different models increased when the height of the beam was increased, which enhanced the significance of the role of shear strain.

In the first dynamic problem, the dynamic behavior of a simple planar pendulum, which consists of one beam, shown in Figure 2.5, is studied using different numbers of proposed two-node two-dimensional shear deformable beam elements. The pendulum is connected to the ground by a revolute joint, and the only force acting on the system is gravity, which is equal to 9.81 m/s^2. The cross-section of the beam is a 0.1-m-sided square, while the length of the beam is 2.0 m. The material of the structure is assumed to be isotropic and the Young's modulus of the material is $2.07 \cdot 10^7$ N/m^2, the Poisson's ratio 0.0 and the mass density 7850 kg/m^3.

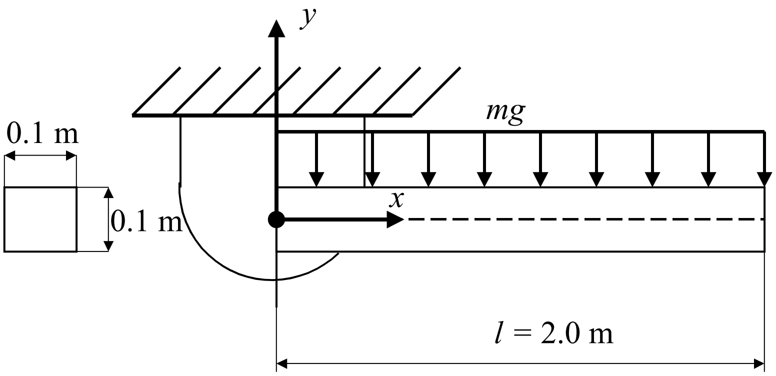

Figure 2.5 A free falling flexible pendulum for dynamic verification in the initial position.

The initial position of the beam is horizontal with zero initial velocity. The vertical displacement of the beam endpoint for different numbers of elements is shown in Figure 2.6. As can be seen from the figure, the solutions for 8 and 16 elements are almost identical while the solution for 4 elements is in good agreement with them.

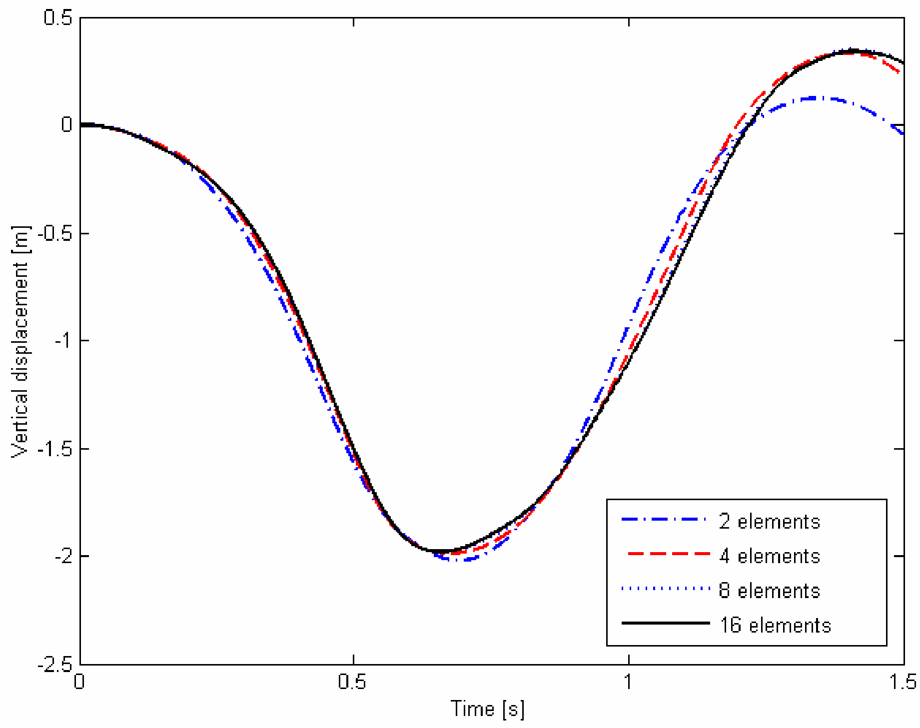

Figure 2.6 Vertical displacement of the falling flexible beam tip point using 2, 4, 8 and 16 elements.

The energy balance of the beam should remain constant due to the fact that the free-falling pendulum is a conservative system. This can be written as follows:

$$\sum_{i}^{n}\left(T^{i}+V^{i}+U^{i}\right)=\text{constant}\,, \tag{2.34}$$

where n is the number of elements of the system, T^{i} the kinetic energy, V^{i} the potential energy and U^{i} the strain energy of the element i [40]. The energy components of the pendulum made up of 4 elements are shown in Figure 2.7. It can be seen that the energy balance remains constant with excellent accuracy. In this case, the greatest deviation of the sum from the constant is $0.62\cdot 10^{-4}$ J.

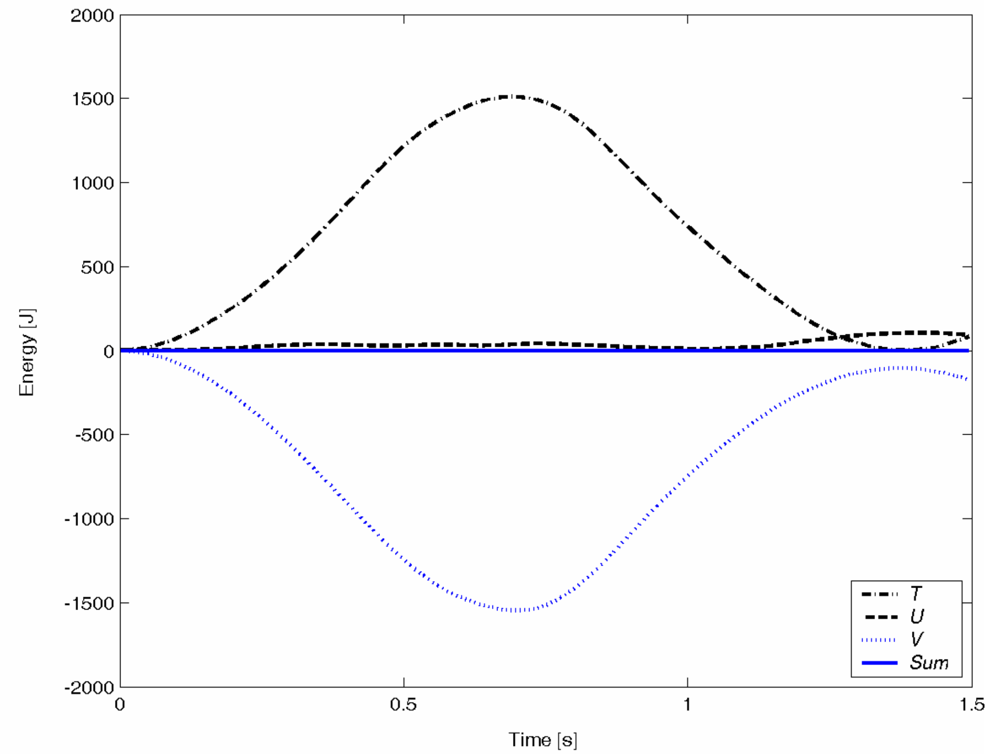

Figure 2.7 The energy components and energy balance of the falling flexible beam modeled using 4 elements.

A comparison of the vertical displacement between the proposed element and that presented by Omar and Shabana is shown in Figure 2.8. The results are obtained using 8 elements and good agreement can be observed between the models. Using the proposed beam element, a significant saving in computation time can be achieved in comparison to using the beam element presented by Omar and Shabana. This is due to the fact that fewer nodal coordinates and simpler polynomials are needed to identify the element, and the dimensions of the vectors and matrices in the calculation are smaller. A comparison of the performance of the elements in terms of relative computer time is shown in Table 2.5.

Table 2.5 The performance of the elements in terms of relative computer time.

Number of elements	**CPU time for the element of Omar and Shabana**	**CPU time for the proposed element**
4	100 %	65 %
8	100 %	68 %

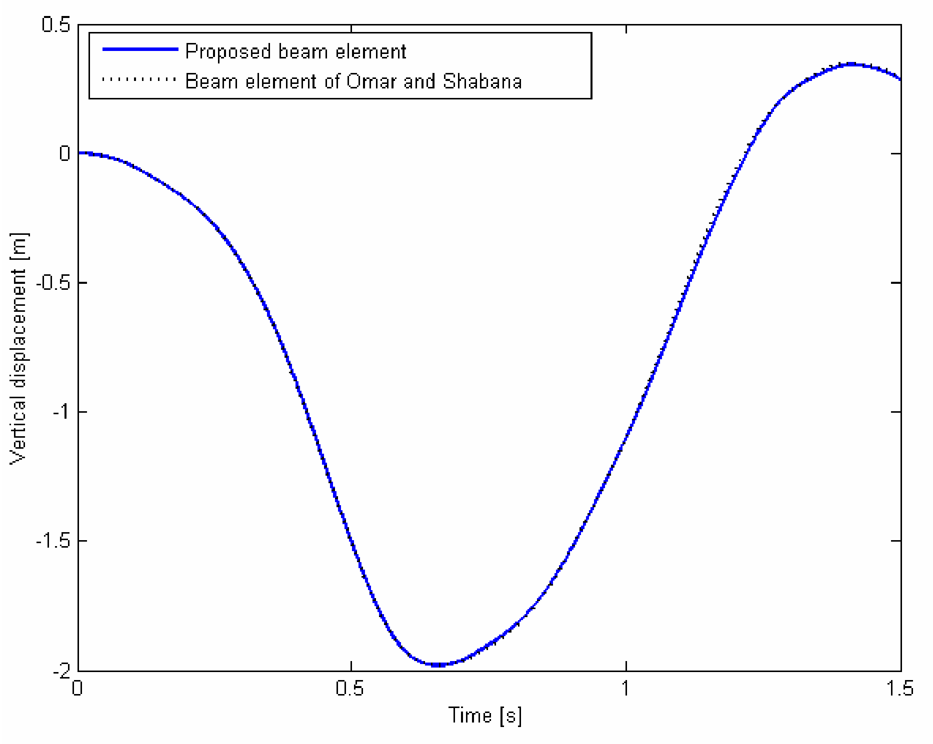

Figure 2.8 A comparison of the vertical displacement between the proposed element and that presented by Omar and Shabana using 8 elements.

In the second dynamic problem, the centrifugal stiffening effect in the spinning cantilever beam modeled with the proposed elements is under examination. A proper definition of beam deformation for the spinning beam demands coupling of the axial force with a bending moment. The capability of capturing this so-called geometrical or centrifugal stiffening effect is examined by modeling a rapidly spinning flexible beam in Figure 2.9 using the parameters and angular displacements reported by Wu and Haug [55]. The beam has a length of 8 m, a width of $1.986 \cdot 10^{-3}$ m, a height of $3.675 \cdot 10^{-2}$ m, a modulus of elasticity of $6.895 \cdot 10^{10}$ N/m^2 and a density of 2766.67 kg/m^3. The angular displacement is given as follows:

$$\theta = \begin{cases} \dfrac{\omega_{\mathrm{s}}}{T_{\mathrm{s}}}\left[\dfrac{1}{2}t^2 + \left(\dfrac{T_{\mathrm{s}}}{2\pi}\right)^2\left(\cos\left(\dfrac{2\pi t}{T_{\mathrm{s}}}\right) - 1\right)\right], & t < T_{\mathrm{s}} \\ \omega_s\left(t - \dfrac{T_{\mathrm{s}}}{2}\right), & t \geq T_{\mathrm{s}} \end{cases} . \tag{2.35}$$

According to Equation (2.35), the steady state angular velocity is reached after T_s seconds. The beam is modeled using three elements and the parameters above. It is important to note that when a nonlinear strain-displacement relationship is used instead of a linear relationship for the elastic forces of the element, there does not exist any critical angular velocity that could induce unstable behavior. This has been demonstrated by Berzeri *et al*. [56]. The difference between the global vertical positions of the endpoints of the modeled beam and the straight shadow beam obtained using an angular velocity ω_s of 4 rad/s and an acceleration time T_s of 15 s during the simulation of 20 s is illustrated in Figure 2.10.

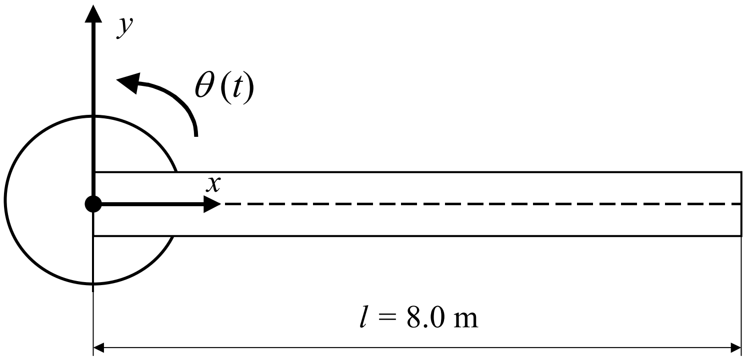

Figure 2.9 A rotating flexible cantilever beam.

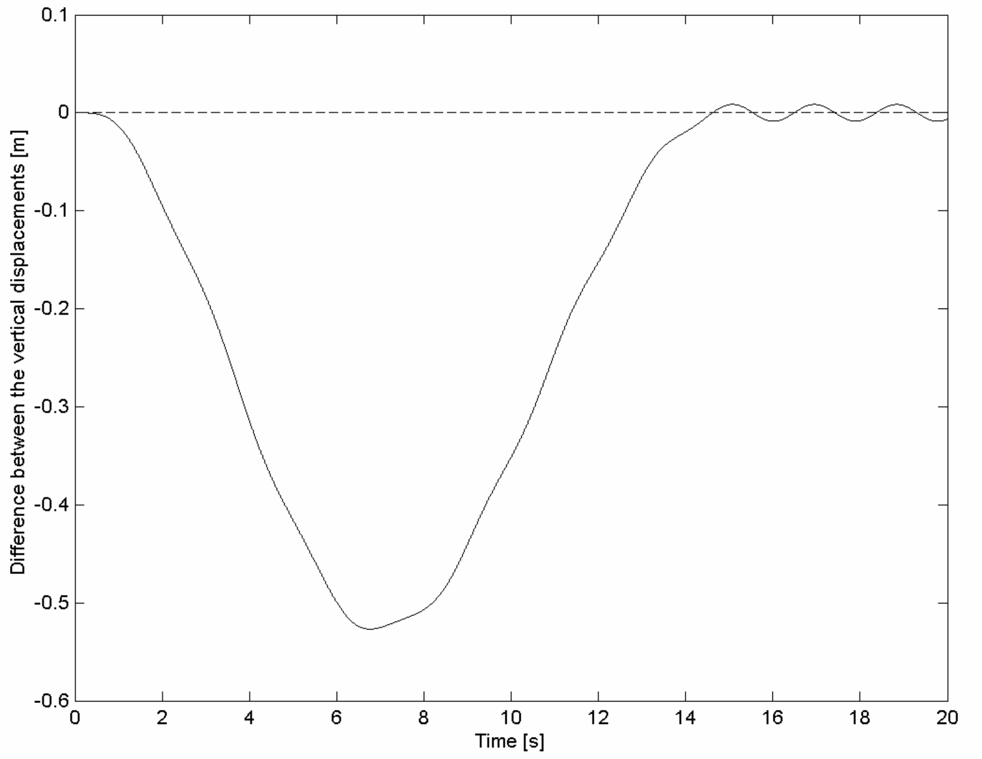

Figure 2.10 The difference of the endpoint vertical displacements between the modeled beam and the straight shadow beam.

A useful indicator of the capability of capturing the geometrical stiffening effect is the steady state axial extension of the beam. The exact solution for the axial extension u_{x} of the beam can be written in the following form [57]:

$$u_{\mathrm{x}} = l\left(\frac{\tan(al)}{al} - 1\right), \tag{2.36}$$

where

$$a = \sqrt{\frac{\rho A}{EA}}\omega_{\mathrm{s}}. \tag{2.37}$$

In Equation (2.37) ω_{s} is the steady state angular velocity. The analytical value of the axial extension of the beam at the steady state phase in this case is $1.09545 \cdot 10^{-4}$ m. The difference between the global horizontal positions of the endpoints of the modeled beam and the straight shadow beam and the value of the axial extension of the beam at the steady state phase are depicted in Figure 2.11.

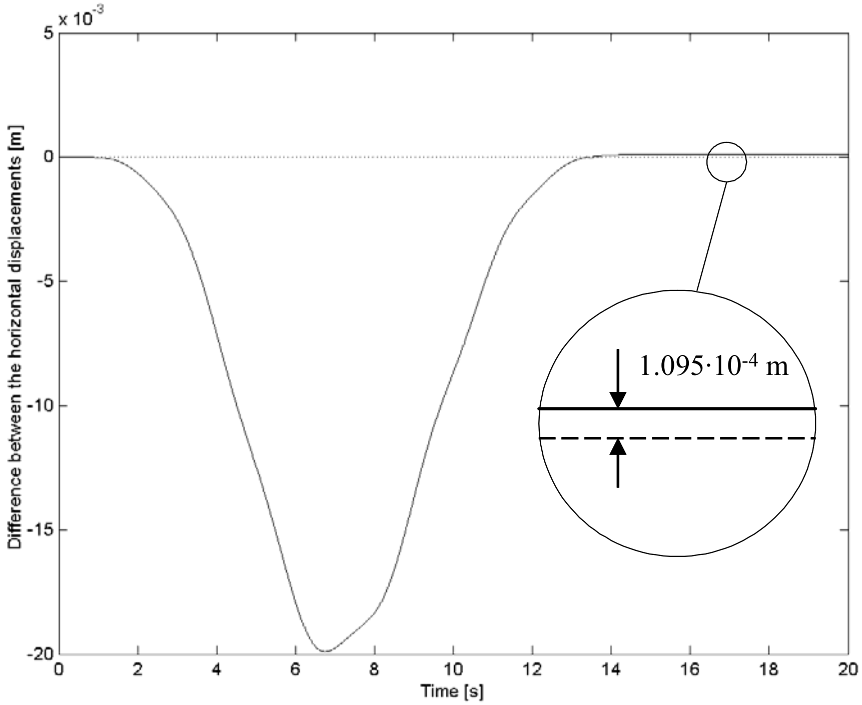

Figure 2.11 The difference of the endpoint horizontal displacements between the modeled beam and the straight shadow beam and the axial extension of the rotating beam.

The results shown in Figure 2.11 are in good agreement with the results of References [55, 57]. There exist small vibrations during the steady state phase, which was expected in the results of Reference [58], where the centrifugal stiffening effect using the absolute nodal coordinate formulation is studied. As can be seen from Figure 2.11, the axial extension of the beam corresponds with the analytical value with good accuracy. On the basis of these results, a capability of automatic accounting of the centrifugal stiffening effect of a spinning beam can be reached by using the proposed elements.

3 MODELING OF TWO-DIMENSIONAL BELT-DRIVES

The elements [36], [37] and [39], which use the continuum mechanics in the description of the elastic forces, suffer from several problems leading to inaccuracies in computation. These problems can be listed as follows [41], [43]: 1. Poisson's locking due to the residual transverse normal stresses. 2. Curvature thickness locking due to the element shrinking in bending. 3. Shear locking due to the inability of the element to describe constant shear strain if the bending moment is linearly varied. 4. Inaccurate description of bending. As shown in the previous chapter, the proposed linear element avoids the problems 1…3 and is one possibility to improve the performance of the elements based on continuum mechanics. It is usable in most of the applications but has still a problem with accuracy in the description of bending because of linearity. This problem reduces the effectiveness of the element in the cases where the description of the behavior related to bending is a dominant feature. In addition, when the linear elements are used to model belt-drives, the contact forces should be solved only at the nodes without the use of the distributed contact forces. Therefore, in order to achieve the required accuracy, the number of elements should be high in comparison with the use of higher order elements. In fact, the use of the proposed linear element in the modeling of belt-drives represents the same category of research as the belt-drive studies proposed by Leamy and Wasfy. In the computationally reasonable modeling of belt-drives the elements used must be able to be curved along the circular shape of pulleys. In order to achieve this feature with a small number of elements, recently introduced higher order elements are chosen to be utilized for modeling of belt-drives.

3.1 Formulation of the Shear Deformable Two-Dimensional Belt Element

In the belt-drive applications the belts exhibit a non-isotropic behavior that cannot be captured using a conventional beam element. For this reason, it is desirable to formulate an element that allows for reducing the bending stiffness of the element. The beam finite element used in this study is based on a two-dimensional element originally proposed by Dufva *et al*. [54]. This shear deformable element is based on the absolute nodal coordinate formulation and it includes an accurate expression of the elastic forces. In the element, a continuum mechanics approach is utilized in the exact displacement field of the shear deformable beam. This leads to the capability of accurately predicting the nonlinear deformations without suffering from shear or Poisson's locking.

The behavior of the belts strongly depends on the kinds of loads they are subjected to. In most of the cases, the stiffness of the belt in bending is usually much lower than in axial deformations due to the use of the composite material. For this reason, the beam element proposed by Dufva *et al.* [54] is slightly modified to obtain an element with reduced bending stiffness. In the following, kinematics and strain measures used to obtain the elastic forces of the element are introduced. The position $\mathbf{r}_P$ of an arbitrary particle P in the element can be defined as follows:

$$\mathbf{r}_P = \mathbf{r}_c + \mathbf{A}_\gamma \mathbf{A}_\psi \mathbf{v}. \tag{3.1}$$

In Equation (3.1), $\mathbf{r}_c$ is the global position of the centerline of the element and the transformation matrices $\mathbf{A}_\psi$ and $\mathbf{A}_\gamma$ are due to the rotation of the centerline and shear deformation, respectively. In Equation (3.1), vector $\mathbf{v}$ contained in the cross-section can be written as

$$\mathbf{v} = \begin{bmatrix} 0 & y \end{bmatrix}^T, \tag{3.2}$$

where y is the location of the particle P on the cross-section of the beam. In the absolute nodal coordinate formulation, slopes and displacements are used as the nodal coordinates instead of finite or infinitesimal rotations. Due to this fact, the components in rotation matrixes $\mathbf{A}_\psi$ and $\mathbf{A}_\gamma$ can be described straightforwardly with the help of the shape function matrix and the nodal coordinates. The rotation matrix $\mathbf{A}_\psi$ can be expressed as follows:

$$\mathbf{A}_\psi = \begin{bmatrix} \mathbf{t}_\psi & \mathbf{n}_\psi \end{bmatrix}. \tag{3.3}$$

In Equation (3.3) the vectors $\mathbf{t}_\psi$ and $\mathbf{n}_\psi$, shown in Figure 3.1, depend only on the longitudinal coordinate x and can be expressed using the global position of the centerline as follows:

$$\mathbf{t}_\psi = \frac{\dfrac{\partial \mathbf{r}_c}{\partial x}}{\left\| \dfrac{\partial \mathbf{r}_c}{\partial x} \right\|}, \tag{3.4}$$

$$\mathbf{n}_\psi = \tilde{\mathbf{I}}\mathbf{t}_\psi, \tag{3.5}$$

where

$$\tilde{\mathbf{I}} = \begin{bmatrix} 0 & -1 \\ 1 & 0 \end{bmatrix}. \tag{3.6}$$

In Equation (3.4) $\|.\|$ denotes the L_2 norm. Since the angle that characterizes the shear deformation is small, matrix $\mathbf{A}_\gamma$ can be calculated by assuming the rotation to be infinitesimal. In this case, the rotation matrix $\mathbf{A}_\gamma$ can be written as

$$\mathbf{A}_\gamma \approx \left(\mathbf{I} + \tilde{\mathbf{I}}\sin\gamma\right), \tag{3.7}$$

where γ is a shear angle as shown in Figure 3.1

The position $\mathbf{r}_P$ of an arbitrary particle P of the element in Figure 3.1 can also be defined as follows:

$$\mathbf{r}_P = \mathbf{r}_c + y\mathbf{r}_s, \tag{3.8}$$

where the position of an arbitrary particle P has been decomposed as the sum of the position of the point where the centerline intersects the cross-section and a vector contained in the cross-section. Vectors $\mathbf{r}_c$ and $\mathbf{r}_s$ are not functions of the transverse coordinate y and can be written as follows:

$$\mathbf{r}_c = \left.\mathbf{Se}\right|_{y=0}, \tag{3.9}$$

$$\mathbf{r}_s = \left(\mathbf{I} + \tilde{\mathbf{I}}\sin\gamma\right)\tilde{\mathbf{I}}\mathbf{t}_\psi. \tag{3.10}$$

In Equation (3.9), $\mathbf{S}$ is the element shape function matrix, which in the case of a shear deformable planar beam element contains cubic terms in x and linear terms in y as follows [54]:

$$\mathbf{S} = \left[S_1\mathbf{I} \quad S_2\mathbf{I} \quad S_3\mathbf{I} \quad S_4\mathbf{I} \quad S_5\mathbf{I} \quad S_6\mathbf{I}\right], \tag{3.11}$$

where

$$S_1 = 1 - 3\xi^2 + 2\xi^3, \qquad S_2 = l(\xi - 2\xi^2 + \xi^3), \qquad S_3 = l\left(\eta - \xi\eta\right),$$

$$S_4 = 3\xi^2 - 2\xi^3, \qquad S_5 = l(-2\xi^2 + \xi^3), \qquad S_6 = l\xi\eta,$$

where the non-dimensional quantities are defined as

$$\xi = \frac{x}{l}, \qquad \eta = \frac{y}{l}.$$

In Equation (3.10), $\mathbf{I}$ is an identity matrix, γ is a shear angle as shown in Figure 3.1 and $\mathbf{t}_\psi$ is a vector that defines the tangent of the beam's centerline.

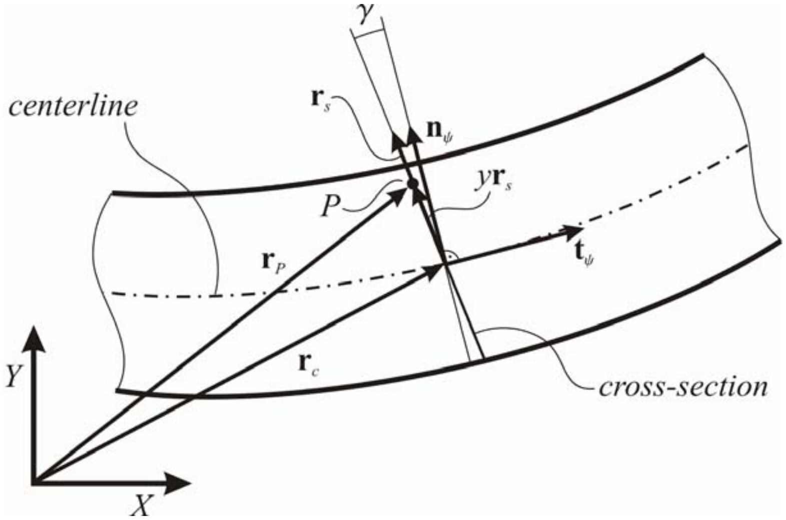

Figure 3.1 Description of the position of an arbitrary particle, *P*.

In Equation (3.10), vector $\mathbf{r}_s$ is obtained by two successive rotations over vector $\mathbf{t}_\psi$. First, vector $\mathbf{t}_\psi$ is rotated 90 degrees using matrix $\tilde{\mathbf{I}}$ leading to a vector $\mathbf{n}_\psi$ shown in Figure 3.1 and after that, an angle of γ due to shear deformation.

The linear distribution of the shear angle can be obtained using a method that resembles the mixed interpolation technique as follows:

$$\sin\gamma \approx (\sin\gamma)^I (1-\frac{x}{l}) + (\sin\gamma)^J \frac{x}{l}. \tag{3.12}$$

In Equation (3.12), $(\sin\gamma)^I$ and $(\sin\gamma)^J$ are related to the nodal points *I* and *J* of the element, respectively, and x is the longitudinal coordinate of the element [54]. Initially the beam is assumed to be coincident with the global coordinate system and not curved. The strain components ε_{xx}^m and ε_{xy}^m can be calculated using Green-Lagrange measures as follows:

$$\varepsilon_{xx}^m = \frac{1}{2}\left[\frac{\partial \mathbf{r}^T}{\partial x}\frac{\partial \mathbf{r}}{\partial x} - 1\right], \tag{3.13}$$

$$\varepsilon_{xy}^{m} = \frac{1}{2}\left[\frac{\partial \mathbf{r}^{T}}{\partial x}\frac{\partial \mathbf{r}}{\partial y}\right]. \tag{3.14}$$

The strain component ε_{yy}^{m} in the transverse direction of the beam can be defined employing the slope vector $\partial\mathbf{r}/\partial y$ at the nodal points together with linear interpolation functions, as explained in Reference [54]. After algebraic manipulations and excluding the superscripts that refer to the number of elements, the terms involved in Equation (2.18) can be rewritten as follows:

$$\begin{aligned}
\varepsilon_{xx}^{m\,2} = {} & \frac{1}{4}\left(\mathbf{r}_{c,x}^{T}\mathbf{r}_{c,x}-1\right)^{2}+\left(\mathbf{r}_{c,x}^{T}\mathbf{r}_{c,x}-1\right)\left(\mathbf{r}_{c,x}^{T}\mathbf{r}_{s,x}\right)y+ \\
& +\left[\left(\mathbf{r}_{c,x}^{T}\mathbf{r}_{s,x}\right)^{2}+\frac{1}{2}\left(\mathbf{r}_{c,x}^{T}\mathbf{r}_{c,x}-1\right)\left(\mathbf{r}_{s,x}^{T}\mathbf{r}_{s,x}\right)\right]y^{2}+, \\
& +\left(\mathbf{r}_{c,x}^{T}\mathbf{r}_{s,x}\right)\left(\mathbf{r}_{s,x}^{T}\mathbf{r}_{s,x}\right)y^{3}+\frac{1}{4}\left(\mathbf{r}_{s,x}^{T}\mathbf{r}_{s,x}\right)^{2}y^{4}
\end{aligned} \tag{3.15}$$

$$\varepsilon_{xy}^{m\,2} = \frac{1}{4}\left(\mathbf{r}_{c,x}^{T}\mathbf{r}_{s}\right)^{2}+\frac{1}{2}\left(\mathbf{r}_{c,x}^{T}\mathbf{r}_{s}\right)\left(\mathbf{r}_{s,x}^{T}\mathbf{r}_{s}\right)y+\frac{1}{4}\left(\mathbf{r}_{s,x}^{T}\mathbf{r}_{s}\right)^{2}y^{2}. \tag{3.16}$$

In Equations (3.15) and (3.16) the term $\mathbf{r}_{i,x}$, where $i = c$, s is the partial derivative of vector $\mathbf{r}_{i}$ with respect to x. Loads that cause bending as well as those that cause elongation of the element induce strains in the longitudinal direction. For this reason, the strain energies due to axial and bending solicitations are both contained in the first term of Equation (2.18). It is important to note that the strain due to axial loads is supposed to be constant along the thickness of the element and, consequently, the strain energy per unit of volume due to elongation of the element must be independent of the coordinate y. Moreover, the elongation ε_{l} of the centerline of the element can be written as follows [40]:

$$\varepsilon_l = \frac{1}{2}\left(\mathbf{r}_{c,x}^T \mathbf{r}_{c,x} - 1\right). \tag{3.17}$$

According to Equation (3.17), the part of ${\varepsilon_{xx}^m}^2$ corresponding to the strain energy associated with an elongation of the element can be easily identified in Equation (3.15). Therefore, in order to modify the bending stiffness of the element, coefficients α_1 and α_2 are included determining the importance of each term in the equation of the strain energy. Due to the symmetry of the cross-section of the element, terms that are multiplied by y and y^3 in Equations (3.15) and (3.16) vanish after integration over the y coordinate. Thus, using Equations (3.15) and (3.16), the first and last terms on the right hand side of Equation (2.18) can be written as follows:

$$\begin{aligned}\frac{1}{2}\int_V E{\varepsilon_{xx}^m}^2 dV = \frac{E}{2}\int_V \Bigg[& \frac{\alpha_1}{4}\left(\mathbf{r}_{c,x}^T \mathbf{r}_{c,x} - 1\right)^2 + \alpha_2 \Bigg[\left(\mathbf{r}_{c,x}^T \mathbf{r}_{s,x}\right)^2 + \\ & + \frac{1}{2}\left(\mathbf{r}_{c,x}^T \mathbf{r}_{c,x} - 1\right)\left(\mathbf{r}_{s,x}^T \mathbf{r}_{s,x}\right)\Bigg] y^2 + \frac{\alpha_2}{4}\left(\mathbf{r}_{s,x}^T \mathbf{r}_{s,x}\right)^2 y^4 \Bigg] dV\end{aligned}, \tag{3.18}$$

$$\frac{1}{2}\int_V 4k_s G{\varepsilon_{xy}^m}^2 dV = 2k_s G\int_V \left[\frac{\alpha_2}{4}\left(\mathbf{r}_{c,x}^T \mathbf{r}_s\right)^2 + \frac{\alpha_2}{4}\left(\mathbf{r}_{s,x}^T \mathbf{r}_s\right)^2 y^2\right] \; dV\,. \tag{3.19}$$

Note that since there should be no tangential deformation ε_{xy}^m in a pure axial strength state, the part of the energy due to transverse strain is affected by coefficient α_2. As can be seen from Equations (3.18) and (3.19), parameters α_1 and α_2 can be used to modify the Young modulus used to calculate the elastic forces due to axial elongation and the Young modulus used in bending deformation. In the case of small strains, parameters α_1 and α_2 linearly affect the axial and bending stiffness of the element.

3.2 Modeling of the Frictional Contact

In power transmission systems that use belts and pulleys, the belt is constrained to move over the surface of the pulley. The contact between both solids must include frictional forces, which are, in fact, responsible for the transmission of motion from the pulley to the belt and *vice versa.* In this study, frictional contact between the pulleys and the belt is modeled applying a method that is based on the studies of Leamy and Wasfy [1, 25]. In this method, a penalty formulation is applied with a Coulomb-like tri-linear creep-rate dependent friction. The advantages of the law are numerical stability and physical relevance in the case of small sliding velocity [23].

In the models proposed by Leamy and Wasfy [1, 25], the forces are applied to the nodes of the low order elements. A normal reaction force and a tangential friction force are generated when a node on the finite element is in contact with the surface of the constraint. The contact forces depend significantly on the closest distance between the node and the contact surface. The contact exists when the node is inside the contact body. The results of their models, where low order elements are used, are based on the discretizations from 38 (154 degrees of freedom) up to 100 (202 degrees of freedom) elements per half pulley. It is important to reiterate that one of the main objectives in this study is to use the absolute nodal coordinate formulation in order to decrease the number of the needed elements and degrees of freedom.

In contrast to the study of Leamy and Wasfy, the two-dimensional high order elements used in this study are capable of reproducing curved shapes using a small number of elements. It is shown in Reference [54] that the use of only four elements enables the bending of a cantilever beam into a circle when a certain concentrated moment is applied at the free end. Since the element can be curved over the surface of the pulley, in contrast to the linear low order element used in the models proposed by Leamy and Wasfy [1, 25], the contact forces do not need to be applied at the nodes only. The use of a high order element enables the distribution of the contact forces along the length of the element. Although the main idea of the model of the contact forces remains the same as in the models of Leamy and Wasfy, the procedure used in this study is subtly different, as it is shown in detail in this section.

In the contact description, the element is allowed to penetrate the pulley at a certain distance d as depicted in Figure 3.2, and, as a result of this penetration, a force which is perpendicular to the surface of the pulley and directed along vector **n,** appears. This force is proportional to the penetration d and to its time-derivative $\dot{d}$. Due to the capability of the high order element of adopting a curved configuration, the penetration is a function of the longitudinal coordinate of the element, x, and as a consequence, the normal and tangential contact forces also depend on x. Thus the distributed normal reaction force $\mathbf{f}_n$ between the pulley and the belt can be written as follows:

$$\mathbf{f}_n = \begin{cases} (k_p d + c_p \dot{d})\mathbf{n}, & d \geq 0 \\ \mathbf{0}, & d < 0 \end{cases}. \tag{3.20}$$

In Equation (3.20), **n** is the unit normal vector at the contact surface, d denotes the closest distance between an arbitrary particle in the element and the contact surface and k_p and c_p are the stiffness and damping coefficient per unit length of the penalty force, respectively.

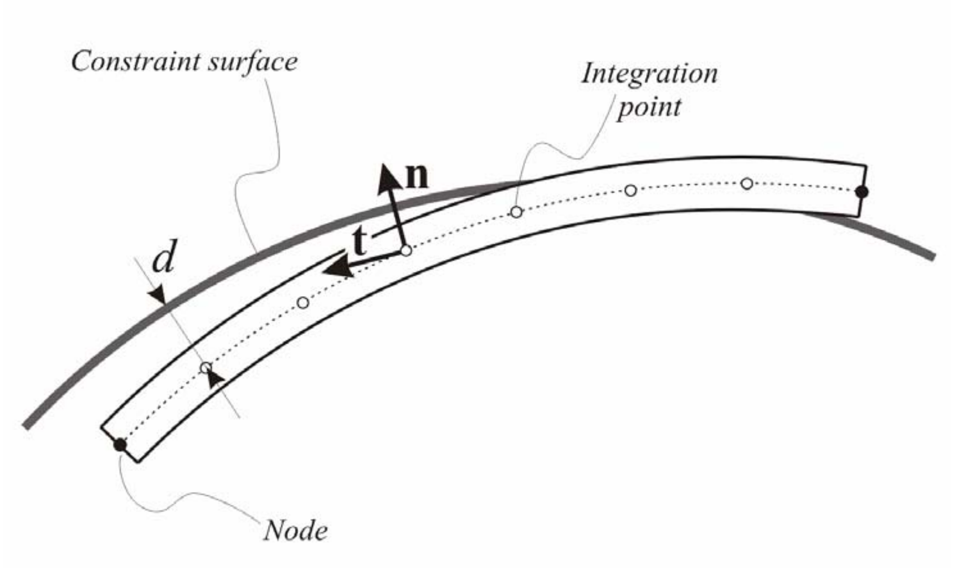

Figure 3.2 Description of the distributed contact forces.

Contact searching is executed through evaluation of the penetration distance d of an arbitrary particle in the centerline of the element, which can be defined using the following equations:

$$d = R - \sqrt{\left(\mathbf{r} - \mathbf{r}_O\right)^T \left(\mathbf{r} - \mathbf{r}_O\right)}\,. \tag{3.21}$$

In Equation (3.21) R is the radius of the circular constraint, $\mathbf{r}$ the location of an arbitrary particle in the centerline of the element, which can be evaluated using the shape function and the vector of the nodal coordinates of the element and $\mathbf{r}_O$ is the location of the center of the constraint in the global coordinate system. Superscripts that refer to the number of elements have been eliminated for simplicity.

The normal unit vector **n** to the surface of the circular constraint can be expressed as follows:

$$\mathbf{n} = \frac{\mathbf{r} - \mathbf{r}_O}{\sqrt{\left(\mathbf{r} - \mathbf{r}_O\right)^T \left(\mathbf{r} - \mathbf{r}_O\right)}}\,. \tag{3.22}$$

In the Coulomb model, tangential forces due to friction are point-wise proportional to the modulus of the normal forces. However, considering the pure Coulomb model, the integration of the equation of motion results in a cumbersome process. The use of a tri-linear creep-rate law that depends on the relative velocity between the contacting surfaces alleviates the friction model difficulties; therefore, the resulting system of equations is, in a computational sense, less expensive to integrate.

The tangential friction force is governed by the creep-rate dependent frictional law and can be expressed as follows:

$$\mathbf{f}_t = -\mu(v_t)\left\|\mathbf{f}_n\right\|\mathbf{t}\,. \tag{3.23}$$

In Equation (3.23) $\mathbf{f}_t$ is the distributed tangential friction force, $\mu(v_t)$ is the friction coefficient that depends on the relative tangent velocity v_t. In addition, $\mathbf{t}$ is the unit vector perpendicular to the normal $\mathbf{n}$ as shown in Figure 3.2, and can be calculated as

$$\mathbf{t} = \tilde{\mathbf{I}}\mathbf{n}, \tag{3.24}$$

where $\tilde{\mathbf{I}}$ can be written as introduced in Equation (3.6). The tangent relative velocity between the surfaces in contact can be calculated in a straightforward manner since the pulleys are assumed to rotate around their center of masses. Assuming that the angular velocity of the pulley is ω, the relative tangent velocity of an arbitrary particle in the centerline of the element can be written as follows:

$$v_t = \mathbf{t}^T(\dot{\mathbf{r}} - \omega R\mathbf{t}). \tag{3.25}$$

The dependency of the friction coefficient on the tangent velocity is shown in Figure 3.3.

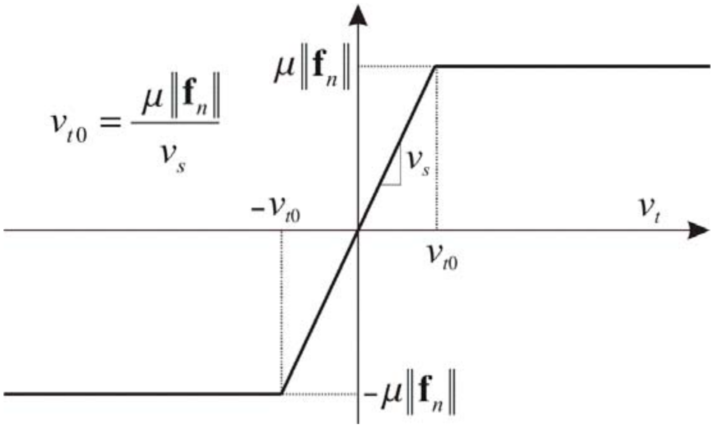

Figure 3.3 Tri-linear creep-rate dependent law [23].

The parameter v_s in Figure 3.3 is the slope of the friction force with respect to tangent velocity at small sliding velocities. The angular velocity ω of the pulley is usually an explicit function of time for a driver pulley. In contrast, for a driven pulley, the moment equilibrium equation can be included in the system of equations of motion considering the angle rotated by the pulley as a generalized coordinate. This equation can be written as follows:

$$I\ddot{\theta} = \sum_{i=1}^{n} \int_{0}^{l_i} \left((R-d)\mathbf{n} \times (-\mathbf{f}_t) \right)_i dx + T_a \,. \tag{3.26}$$

In Equation (3.26) I is the mass moment of inertia of the driven pulley, $\ddot{\theta}$ the angular acceleration, index i refers to the number of elements, l_i the length of the element i and T_a the possible opposing torque applied by the driven accessories on the constraint.

It is important to note that the model does not place any restriction for the possible slippage of a particle in the centerline. The use of the slopes as nodal coordinates enables the element to adopt curved configurations. Due to this feature the normal and friction forces can be different from particle to particle and, indeed, it should be possible to find areas of slippage and areas of sticking within the same element. However, only the kinetic friction is applied in the model excluding the existence of adhesion in the contact regions of the belt and the pulleys [23].

The virtual work done by the frictional contact forces can be used to obtain the expression of the generalized frictional contact forces. Thus the virtual work of the friction forces can be written as

$$\delta W = \int_{0}^{l} \delta \mathbf{r}^{T} \left(\mathbf{f}_n + \mathbf{f}_t \right) dx = \delta \mathbf{e}^{T} \int_{0}^{l} \mathbf{S}_0^{T} \left(\mathbf{f}_n + \mathbf{f}_t \right) dx = \delta \mathbf{e}^{T} \mathbf{Q}_c \,, \tag{3.27}$$

where $\mathbf{S}_0$ is the shape function matrix of the element evaluated at the centerline of the beam element, that is, $y = 0$ and $\mathbf{Q}_c$ the generalized contact force vector. The integral in Equation (3.27) is complicated to evaluate symbolically and, for this reason, a Gaussian quadrature integration formula is employed to solve the integral of the virtual work. Since the normal and friction forces are not smooth functions, a high enough number of integration points must be used. In addition, the number of integration points is related to the accuracy of the definition of the slippage area of the element, as long as the information of sliding is obtained at the integration points.

In the finite element assembling procedure, the distributed contact forces are converted to the generalized friction contact forces (i.e. equivalent nodal force) as expressed in Equation (3.27). This is accomplished using the shape function matrix and it is a crucial step if the belt is modeled using a low number of elements. Naturally, in the finite element sense, the use of the distributed contact force could be replaced by a large number of discrete forces [11, 23, 25]. The use of the distributed contact forces with the high order elements allows reducing the number of elements and, therefore, the number of degrees of freedom since the curving of the elements into the circular shape of the pulley is no longer *vis major*. It is worth remarking the importance of using a small number of elements to model the contact between the pulley and the belt. The reason being that in belt and pulley applications, the distance between the centers of the pulleys, the span length, is usually much larger than the arc length of the pulleys. It is also usual that the pulleys are very different in size because of changes in velocities and torques. In this case, the smallest pulley forces to use an excessive number of elements for the larger one. Hence the total number of elements in the model can be considerably decreased with a reduction in the number of elements needed per pulley. Since, when using the Lagrangian mesh, all the elements of the belt have to come in contact with the pulleys sooner or later, there is no possibility to use different element lengths.

When using the absolute nodal coordinate formulation, it is also easy to detect the possibility of the element contact before the contact calculation procedure. Then, if the element cannot be in contact with a pulley due to its location in the middle of one of the spans, there is no reason to check the forces in the integration points. Neither is there need to find the limits of the contact area *a priori* since eventually the integration point is checked when evaluating the integral in Equation (3.27). Based on these features, the proposed model leads to the inclusion of contact in a systematic manner using a set of external forces.

3.3 Numerical Examples of the Two-Dimensional Belt-Drive

In this section, the applicability of the absolute nodal coordinate formulation in the modeling of belt-drives is demonstrated using static and dynamic examples. The belt is discretized using elements that are straight in their initial configuration. Thus once the belt is forced over the surface of the pulleys it is expected to have some initial stresses. Then, it is easy to imagine that if the belt were released from the pulleys, it would obtain a circular shape in the equilibrium configuration due to the bending stiffness even if it has been reduced, as long as all the elements have the same properties.

In order to show the capabilities of the absolute nodal coordinate formulation, a static analysis is carried out to find the equilibrium configuration. In this example, the belt is studied without the pulley contact. The material of the belt is assumed to have a Young's modulus of $1.0 \cdot 10^8$ N/m^2, a Poisson's ratio of 0.3 and a mass density of 1,036 kg/m^3. The cross-section of the belt is a 0.01-m-sided square and the length of the belt is assumed to be 1.276 m. Since the static analysis involves the numerical solution of a nonlinear system of equations, an initial estimation of the solution is needed. In this analysis, the initial configuration of the belt is working conditions, which can be seen in Figure 3.4. In this configuration, the global coordinates of the centers of the pulleys, O_1 and O_2, are (-0.191441 m, 0.0 m) and (0.191441 m, 0.0 m), respectively, and the radiuses R_1 and R_2 of the pulleys are 0.08125 m.

In order to carry out the static analysis, the rigid body motion of the belt must be constrained. To this end, point A of the belt is constrained by boundary conditions that eliminate the horizontal and vertical displacement. In addition, the boundary conditions are given to eliminate vertical displacement of the node in point *B*, as shown in Figure 3.4. The belt is discretized using ten elements leading to 60 degrees of freedom while the axial and the bending stiffness of the elements are affected by the parameters $\alpha_1 = 1$ and $\alpha_2 = 0.01$. In Figure 3.5, four different configurations of the belt corresponding to different iterations of the Newton-Raphson procedure are shown. As can be seen, when convergence is achieved, the configuration of the belt is fully circular as expected. It is important to note that the use of only 10 elements enables an accurate representation of the initial configuration, iteration 1 in Figure 3.5, and a perfect circle after convergence, iteration 55 in Figure 3.5.

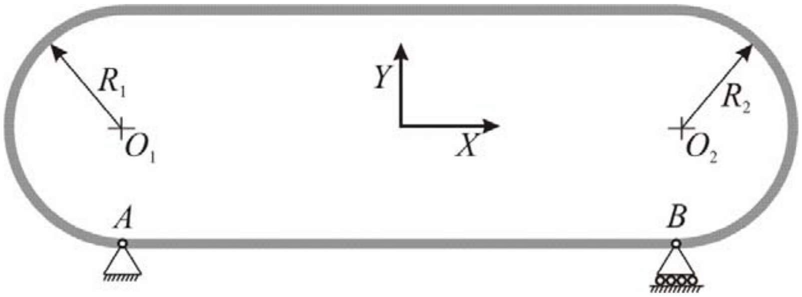

Figure 3.4 Sketch of the belt in the initial configuration.

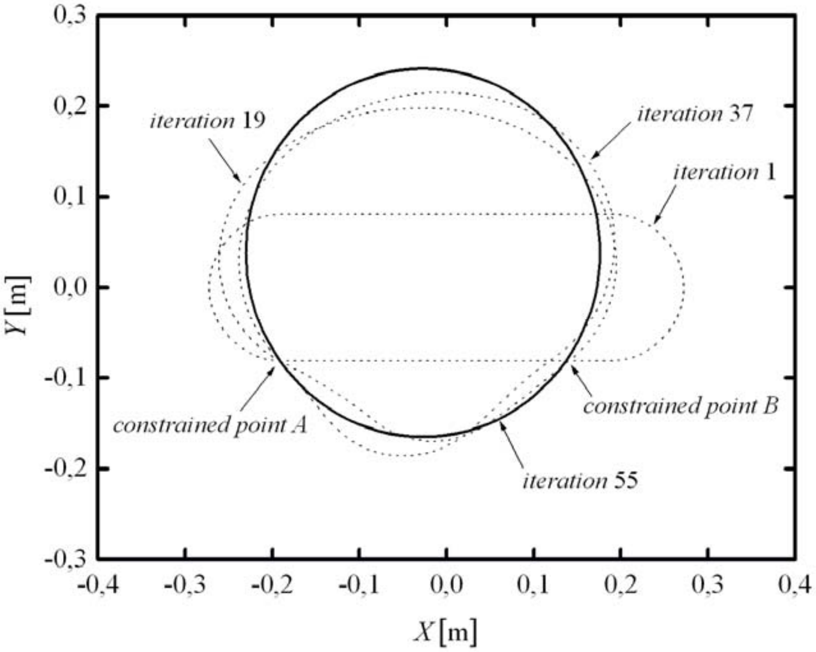

Figure 3.5 Four shapes of the belt during the iteration process of the static analysis.

The use of a set of global variables as nodal coordinates is an advantage in the treatment of contact with fixed boundaries. This is due to the fact that the evaluation of the entities involved in contact, such as penetration or normal vectors, can be estimated in a very straightforward manner. In fact, the pulleys can be treated as circular boundaries, which are in contact with the belt. In addition, the absolute nodal coordinate formulation uses a global measure of deformations and does not use reference conditions. Thus the absolute nodal coordinate formulation appears to be a very suitable approach for the modeling of belt-drives.

In the following examples the performance and the applicability of the absolute nodal coordinate formulation for modeling the belt-drive systems is studied using a simple two-pulley belt-drive system shown in Figure 3.6. Two identical pulleys compose the belt-drive with similar values for center locations O_1 and O_2, and radiuses, R_1 and R_2, as in the static example. However, in order to generate an initial normal force between the pulleys and the belt that allows the frictional forces to transmit the motion, the used length of the belt, 1.2727 m, is slightly smaller than in the static example. The parameters of the belt-drive system are shown in Table 3.1.

Lagrange equations can be used to obtain the equations of motion of the belt-drive system. In this study, the belt is essentially treated as a beam or a plate whose ends are joined together forming a closed loop structure. Due to the use of absolute nodal coordinates, the constraints that come from the rigid joint are linear. These linear constraints can be added to the equations of motion by the use of Lagrange multipliers. It is worth remarking the convenience of using the absolute nodal coordinate formulation when dealing with the Jacobian of the elastic forces [59]. From Equation (2.32), it is possible to eliminate the Lagrange multipliers and write the acceleration vector of the nodal coordinates as follows:

$$\begin{aligned}\ddot{\mathbf{e}} &= \left[\mathbf{M}^{-1} - \mathbf{M}^{-1}\mathbf{C}_e^T\left(\mathbf{C}_e\mathbf{M}^{-1}\mathbf{C}_e^T\right)^{-1}\mathbf{C}_e\mathbf{M}^{-1}\right]\mathbf{Q} + \\ &\quad + \left[\mathbf{M}^{-1}\mathbf{C}_e^T\left(\mathbf{C}_e\mathbf{M}^{-1}\mathbf{C}_e^T\right)^{-1}\right]\mathbf{Q}_d = \mathbf{g}\left(\mathbf{e},\dot{\mathbf{e}},t\right)\end{aligned} \tag{3.28}$$

Since the mass matrix and the Jacobian of the constraints, if the linear constraints are not eliminated, are constant matrices, the terms in brackets in Equation (3.28) are constant during the evaluation of $\mathbf{g}(\mathbf{e}, \dot{\mathbf{e}}, t)$, which is a valuable feature of the absolute nodal coordinate formulation. This feature allows for calculating constant terms once in advance and evaluating $\mathbf{g}(\mathbf{e}, \dot{\mathbf{e}}, t)$ and, more significantly, its Jacobian with a small computational cost during the integration.

For belt-drive models, a further simplification of the equations of motion can be achieved when using absolute nodal coordinates since it is possible to eliminate the linear constraint equations in a straightforward manner. To this end, the first and last element of the belt can be defined in such a way that they share the coordinates of the common node. Thus, after eliminating the constraint equations, the system equations of motion can be simply written according to Equation (2.27). However, no excessive effort is required if the linear constraints are not eliminated. As can be seen, both Equations (2.27) and (3.28) present a very simple structure that facilitates the use of any standard integrator.

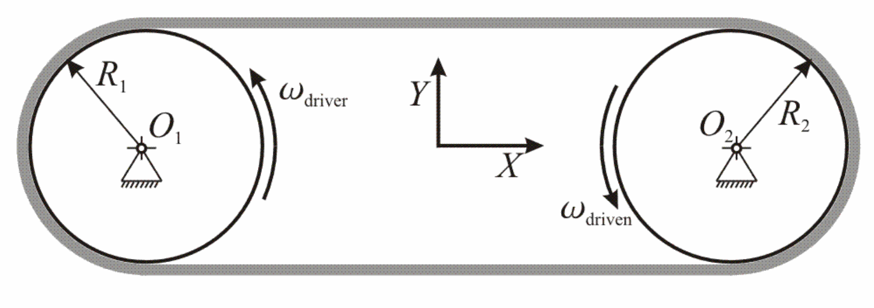

Figure 3.6 Two-pulley belt-drive system.

Table 3.1 Parameters of the studied two-dimensional belt-drive system.

Belt-drive parameter	**Symbol**	**Assigned value**
Radius of the driver pulley	R_1	0.08125 [m]
Radius of the driven pulley	R_2	0.08125 [m]
Span length	l_s	0.382882 [m]
Coordinates of the center of the driver pulley	O_1	(-0.191441, 0.0) [m]
Coordinates of the center of the driven pulley	O_2	(0.191441, 0.0) [m]
Density of the belt material	ρ	1036 [kg/m^3]
Zero-strain cross-section of the belt	A	0.01-m-sided square
Young's modulus	E	$1.0 \cdot 10^8$ [N/m^2]
Poisson's ratio	ν	0.3
Stiffness coefficient of the penalty spring-damper	k_p	$1.0 \cdot 10^7$ [N/m^2]
Damping coefficient of the penalty spring-damper	c_p	$1.0 \cdot 10^1$ [Ns/m^2]
Friction coefficient between the belt and the pulley	μ	1.2
Mass moment of inertia of the driven pulley	I	0.1 [kgm^2]
Friction creep-rate factor	v_S	$1.0 \cdot 10^5$ [kg/m·s]
Axial stiffness parameter	α_1	1.0
Bending stiffness parameter	α_2	0.01

The driven pulley only has freedom to rotate about its center and the angular velocity of the driver pulley is subjected to the following velocity profile:

$$\omega_{\text{driver}} = \begin{cases} 0, & \textit{if} \quad t \le 0.05 \\ 12\dfrac{t-0.05}{0.6-0.05}, & \textit{if} \quad 0.05 < t \le 0.6 \\ 12, & \textit{if} \quad 0.6 < t \end{cases} . \tag{3.29}$$

Due to Equation (3.29), the angular velocity of the driver pulley is linearly ramped from 0 to 12 rad/s in 0.55 seconds. After that, a constant driver pulley angular velocity is maintained until a final simulation time is reached.

Figure 3.7 shows the angular velocity of the driver and driven pulleys during the simulation for discretizations of different numbers of elements. As can be seen in the figure, the results obtained using 20 (120 degrees of freedom), 25 (150 degrees of freedom) and 30 (180 degrees of freedom) elements for the whole belt are practically equal. This observation indicates that convergence is achieved with a relatively low number of elements. Based on this result, the model of 20 elements is considered to be accurate enough for this study and is used in the following examples to introduce some comparisons. Thus the model uses only four elements (30 degrees of freedom) to discretize half of the pulley, which is significantly smaller than the number of elements and degrees of freedom used in the models of Leamy and Wasfy [1, 25].

The amplitude of the oscillations of the angular velocity of the driven pulley around the velocity of the driver pulley can be reduced if the stiffness of the belt is increased as shown in Figure 3.8. Two different values of the Young modulus, $1.0 \cdot 10^8$ N/m^2 and $1.0 \cdot 10^9$ N/m^2, have been used to obtain the results shown in Figure 3.8, while the other parameters of the model have not been changed.

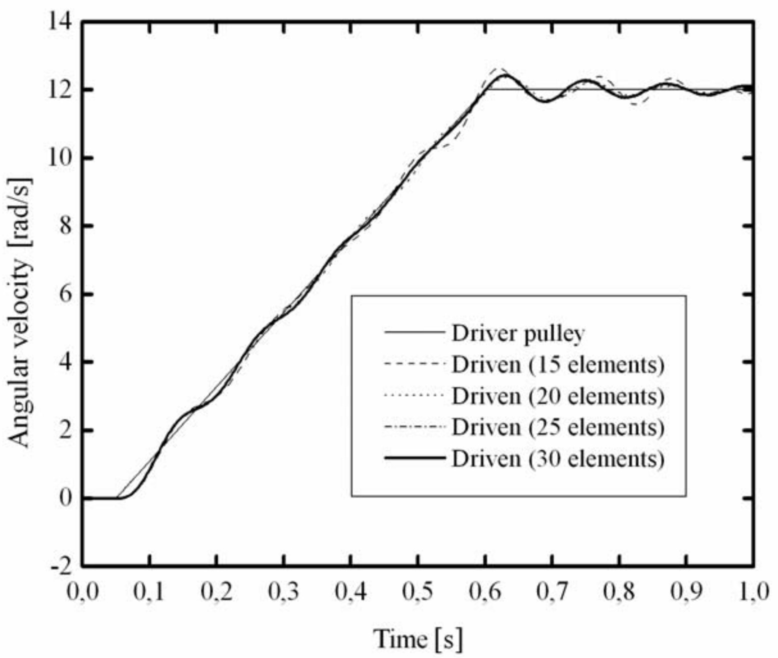

Figure 3.7 Angular velocities of the pulleys for different numbers of elements.

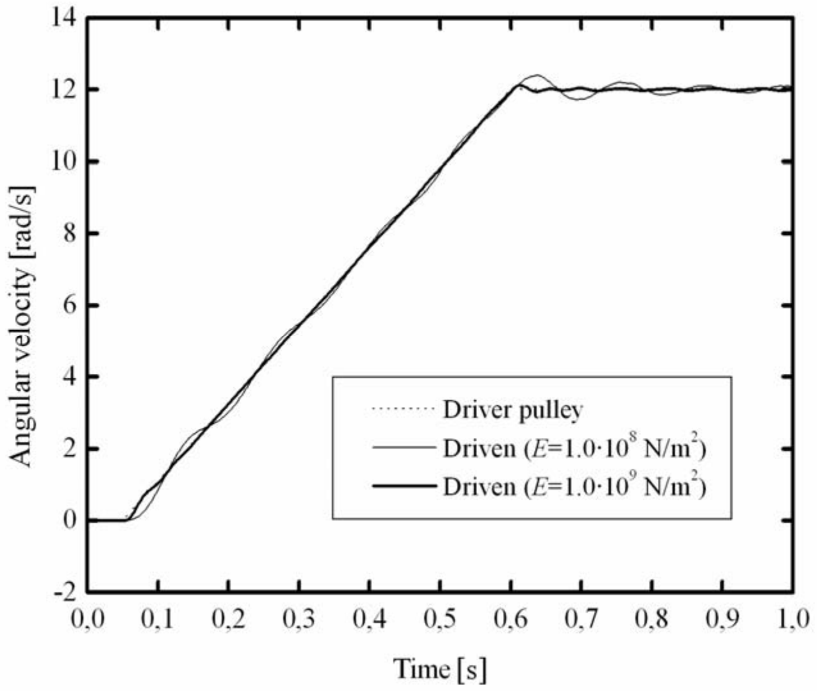

Figure 3.8 Influence of the stiffness of the belt.

Another important parameter of the model is the friction creep-rate factor v_S since small values of this parameter lead to a more computationally efficient integration procedure. However, the results can not be acceptable for certain values of v_S since it may lead to excessive slippage of the belt over the pulley and even the inability of the model to react to the changes of the angular velocity in the driver pulley. The results of two simulations using the elements with a Young modulus of $1.0 \cdot 10^9$ N/m^2 and two different values of v_S, $1.0 \cdot 10^4$ $\text{kg/m} \cdot \text{s}$ and $1.0 \cdot 10^5$ $\text{kg/m} \cdot \text{s}$, are shown in Figure 3.9. As can be observed from the figure, the smaller value of v_S conduces to a delay in the velocity of the driven pulley when the angular velocity is increasing while the higher value of v_S reduces the slippage leading to more accurate results.

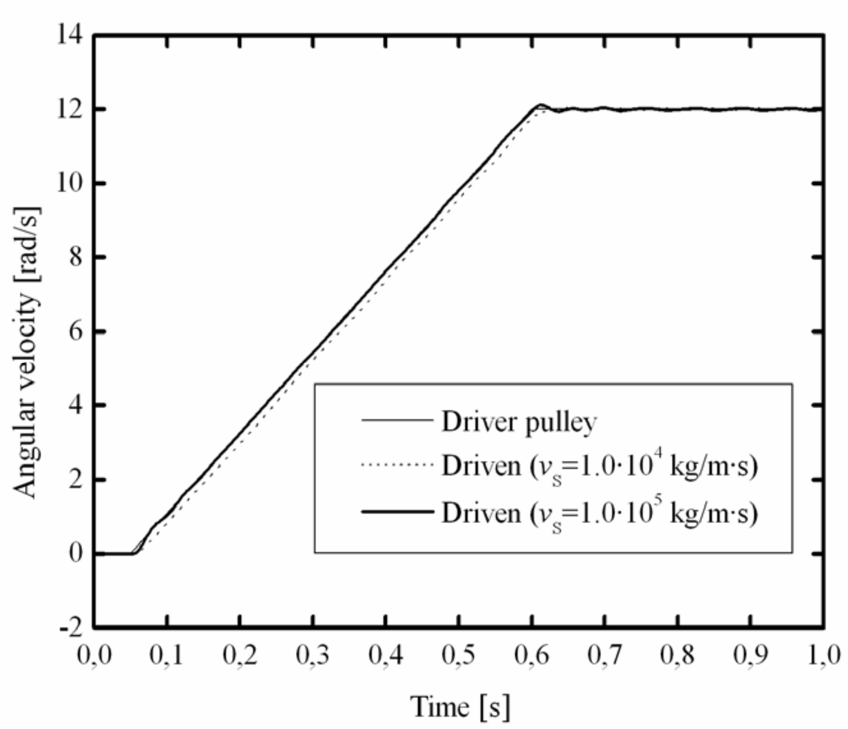

Figure 3.9 Influence of the parameter v_S.

In order to study the friction and normal force distributions over the belt length of the belt-drive, the opposite torque T_a is applied to the driven pulley. This torque is implemented using a trigonometric expression as follows:

$$T_a = \begin{cases} 0, & \mathit{if} \;\; t \le 0.05 \\ \dfrac{45}{2}\left(1 - \cos\dfrac{\pi t}{0.6}\right), & \mathit{if} \;\; 0.05 < t \le 0.6 \\ 45, & \mathit{if} \;\; 0.6 < t \end{cases} . \tag{3.30}$$

In this example, the angular velocity of the driver pulley is increased to the value of 120 rad/s, which is a typical running velocity in automotive applications. Furthermore, the initial length of 1.24437 m, parameter α_2 of 0.001 and the elastic modulus of $1.0 \cdot 10^9$ N/m^2 are used in this example. The time history response curves of the vertical position of the belt at the midpoint of the tight and slack spans for the belt-drive model are shown in Figures 3.10…3.11. When the belt-drive system is accelerated, the tight free span has larger vertical displacements than the slack free span. The vertical vibration of the belt is smoothly decreased for both spans after the driver pulley has obtained the final angular velocity 120 rad/s. The typical tensile force distributions of the belt during the acceleration and steady state are illustrated in Figure 3.12. As can be concluded from the tension distributions, the difference in the tension of the slack and tight free spans corresponds to the torque required by the opposing torque and the mass moment of inertia of the driven pulley. The changes of tensions at the inlet and exit regions of the pulleys exist as consequences of momentary accelerations and decelerations of the belt. However, these changes are essentially smoothed in the steady state.

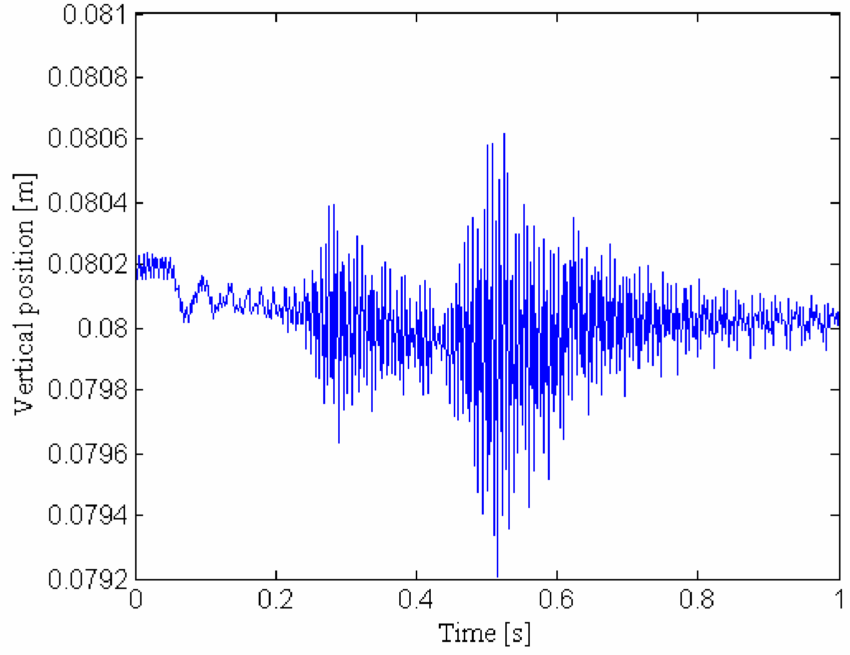

Figure 3.10 Vertical position of the midpoint of the tight span of the belt.

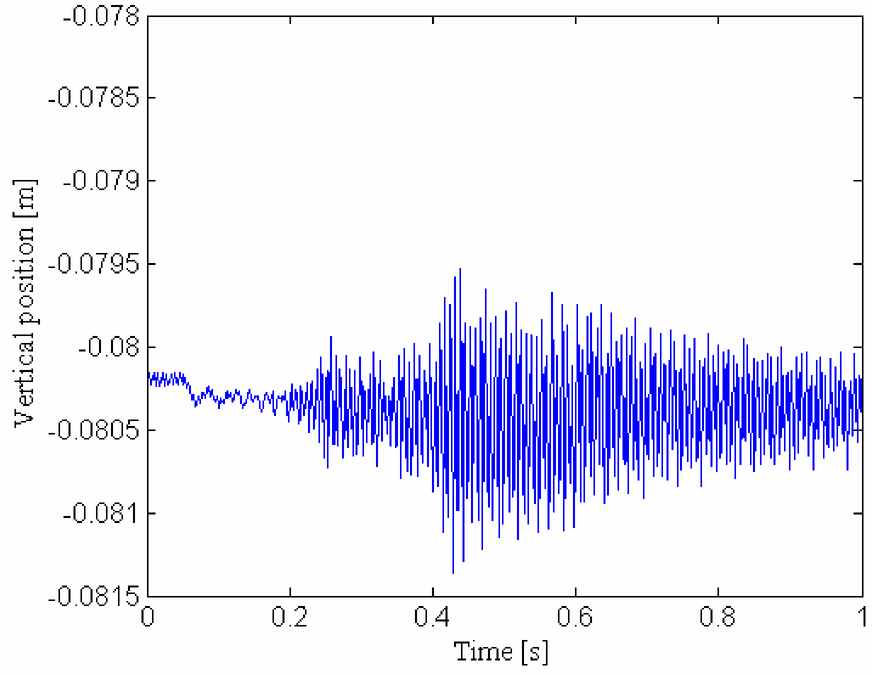

Figure 3.11 Vertical position of the midpoint of the slack span of the belt.

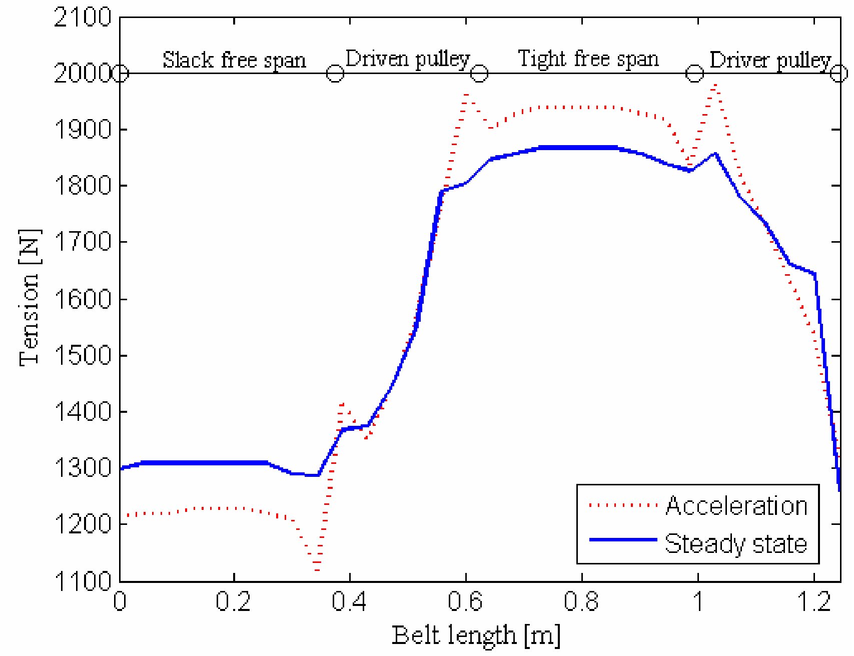

Figure 3.12 A belt tension in acceleration ($t = 0.428$ s) and in steady state ($t = 0.976$ s).

Figure 3.13 and Figure 3.14 illustrate the friction and normal force distributions over the belt length of the belt-drive when 30 elements (42 degrees of freedom per half a pulley) and the friction creep-rate factor of $1.0 \cdot 10^4$ kg/m·s are used. Correspondingly, Figure 3.15 and Figure 3.16 show force distributions when the friction creep-rate factor is increased to a value of $1.0 \cdot 10^5$ kg/m·s. The *x*-axis of the figures is the belt extended along the horizontal axis. The results have been taken at a simulation time of 1 second when the belt and pulley system under consideration has achieved the steady state running condition. As can be seen in the figures, the creep-rate factor plays an important role in terms of the normal and friction force distributions. When the friction creep-rate factor is $1.0 \cdot 10^4$ kg/m·s, the force distributions have an approximately linear pattern with the exception of the tangential force distribution of the driver pulley. The force distributions become more nonlinear when the creep-rate factor is increased to $1.0 \cdot 10^5$ kg/m·s. This occurrence can be also found from the studies of Leamy and Wasfy [1, 23, 25]. In this study, however, the friction force has peaks on the arriving (inlet) and leaving (exit) zones of the driver pulley. This pattern is emphasized when the creep-rate factor increases. In the case of the large creep-rate factor, the peaks in the friction force distribution can be seen also in the driven pulley.

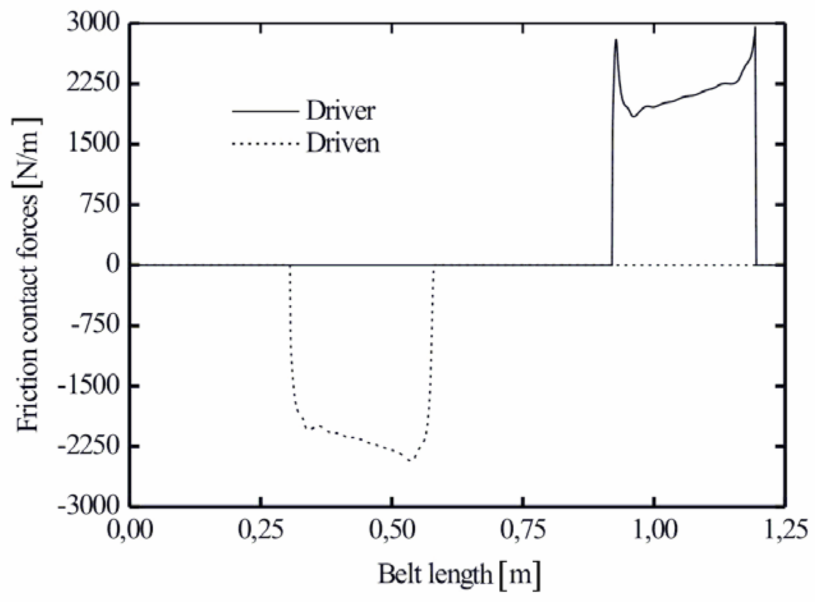

Figure 3.13 Friction forces for driver and driven pulleys, $v_S = 1.0 \cdot 10^4$ kg/m·s.

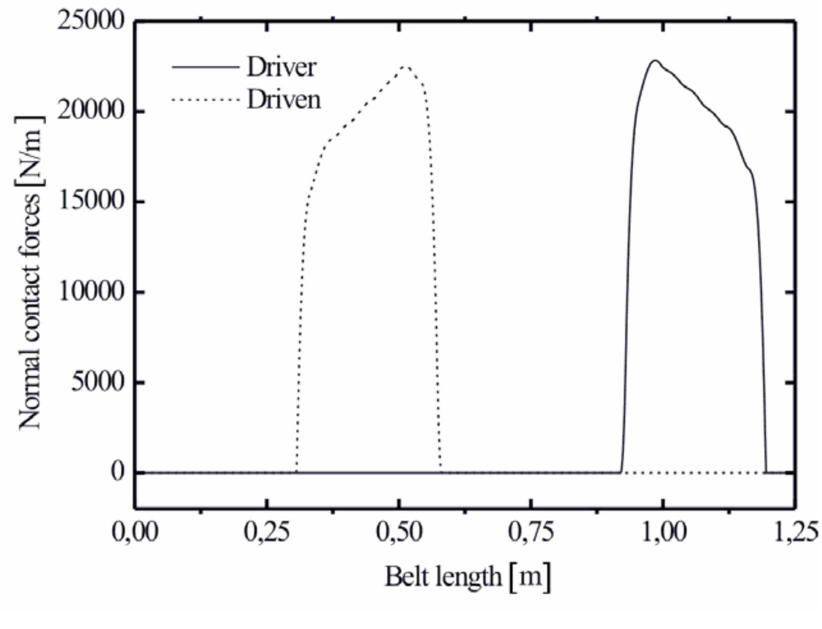

Figure 3.14 Normal forces for driver and driven pulleys, $v_S = 1.0 \cdot 10^4$ kg/m·s.

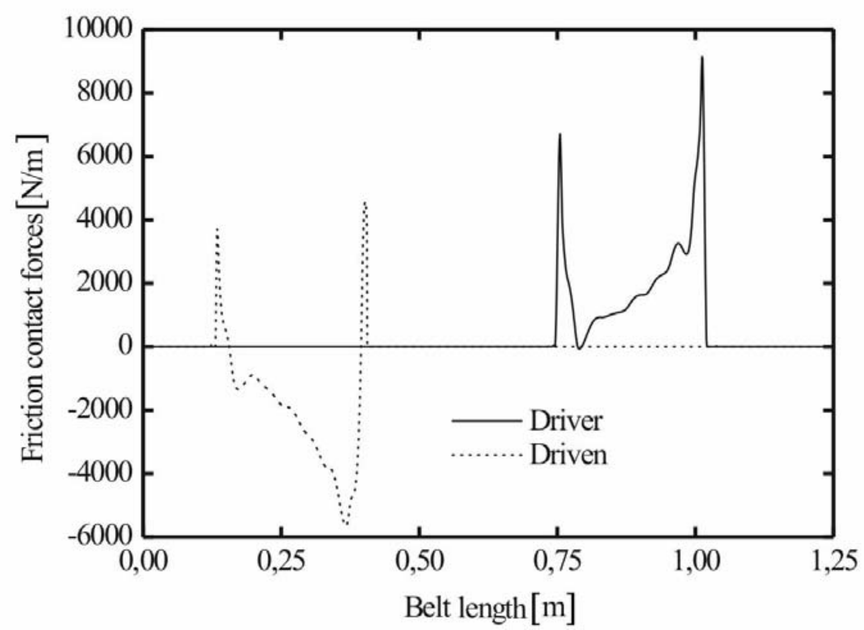

Figure 3.15 Friction forces for driver and driven pulleys, $v_S = 1.0 \cdot 10^5$ kg/m·s.

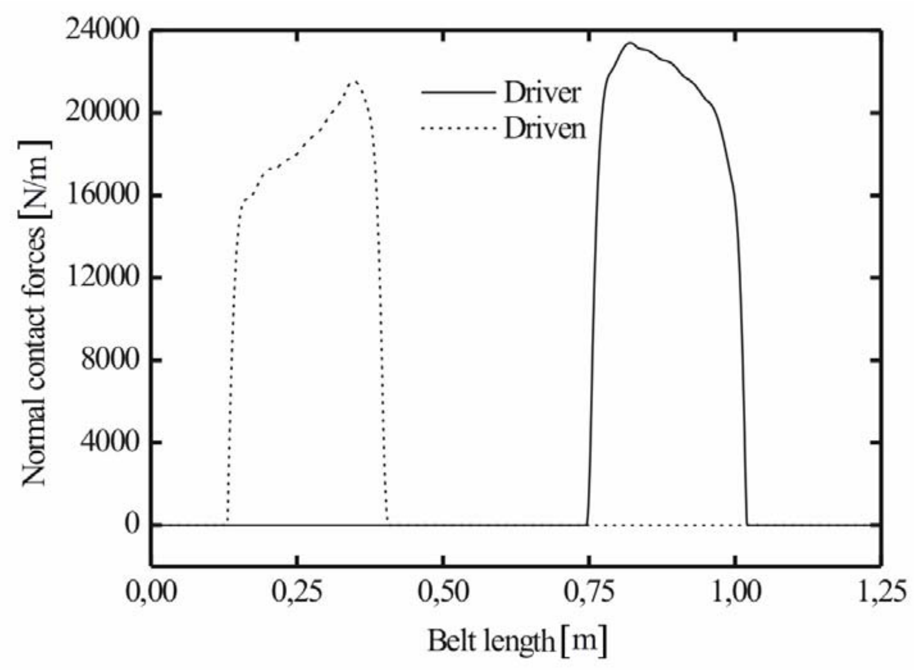

Figure 3.16 Normal forces for driver and driven pulleys, $v_S = 1.0 \cdot 10^5$ kg/m·s.

If the value of the friction creep-rate factor v_S is increased to $1.0 \cdot 10^5$ kg/m·s, the sign of the relative velocity between the belt and the surface of the driven pulley is changed at the inlet and exit regions of the driven pulley rapidly as illustrated in Figure 3.17. In the figure, the pulley arc coordinate is measured counter-clockwise from the inlet contact position. As a consequence, the sign of the friction force is changed due to the used tri-linear creep-rate dependent friction law. In the steady state, the belt slightly penetrates the pulleys and when a node first contacts and then penetrates the surface of a driven pulley, the activating *x*-component of a normal force slows down the velocity of the belt so that the velocity of the belt is temporarily less than the velocity of the surface of the driven pulley. In the exit regions, the movement of the belt from the pulley is opposed due to a damping force, which causes similar deceleration of the belt as in the inlet region. The change of the sign of friction force does not exist on the driver pulley, because the velocity of the surface of the driver pulley is permanently at least as high as the velocity of the belt. Neither does this feature exist if v_S has a value of $1.0 \cdot 10^4$ $\mathrm{kg/m \cdot s}$, because then the velocity of the surface of the driven pulley remains constantly and clearly slower than the velocity of the belt due to larger sliding. The angular velocities of the pulleys for different values of the parameter v_S are illustrated in 3.18.

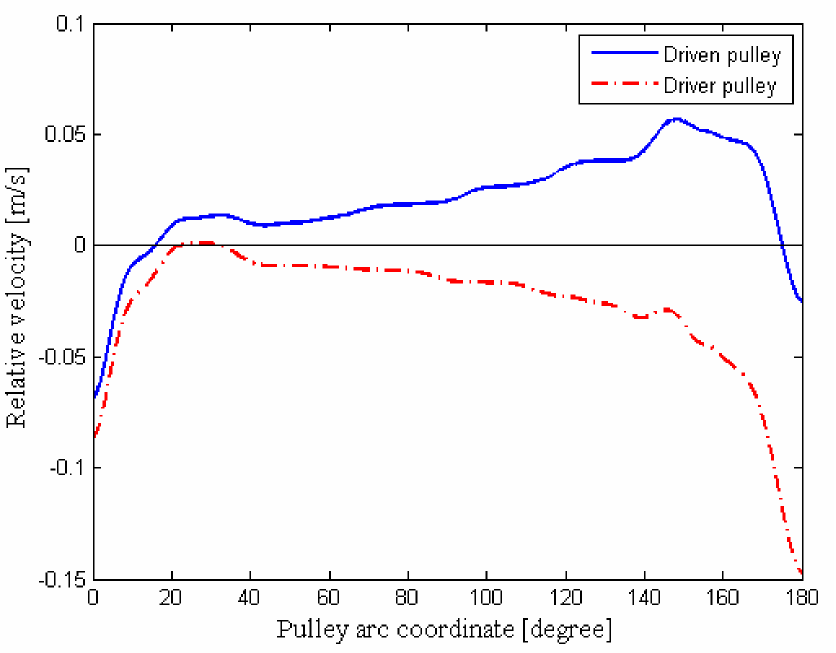

Figure 3.17 Relative velocities of the belt and the pulleys (t = 1 s).

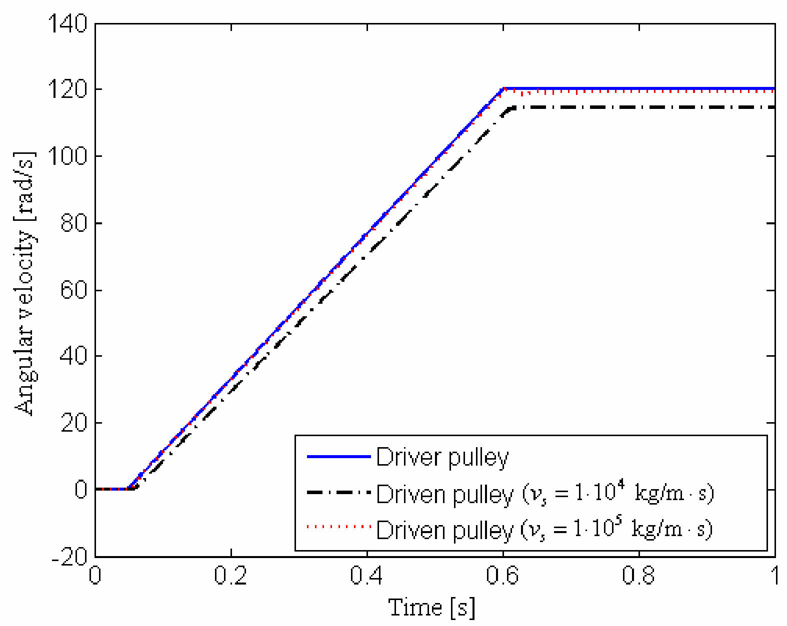

Figure 3.18 Angular velocities of the pulleys for different values of the parameter v_s .

Figures 3.19…3.20 illustrate the normal force distributions for driven and driver pulleys at five different time steps of the simulation. Based on these curves, the positions of the inlet and exit points of the contact area do not change significantly. Particularly, the steady state positions of the points remain very close to each other.

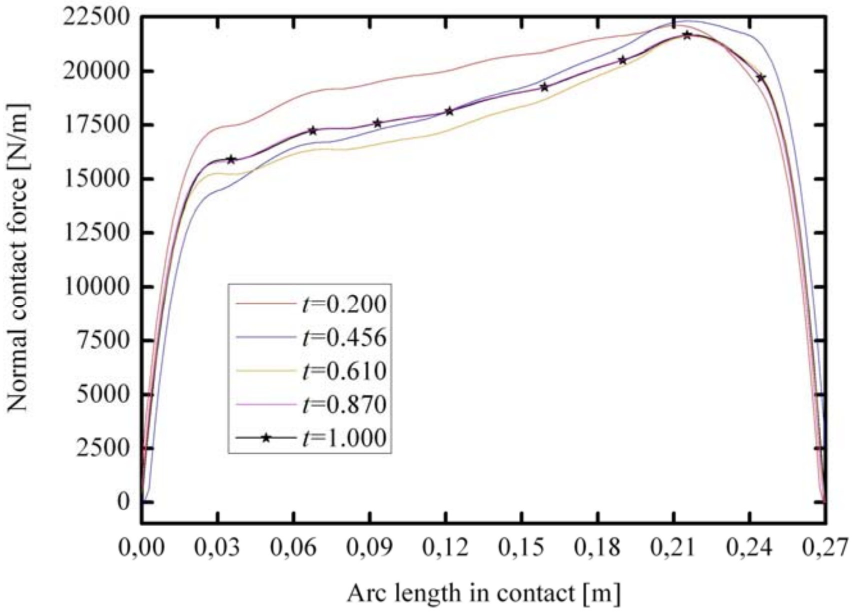

Figure 3.19 Normal force distribution for driven pulley at different time steps.

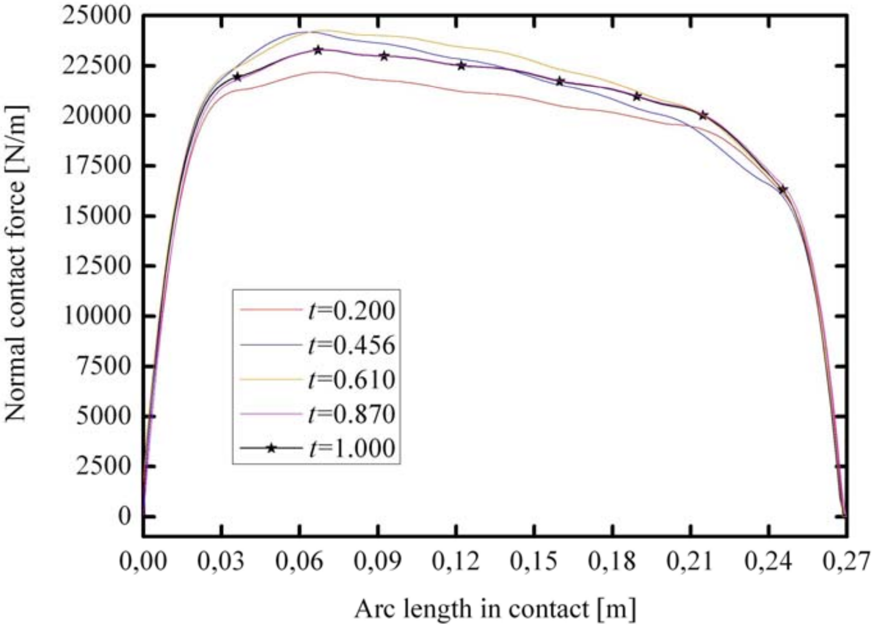

Figure 3.20 Normal force distribution for driver pulley at different time steps.

It is important to note that the belt and pulley system introduced by Leamy and Wasfy [1, 23, 25] is different from the one used in this study. In this study, the belt is assembled to the pulleys employing the initial strain while in the study of Leamy and Wasfy the assembling is accomplished by the spring tensioner. In addition, the interpretation of the friction creep-rate factor is different in this study as compared to the study of Leamy and Wasfy. In this study, the friction creep-rate factor is referred to as force per unit length being the distributed parameter. In the studies of the friction and normal force distributions, the number of integration points used in the evaluation of the generalized contact forces was varied. In these examples 5, 7 and 11 integration points produce identical solutions.

The proposed model is not restricted to pulleys with the same radius and it is capable of simulating different variations including, for example, more than two pulleys of different sizes. As an example, using the values of the first belt-drive simulation and changing only the radius of the driven pulley from 0.08125 m to 0.1218 m, it is possible to show that the quotient between the angular velocities approaches the inverse of the quotient of the radiuses, as it is expected. The result of this example is illustrated in Figure 3.21.

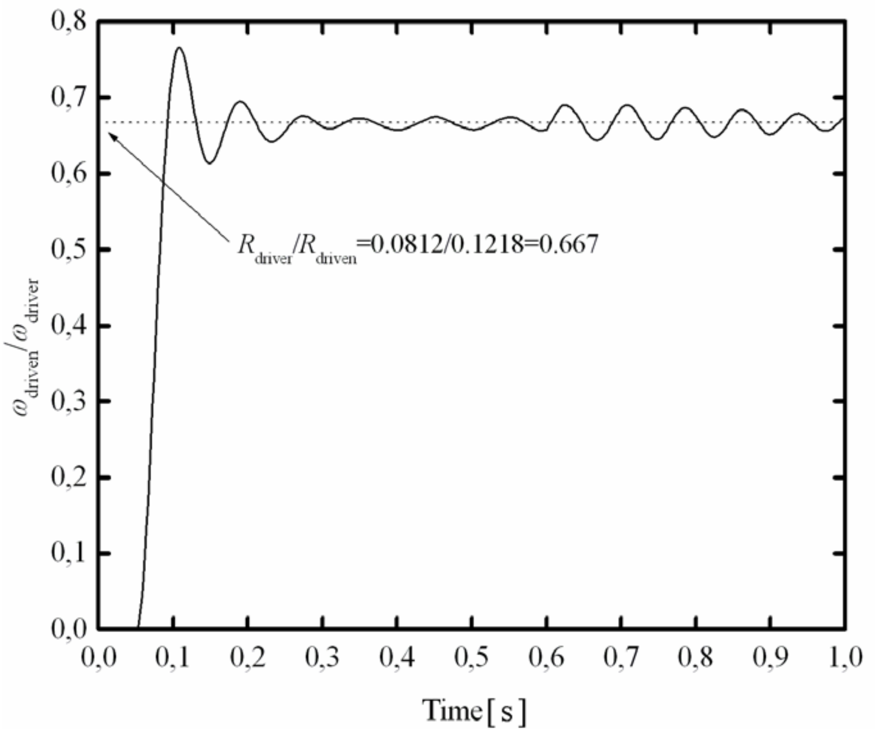

Figure 3.21 Quotient of the angular velocities of pulleys of different sizes.

As demonstrated by numerical examples in this section, the absolute nodal coordinate formulation is a potential approach to the analysis of the belt and pulley system. The use of the proposed computation procedure for the belt and pulley leads to reduced degrees of freedom as compared to previously proposed methods. It is noteworthy, however, that it is not a trivial task to find an objective measure for computational efficiency. Even often used CPU time can easily be misleading due to different implementation techniques. In the case of the absolute nodal coordinate formulation, a number of studies have recently been focused on the improvement of the numerical performance of the formulation [59, 60]. Utilizing these improvement proposals, the computer implementation of the absolute nodal coordinate formulation can be carried out more efficiently in a computational sense.

4 MODELING OF THREE-DIMENSIONAL BELT-DRIVES

It is important to point out that in the case of a wide elastic belt and pulleys that have large dimensions in the lateral direction, accurate modeling of the system can not be realized by using beam elements. This is mainly due to the fact that the nodes of beam elements as well as the integration points used to obtain the distribution of the contact forces are located on the centerline of the element. In order to be able to accurately describe the geometry of the contact regions, the finite elements used must allow a surface description in order to have integration points that can be used to obtain an accurate distribution of the contact forces [61].

The objective of this chapter is to develop more general formulations for the nonlinear dynamic finite element analysis of belt-drives by proposing three-dimensional belt-like beam and plate finite elements based on the absolute nodal coordinate formulation. The plate element relies upon a thin plate theory including the effect of geometric nonlinearities that arise from the large rotation and deformation of the belt. Bending stiffness can systematically be included in or excluded from the element formulation, thereby allowing the studying of the effect of bending on the nonlinear dynamics of the belt-drive system. The performance of the belt-like plate element formulation is examined by using a simple belt-drive system to study the angular velocities of the pulleys, speed and tension of the belt. The finite element solutions are also compared with the solutions obtained using simplified analytical techniques. The use of a cable element in the modeling of belt-drives is studied in Reference [61]. Due to the simplicity of the formulation of the cable element, the cable element based model [62] is more efficient compared to the beam element model. However, the cable element model does not include several deformation modes that are captured by the beam element, and therefore the use of the cable element in belt-drive models is limited.

4.1 Analysis of the Analytical Formulation for the Belt-Drive

In this section, an analytical formulation for the belt-drive is discussed and the main assumptions used in this analytical formulation are summarized in order to have an understanding of the basic differences between the simplified analytical formulation and the more general finite element solution presented later in this chapter. The material presented in this section is a summary of the work presented by Bechtel *et al.* [5], where a planar model for an extensible belt-pulley system, shown in Figure 4.1, is considered. The model includes the effect of inertia, including the acceleration due to stretching. Bechtel *et al.* [5] pointed out that it is important to include the effect of the change of the belt stretch since the tension is not uniform and the change in tension is accompanied by change in the strain. When the stretching acceleration term is included, the two momentum equations in the normal and tangential directions become coupled differential equations. In order to be able to solve these equations, one must specify the constitutive equation that relates the belt tension to the strain. The radius of the pulleys, the transmitted moment, the angular velocity of driving pulley, the initial tension in the belt, the stiffness of the belt, and the coefficient of friction between the belt and the pulleys are considered to be specified. Then the problem is solved for the angular velocity of the driven pulley, the belt tension and speed, the normal and friction forces with the slipping zones on the driving and driven pulleys. The belt dynamic equations are formulated in several regions including the slip and stick regions of contact between the belt and the driver and driven pulleys and the tight and slack free spans as shown in Figure 4.1.

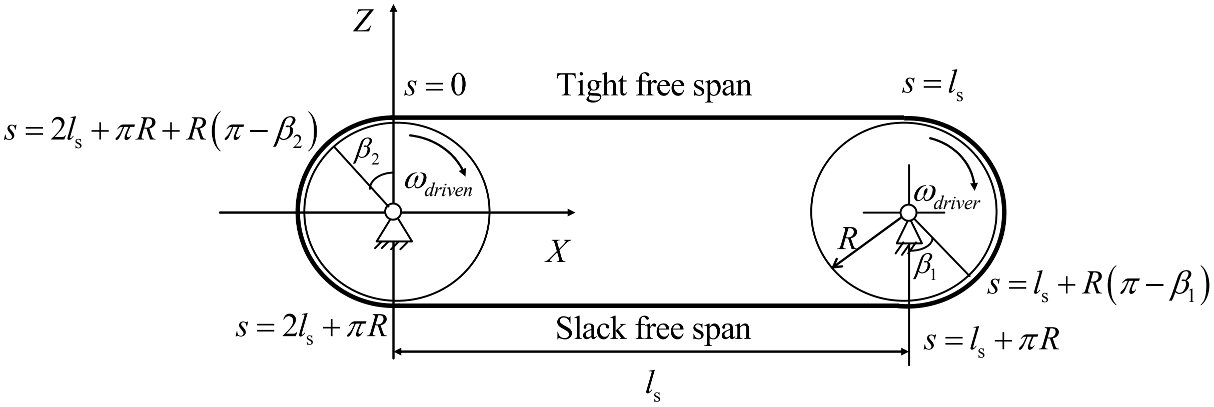

Figure 4.1 Assembly of the belt-drive mechanism [5].

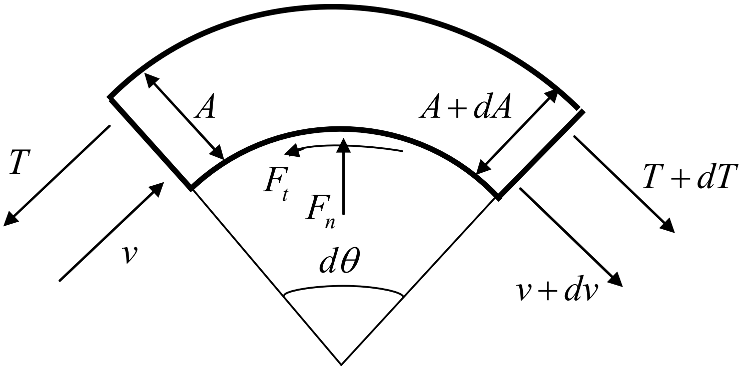

Figure 4.2 Portion of belt on pulley [5].

The analytical equations for determining the belt tension and speed at different contact zones and free spans for given values of the velocities in terms of the angular velocities of the pulleys are briefly introduced in the following. In the analytical solution, it is assumed that the motion is steady in such a way that the conditions at location *s* shown in Figure 4.1 are independent of time.

A free-body diagram of a portion of the belt of length *ds* at location *s*, subtending an angle *dθ* is shown in Figure 4.2. The relationship between the axial force and speed of the belt can be written as follows [5]:

$$T(s) = T_o + k\left(\frac{v(s)}{v_o} - 1\right). \tag{4.1}$$

In Equation (4.1), *T* is the axial strain in the belt (T_o in the reference state), *k* an elastic modulus with units of force, *v* the speed of the belt (v_o in the reference state) and *s* the location of a portion of the belt.

The following equation can be determined from the equilibrium of the forces in the tangential and normal directions in a portion of the belt:

$$\frac{d(T - Gv)}{T - Gv} = \pm \mu d\theta\,. \tag{4.2}$$

In Equation (4.2), G is the mass flow rate, $d\theta$ an infinitesimal bending angle of a portion of the belt and μ the coefficient of friction. Equations (4.1) and (4.2) can be solved to determine the belt tension and speed at different contact zones.

A free-body diagram of a portion of the belt of length ds at s in the free span is illustrated in Figure 4.3. An equilibrium of the forces leads to

$$T = Gv + c, \tag{4.3}$$

where c is a constant of integration. Note that the constitutive relationship of Equation (4.1) can be written as follows:

$$T(s) = T_o + \left(\frac{k}{v_o}\right) v(s) + (T_o - k). \tag{4.4}$$

By comparing the preceding two equations one can conclude that the mass flow rate G will not, in general, be equal to the elastic modulus divided by the reference speed. Therefore, the values for T and v in the free spans must be constant.

The values of T and v for a portion of the belt in the free span can be determined by solving Equations (4.3) and (4.4). The solutions obtained are presented in detail in the literature [5].

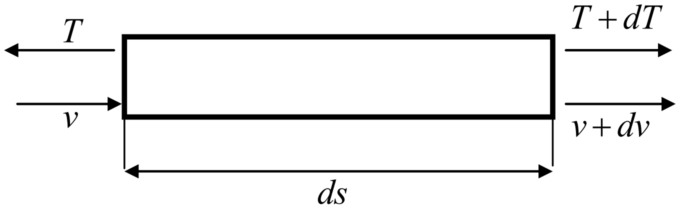

Figure 4.3 Portion of belt in a free span [5].

The equations of the belt when it is in contact with the pulleys and during the free span motion can be solved to obtain the belt tension and speed for a given radius of the pulleys, a transmitted moment angular velocity of the driving pulley, the initial tension in the belt and the coefficient of friction. The belt tension and speed as a function of the belt length obtained using the analytical model summarized in this section are shown in Figures 4.4 and 4.5. The data used for this model are according to Model 2, shown in Table 4.1. The results presented in these figures are obtained assuming a belt stiffness *k* equal to 25 kN.

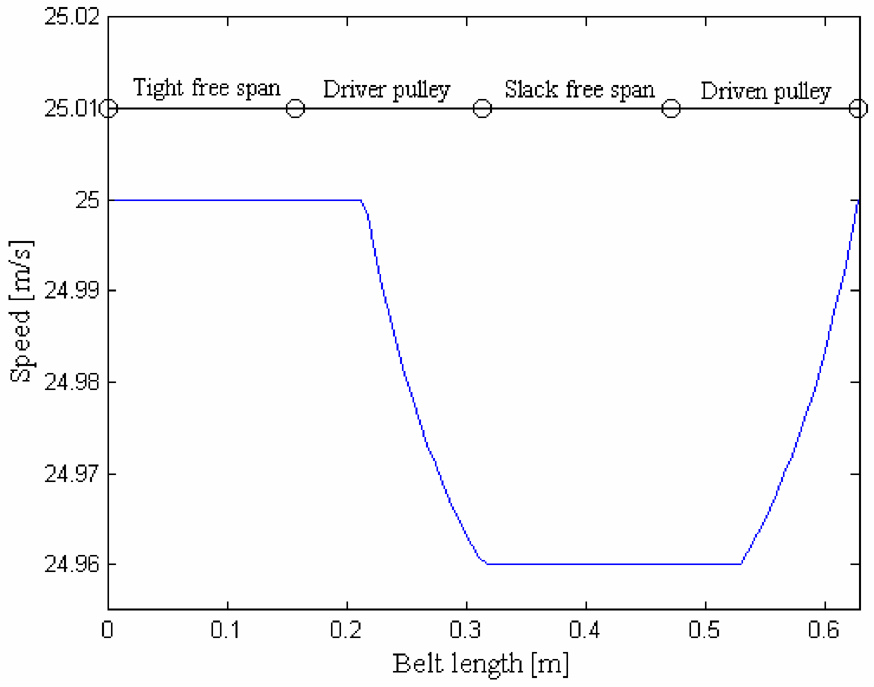

Figure 4.4 Analytical results of the belt speed for a stiff belt (k = 25 kN), Model 2 [5].

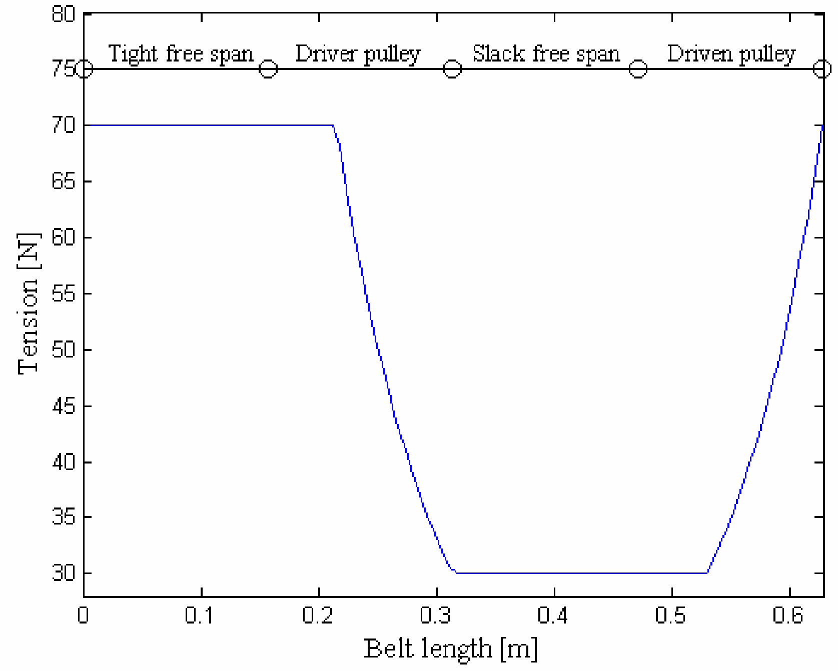

Figure 4.5 Analytical results of the belt tension for a stiff belt (k = 25 kN), Model 2 [5].

The following features of the analytical model can be listed from the formulations and results presented in this section and from the more detailed analysis presented in [5] [61]:

1. It is assumed that the motion is steady so that the conditions at location s are independent of time.

2. The normal belt acceleration is always zero and there is no separation between the belt and the pulleys. This assumption allows obtaining an algebraic equation for the equilibrium of the forces in the normal direction.

3. There is no sliding of the belt on the pulleys in the no slip zone. This assumption allows using simple boundary conditions to solve the resulting belt equations.

4. The tension and speed in the free spans are constant. These assumptions must hold as the result of the used equilibrium and constitutive equations.

5. The belt bending and other deformation modes, except for the extension, are neglected.

6. The analytical formulation is limited to a simple configuration in which the dynamics can not be a function of more general displacements of the pulleys and belt.

In order to eliminate some of the limitations of the analytical model, more general finite element formulations that can be implemented in flexible multibody algorithms are used in this study.

Table 4.1 Parameters of the studied belt-drive system.

Belt-drive parameter	**Assigned values, Model 1**	**Assigned values, Model 2**
R	0.10 [m]	0.05 [m]
l_s	πR [m]	πR_p [m]
l_{belt}	$4\pi R$ [m]	$4\pi R_p$ [m]
w	0.08 [m]	0.04 [m]
h	0.01 [m]	0.003 [m]
k_p	$1.0 \cdot 10^7$ [N/m^3]	$8.0 \cdot 10^7$ [N/m^3]
c_p	2000 [Ns/m^3]	2000 [Ns/m^3]
v_s	$1.0 \cdot 10^5$ [kg/m$^2 \cdot$ s]	$2.0 \cdot 10^5$ [kg/m$^2 \cdot$ s]
μ	1.2	0.6
ρ	1036 [kg/m^3]	166.667 [kg/m^3]
v	0.3	0.3
t_0	0.05 [s]	0.05 [s]
t_1	0.60 [s]	1.00 [s]
ω_0	12.0 [rad/s]	500.0 [rad/s]
I	0.25 [kgm^2]	0.00025 [kgm^2]

4.2 Correlation with the Finite Element Solution

A three-dimensional belt-like large deformation nonlinear finite plate element formulation is considered in this study. In the formulation, a thin plate element with four nodes and 36 nodal coordinates is used. In order to draw a correlation between the simplified analytical formulation discussed in the preceding section and the more general computational finite element formulation to be presented in the following sections, one must be able to obtain the tension, i.e. the axial force T and the speed v of the particles on the belt. The finite element coordinates and their time derivatives are readily available from the solution of the differential equations of motion. Using the coordinates and the assumed shape functions of the finite element, one can obtain the Green-Lagrange strain tensor $\boldsymbol{\varepsilon}^m$ of Equation (2.14) at an arbitrary particle on the element.

It is important to note that in belt drive applications, the belt has an initial stress field and possible pre-tensioning when it is wrapped over the pulleys. In order to introduce the initial stress of the element, the reference configuration used in Equation (2.13) is taken as the initial undeformed element configuration. From continuum mechanics theory, the Green-Lagrange strain tensor must satisfy the following equation [32]:

$$\frac{1}{2}\left\{\left(\frac{dl(s)}{dl_o}\right)^2 - 1\right\} = \mathbf{t}_o^T \boldsymbol{\varepsilon}^m \mathbf{t}_o, \tag{4.5}$$

where $dl(s)$ is the length of an infinitesimal portion of the belt at location s, dl_o is the length of the portion in the reference state and $\mathbf{t}_o$ is a unit vector along which dl_o is measured. In the case of the belt drive, $\mathbf{t}_o$ is considered as the unit tangent vector $\mathbf{t}_o = \dfrac{\mathbf{r}_{o,x}}{\left\|\mathbf{r}_{o,x}\right\|}$ with the assumption that x is in the direction of the length s of the belt. Note that in the absolute nodal coordinate formulation, $\mathbf{r}_{o,x}$ is a vector defined in the global frame, which is the same frame in which the Green-Lagrange strain tensor is defined. The axial strain as a function of the length s can be written as follows:

$$\varepsilon(s) = \frac{dl(s)}{dl_o} - 1. \tag{4.6}$$

Using Equations (4.5) and (4.6), one can write the following quadratic equation for the strain:

$$\varepsilon^2 + 2\varepsilon - \alpha = 0, \tag{4.7}$$

where $\alpha = 2\mathbf{t}_o^T \boldsymbol{\varepsilon}^m \mathbf{t}_o$. The preceding quadratic equation has the following two solutions:

$$\varepsilon = -1 \pm (1+\alpha)^{\frac{1}{2}}. \tag{4.8}$$

The second solution is not physically possible because it does not represent a rigid body motion. Therefore, the strain ε can be evaluated using the components of the Green-Lagrange strain tensor obtained using the finite element solution as

$$\varepsilon = -1 + (1+\alpha)^{\frac{1}{2}}. \tag{4.9}$$

This equation will be used to define the belt stretch in the finite element model. Using the preceding equation and the longitudinal stiffness of the belt, one can define the belt tension used in the analytical formulation. One may also choose to use another definition of the strain, true strain ε^t, as follows:

$$\varepsilon^t = \frac{dl - dl_o}{dl}. \tag{4.10}$$

Following a similar procedure as the one used to obtain Equation (4.9), one can present the Almansi strain ε^A:

$$\varepsilon^A = -1 + (1+\alpha_A)^{\frac{1}{2}}, \tag{4.11}$$

where $\alpha_A = 2\mathbf{t}_t^T \boldsymbol{\varepsilon}^e \mathbf{t}_t$, $\mathbf{t}_t = \dfrac{\mathbf{r}_{,x}}{\left\|\mathbf{r}_{,x}\right\|}$ is the tangent defined in the current configuration, and $\boldsymbol{\varepsilon}^e = \dfrac{1}{2}\left(\mathbf{I} - \mathbf{D}^{-1^T}\mathbf{D}^{-1}\right)$ is the Eulerian or Almansi strain tensor. The use of the Green strain ε, true or engineering strain ε^t and Almansi strain ε^A will be examined in this study.

Similarly, the finite element solution can be used to define the velocity vector. In the absolute nodal coordinate formulation, the absolute velocity vector **v** of the particle on the element can be written as

$$\mathbf{v} = \dot{\mathbf{r}} = \mathbf{S}\dot{\mathbf{e}}, \tag{4.12}$$

and the velocity component v along the tangent to the belt can be obtained as follows:

$$v = \mathbf{t}_t^T \mathbf{v}. \tag{4.13}$$

A speed, i.e. the length of the tangential velocity obtained using the finite element solution, of the belt will be compared with the speed predicted using the simplified analytical formulation presented in this section.

4.3 Thin Plate Element Formulation

In this section, the plate element based on the absolute nodal coordinate formulation with 36 degrees of freedom is reviewed [63]. The global and local coordinates used to define the absolute position and gradient coordinates for this element are shown in Figure 4.6.

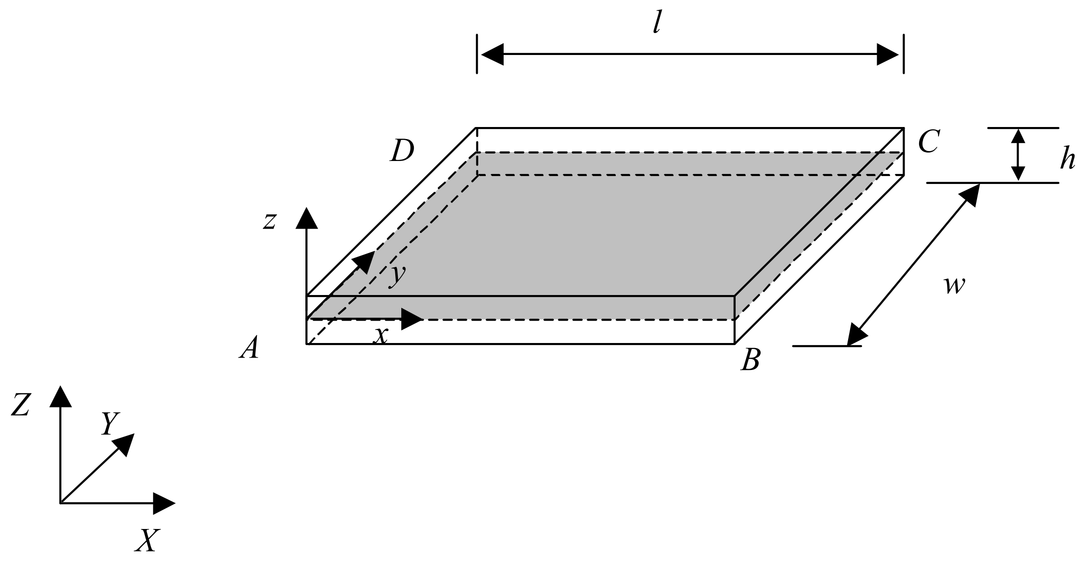

Figure 4.6 Plate element dimensions and coordinates [63].

The use of the thin plate assumption which does not consider the deformation along the element thickness is justified for the modeling of belt-drives. Using this assumption, one can develop a low order plate element with 36 degrees of freedom since the displacement field of the element becomes independent on the spatial coordinate z. It is important to note that the more general plate element which can capture shear deformation has 48 degrees of freedom [39]. The normal to the mid surface of the plate can be redefined using a cross product of the vectors $\mathbf{r}_{,x}$ and $\mathbf{r}_{,y}$, where subscripts x and y refer to partial derivatives. The nodal coordinate vector for node A of the low order plate element is defined as follows:

$$\mathbf{e}^A = \begin{bmatrix} \mathbf{r}^{A^T} & \dfrac{\partial \mathbf{r}^{A^T}}{\partial x} & \dfrac{\partial \mathbf{r}^{A^T}}{\partial y} \end{bmatrix}^T . \tag{4.14}$$

The vector of the element nodal coordinates can be written as follows:

$$\mathbf{e} = \begin{bmatrix} \mathbf{e}^{A^T} & \mathbf{e}^{B^T} & \mathbf{e}^{C^T} & \mathbf{e}^{D^T} \end{bmatrix}^T . \tag{4.15}$$

The continuity of the gradients at the interface between adjoined elements is not ensured due the nonconformity of the element. However, this disadvantage can be avoided if the shape functions are tailored for the element by applying the same technique as the one used for the general shell element based on the absolute nodal coordinate formulation [39].

4.3.1 The Elastic Forces of the Plate Element

As presented in Equation (2.20), the element strain energy can be used to construct the vector of elastic forces of the element. In the classical nonlinear plate theory [64] the strain energy density function is obtained by superimposing components from axial and bending stiffness and thereby neglecting the coupling between the axial and bending stiffness. The assumptions of Kirchhoff's thin plate theory lead to the plane stress conditions and deactivation of the effect of the transverse shear forces. Using the plane stress assumption, the bending stiffness is expressed in terms of the curvatures of the element mid plane [63, 65], the stress components along the thickness direction are assumed to be zero and the strains in the thickness direction are a function of the strains related to the element mid surface. In this study, belt material is assumed to be isotropic and the total strain energy is decomposed as the sum of strain energies due the axial elongation and the bending stiffness. The strain energy due to the axial elongation of the element can be defined as follows [64]:

$$U^{\varepsilon} = \frac{Eh}{2\left(1-\nu^2\right)} \int_A \left\{ \left(\varepsilon_{xx}^m + \varepsilon_{yy}^m \right)^2 - 2\left(1-\nu\right) \left(\varepsilon_{xx}^m \varepsilon_{yy}^m - \frac{1}{4} \varepsilon_{xy}^m \right)^2 \right\} dA \, . \tag{4.16}$$

The strain energy function due to the bending stiffness is written as follows [64]:

$$U^{\kappa} = \frac{D}{2} \int_A \left\{ \left(\kappa_{xx} + \kappa_{yy} \right)^2 - 2\left(1-\nu\right) \left(\kappa_{xx} \kappa_{yy} - \kappa_{xy}^2 \right) \right\} dA \, , \tag{4.17}$$

where D is defined as $Eh^3/12$. Nonlinear curvatures obtained using x and y coordinates are derived from elementary differential geometry and can be defined using the second derivatives of the position vector:

$$\kappa_{ij} = \frac{\mathbf{r}_{,ij}^T \mathbf{n}}{\|\mathbf{n}\|} \frac{1}{\|\mathbf{r}_{,i}\| \|\mathbf{r}_{,j}\|}, \quad i, j = x \text{ or } y, \tag{4.18}$$

where $\mathbf{r}_{,ij}$, where $i, j = x$ or y, are second derivatives of the position vector $\mathbf{r}$, $\mathbf{n}$ is the normal to the element mid surface, $\mathbf{n} = \mathbf{r}_{,x} \times \mathbf{r}_{,y}$ and the vectors $\mathbf{r}_{,x}$ and $\mathbf{r}_{,y}$ are gradient vectors defined by differentiation with respect to the x and y coordinates of the element, respectively.

Accordingly, the total strain energy function of the element is written as follows [63]:

$$U = U^{\varepsilon} + U^{\kappa}. \tag{4.19}$$

The bending stiffness may have an effect on the transverse vibrations and stability of the belt [25] although it is obvious that considerably thin belts are used in many applications and in such cases the role of the membrane stress is dominant.

4.4 Three-Dimensional Shear Deformable Belt Element Formulation

In this section, the formulations of two three-dimensional shear deformable beam elements are introduced in order to obtain elements which can be utilized in the modeling of V-belts. The first formulation is a three-dimensional generalization of the linear two-dimensional shear deformable beam element introduced in Chapter 2. Using the absolute nodal coordinate formulation, the global position vector $\mathbf{r}$ of an arbitrary particle in a spatial case can be written as

$$\mathbf{r} = \mathbf{S}(x, y, z)\mathbf{e}. \tag{4.20}$$

Nine nodal coordinates can be chosen for the node I of a two-node beam element as follows:

$$\mathbf{e}_I = \begin{bmatrix} \mathbf{r}_I^T & \dfrac{\partial \mathbf{r}_I^T}{\partial y} & \dfrac{\partial \mathbf{r}_I^T}{\partial z} \end{bmatrix}^T , \tag{4.21}$$

where vector $\partial \mathbf{r}_I^T / \partial z$ defines the orientation of the width coordinate of the cross-section of the beam [41]. Note that this three-dimensional element resembles the beam formulation introduced in Reference [46].

The element shape function matrix **S** can be expressed by using the nodal coordinates and the interpolating polynomial as follows:

$$\mathbf{S} = \left[S_1\mathbf{I} \quad S_2\mathbf{I} \quad S_3\mathbf{I} \quad S_4\mathbf{I} \quad S_5\mathbf{I} \quad S_6\mathbf{I} \right] . \tag{4.22}$$

In Equation (4.22), **I** is a 3 × 3 identity matrix and the element shape functions $S_1 \ldots S_6$ are

$$S_1 = 1 - \xi , \qquad S_2 = l(\eta - \xi\eta) , \qquad S_3 = l\zeta(1-\xi) ,$$

$$S_4 = \xi , \qquad S_5 = l\xi\eta , \qquad S_6 = l\xi\zeta ,$$

where the non-dimensional quantities ξ, η and ζ are defined as follows:

$$\xi = \frac{x}{l} , \qquad \eta = \frac{y}{l} , \qquad \zeta = \frac{z}{l} .$$

The shape functions contain both quadratic terms and terms that are products of one-dimensional linear polynomials.

In order to be able to model curved shapes in an efficient way, the element can be modified by adding an extra node in the middle of the element as introduced as a planar case in Reference [43] or the higher order element recently proposed by Dufva *et al.* [66] can be used. The element proposed by Dufva *et al.* is based on a similar theory with the two-dimensional shear deformable beam used for the two-dimensional belt-drive examples in Chapter 3. In the element, the position $\mathbf{r}_P$ of an arbitrary particle P can be defined as follows:

$$\mathbf{r}_P = \mathbf{r}_c + \mathbf{A}_\gamma^y \mathbf{A}_\psi^y \mathbf{v}^y + \mathbf{A}_\gamma^z \mathbf{A}_\psi^z \mathbf{v}^z \,. \tag{4.23}$$

In Equation (4.23), the vector $\mathbf{r}_c$ can be written as

$$\mathbf{r}_c = \left.\mathbf{Se}\right|_{y,\, z=0}, \tag{4.24}$$

where the vector **e** for the node I of the element is

$$\mathbf{e}_I = \begin{bmatrix} \mathbf{r}_I^T & \dfrac{\partial \mathbf{r}_I^T}{\partial x} & \dfrac{\partial \mathbf{r}_I^T}{\partial y} & \dfrac{\partial \mathbf{r}_I^T}{\partial z} \end{bmatrix}^T . \tag{4.25}$$

The transformation matrices $\mathbf{A}_\gamma^\alpha$ and $\mathbf{A}_\psi^\alpha$, where $\alpha = y, z$, are due to the rotation of the centerline and shear deformation in the y- and z-directions, respectively. Vectors $\mathbf{v}^y$ and $\mathbf{v}^z$ contained in the cross-section of the beam in the initial position can be written as:

$$\mathbf{v}^y = \begin{bmatrix} 0 & y & 0 \end{bmatrix}^T, \tag{4.26}$$

$$\mathbf{v}^z = \begin{bmatrix} 0 & 0 & z \end{bmatrix}^T, \tag{4.27}$$

where y and z are the local coordinates of the particle P in the cross-section of the beam. The orthogonal rotation matrices $\mathbf{A}_\psi^y$ and $\mathbf{A}_\psi^z$ created from the tangent frames can be expressed as follows:

$$\mathbf{A}_\psi^y = \begin{bmatrix} \mathbf{t}_\psi^y & \mathbf{n}_\psi^y & \mathbf{b}_\psi^y \end{bmatrix}, \tag{4.28}$$

$$\mathbf{A}_{\psi}^{z} = \begin{bmatrix} \mathbf{t}_{\psi}^{z} & \mathbf{n}_{\psi}^{z} & \mathbf{b}_{\psi}^{z} \end{bmatrix}. \tag{4.29}$$

In Equations (4.28…4.29) the vectors $\mathbf{t}_{\psi}^{\alpha}$, $\mathbf{n}_{\psi}^{\alpha}$ and $\mathbf{b}_{\psi}^{\alpha}$, where $\alpha = y, z$, can be written as:

$$\mathbf{t}_{\psi}^{y} = \frac{\mathbf{r}_{,x}}{\left\| \mathbf{r}_{,x} \right\|}, \qquad \mathbf{b}_{\psi}^{y} = \frac{\mathbf{t}_{\psi}^{y} \times \mathbf{r}_{,x}}{\left\| \mathbf{t}_{\psi}^{y} \times \mathbf{r}_{,x} \right\|}, \qquad \mathbf{n}_{\psi}^{y} = \mathbf{b}_{\psi}^{y} \times \mathbf{t}_{\psi}^{y},$$

$$\mathbf{t}_{\psi}^{z} = \mathbf{t}_{\psi}^{y}, \qquad \mathbf{n}_{\psi}^{z} = \frac{\mathbf{r}_{,x} \times \mathbf{t}_{\psi}^{z}}{\left\| \mathbf{r}_{,x} \times \mathbf{t}_{\psi}^{z} \right\|}, \qquad \mathbf{b}_{\psi}^{z} = \mathbf{t}_{\psi}^{z} \times \mathbf{n}_{\psi}^{z}.$$

Since the angles that characterizes the shear deformations are small, the rotation matrices $\mathbf{A}_{\gamma}^{y}$ and $\mathbf{A}_{\gamma}^{z}$ can be determined with the help of linearized Rodriquez formula as follows:

$$\mathbf{A}_{\gamma}^{y} = \begin{bmatrix} 1 & 0 & \sin\gamma^{y} \\ 0 & 1 & 0 \\ -\sin\gamma^{y} & 0 & 1 \end{bmatrix}, \tag{4.30}$$

$$\mathbf{A}_{\gamma}^{z} = \begin{bmatrix} 1 & -\sin\gamma^{z} & 0 \\ \sin\gamma^{z} & 1 & 0 \\ 0 & 0 & 1 \end{bmatrix}. \tag{4.31}$$

The components of the shear angles shown in Figure 4.7 are simply interpolated over the element as follows:

$$\sin\gamma^{y} \approx (\sin\gamma^{y})^{I}(1 - \frac{x}{l}) + (\sin\gamma^{y})^{J}\frac{x}{l}, \tag{4.32}$$

$$\sin\gamma^{z} \approx (\sin\gamma^{z})^{I}(1 - \frac{x}{l}) + (\sin\gamma^{z})^{J}\frac{x}{l}. \tag{4.33}$$

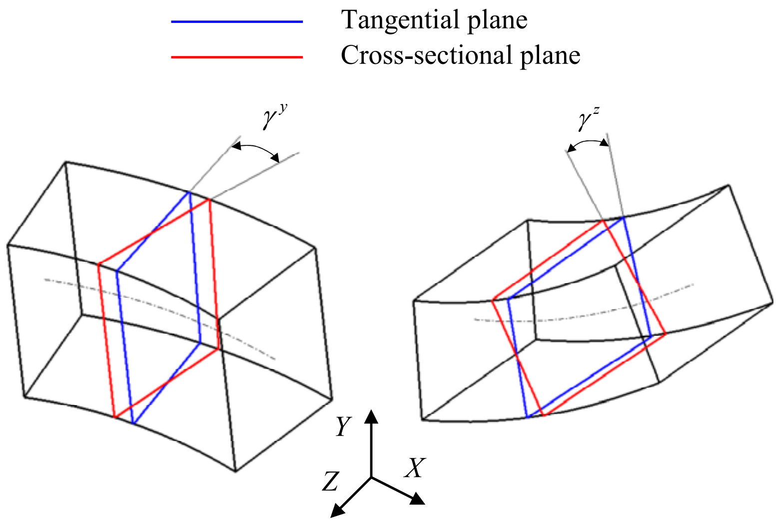

Figure 4.7 The shear angles of the element.

The strain energy is expressed with the components of the strain tensor as follows:

$$U = \frac{1}{2}\int_V \left[\left(E(\varepsilon_{xx}^2 + \varepsilon_{yy}^2 + \varepsilon_{zz}^2) + 4G(k_s\varepsilon_{xy}^2 + k_s\varepsilon_{xz}^2 + \varepsilon_{yz}^2\right)\right] dV\,. \tag{4.34}$$

Initially the beam is assumed to be coincident with the global coordinate system and not curved. The strain components ε_{xx}^m and ε_{xy}^m are calculated using Equations (3.13) and (3.14). Accordingly, the strain component ε_{xz}^m can be written in the following form:

$$\varepsilon_{xz}^m = \frac{1}{2}\left[\frac{\partial \mathbf{r}^T}{\partial x}\frac{\partial \mathbf{r}}{\partial z} - 1\right]. \tag{4.35}$$

The rest of the strain components of Equation (4.34) are approximated using linear interpolation [54]. For example, the strain component ε_{yy}^m can be defined as follows:

$$\varepsilon_{yy}^m = \left(1 - \frac{x}{l}\right)\left\|\frac{\partial \mathbf{r}^I}{\partial y}\right\| + \frac{x}{l}\left\|\frac{\partial \mathbf{r}^J}{\partial y}\right\| - 1\,. \tag{4.36}$$

The strain components achieved using Green-Lagrange measures are modified in order to obtain a belt-like element with reduced bending stiffness around the *y*- and *z*-axis by adding coefficients α_1 and α_2 to determine the magnitude of each term of the strain energy similarly to the procedure introduced in Chapter 3. According to Figure 4.8, the following definition for the position vector **r** can be used:

$$\mathbf{r} = \mathbf{r}_c + y\mathbf{r}_s^y + z\mathbf{r}_s^z \,, \tag{4.37}$$

where

$$\mathbf{r}_s^y = \mathbf{A}_\gamma^y \mathbf{A}_\psi^y \begin{bmatrix} 0 \\ 1 \\ 0 \end{bmatrix}, \tag{4.38}$$

$$\mathbf{r}_s^z = \mathbf{A}_\gamma^z \mathbf{A}_\psi^z \begin{bmatrix} 0 \\ 0 \\ 1 \end{bmatrix}. \tag{4.39}$$

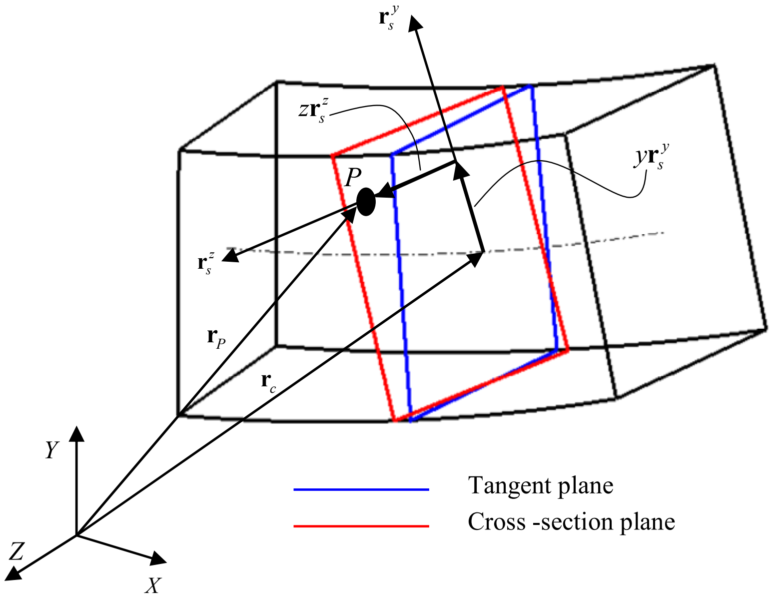

Figure 4.8 Description of the position of an arbitrary particle *P* on the cross-section of the element.

The terms of Equation (4.34) which are related to the strain components ε_{xx}^{m}, ε_{xy}^{m} and ε_{xz}^{m} can be rewritten as follows:

$$
\begin{aligned}
\frac{1}{2}\int_V E{\varepsilon_{xx}^{m}}^2 dV = \frac{E}{2}\int_V \Bigg[& \frac{\alpha_1}{4}\left(\left(\mathbf{r}_{c,x}^{T}+\mathbf{r}_{c,x}^{zT}\right)\left(\mathbf{r}_{c,x}+\frac{\alpha_2}{\alpha_1}\mathbf{r}_{c,x}^{z}z\right)-1\right)^2 + \\
& +\frac{\alpha_2}{4}\Big(\Big(\left(\left(\mathbf{r}_{c,x}^{T}+\mathbf{r}_{s,x}^{zT}z\right)\left(\mathbf{r}_{c,x}+\mathbf{r}_{s,x}^{z}z\right)-1\right)\mathbf{r}_{s,x}^{yT}\mathbf{r}_{s,x}^{y} + \\
& +\left(\mathbf{r}_{c,x}^{T}+\mathbf{r}_{s,x}^{zT}z\right)\mathbf{r}_{s,x}^{y}+\mathbf{r}_{s,x}^{yT}\left(\mathbf{r}_{c,x}+\mathbf{r}_{s,x}^{z}z\right)\Big)\Big)^2 y^2 \\
& +\frac{\alpha_2}{4}\left(\mathbf{r}_{s,x}^{yT}\mathbf{r}_{s,x}^{y}\right)^2 y^4\Bigg]dV
\end{aligned}, \qquad (4.40)
$$

$$
\frac{1}{2}\int_V 4k_s G{\varepsilon_{xy}^{m}}^2 dV = 2k_s G\int_V\left[\frac{\alpha_2}{4}\left(\left(\mathbf{r}_{c,x}^{T}+\mathbf{r}_{s,x}^{zT}z\right)^2 {\mathbf{r}_{s}^{y}}^2 + {\mathbf{r}_{s,x}^{yT}}^2{\mathbf{r}_{s}^{y}}^2 y^2\right)\right]dV\,, \qquad (4.41)
$$

$$
\frac{1}{2}\int_V 4k_s G{\varepsilon_{xz}^{m}}^2 dV = 2k_s G\int_V\left[\frac{\alpha_2}{4}\left(\left(\mathbf{r}_{c,x}^{T}+\mathbf{r}_{s,x}^{zT}z\right)^2 {\mathbf{r}_{s}^{z}}^2 + {\mathbf{r}_{s,x}^{yT}}^2{\mathbf{r}_{s}^{z}}^2 y^2\right)\right]dV\,. \qquad (4.42)
$$

It is essential to note that the beam element can be used to analyze V-belts since the three-dimensional element can take surface forces into account. It is also noteworthy that the beam element can describe the deformation of a cross-section [41]. The implementation of these elements to the models of belt-drives is not carried out in this work and should be done in the future.

4.5 Modeling of the Frictional Contact

The frictional contact force between the belt and the pulley surface used in this section is based on the model proposed by Wasfy and Leamy [1, 25] and the generalization of the use for higher order elements based on the absolute nodal coordinate formulation with the distributed frictional forces used to derive the equivalent nodal forces [31]. The penetration at the point of contact between the belt and the pulley is used in the formulation of the normal forces which are included in the dynamic formulation by the penalty method.

The penetration d and the time rate $\dot{d}$ of penetration are defined in the direction of the surface normal **n**. The penetration at a contact point can be determined as follows:

$$d = R_p - \|\mathbf{N}\|, \tag{4.43}$$

where **N** defines the position of an arbitrary particle on the element and R_p is the radius of the pulley. In a general three-dimensional case, the normal vector **N** can be defined as illustrated in Figure 4.9:

$$\mathbf{N} = \mathbf{r}_n - \left(\mathbf{r}_n^T \mathbf{p}\right)\mathbf{p}. \tag{4.44}$$

In Equation (4.44) $\mathbf{r}_n = \mathbf{r} - \mathbf{r}_p$, $\mathbf{r}$ is a global position vector of a particle on the element, $\mathbf{r}_p$ the global position vector of the pulley center and **p** a unit vector along the pulley axis.

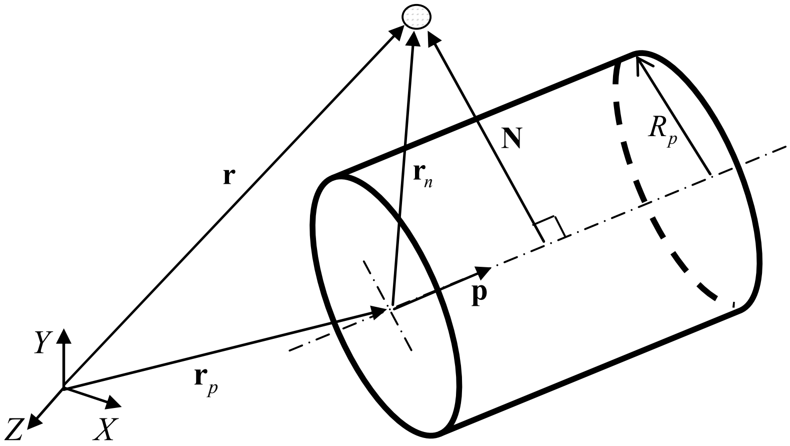

Figure 4.9 Definition of the contact point [61].

The virtual work of the contact forces in the case of a plate element with the length l and the width w can be written as [31]:

$$\partial W = \int_0^w \int_0^l \partial \mathbf{r}^T \left(\mathbf{f}_n + \mathbf{f}_t \right) dxdy = \partial \mathbf{e}^T \int_0^w \int_0^l \mathbf{S}^T \left(\mathbf{f}_n + \mathbf{f}_t \right) dxdy = \partial \mathbf{e}^T \mathbf{Q}_c \,. \tag{4.45}$$

Generally contact conditions, velocities and forces are different from one particle to another on the element and therefore it is essential to determine the contact forces at different locations. In the numerical implementation, the contact forces can be calculated using Gauss integration points [31] or other discrete points [61].

4.6 Numerical Examples of the Three-Dimensional Belt-Drive

The three-dimensional belt-drive used in the numerical examples consists of two pulleys and a flexible belt as shown in Figure 4.1. In order to produce the initial stress in the belt, the undeformed configuration is used as the reference configuration for the evaluation of the elastic forces of the element. As can be seen in Table 4.1 shown in Section 4.1, differences between the two models used, Model 1 and Model 2, are related to the values of the parameters, while the structures are identical.

The geometrical and material parameters of Model 2 are approximated from the data presented in Reference [5], where the analytical formulation with assumptions of planar configuration and a steady state condition is studied. The number of discrete points used to evaluate the contact forces is 81 in every following example. In the numerical examples presented in this section, the angular velocity of the driving pulley is determined according to Equation (3.29) with varying values for nominal angular velocity of the driving pulley and time. Since the tension of the belt has an essential role on the contact forces between the belt and pulleys, it is important to achieve sufficient initial tension. In Model I, the belt tension is controlled at the beginning of the simulation by defining the displacement of the driver pulley in the x -direction using the following function:

$$u = \begin{cases} \dfrac{u_0}{t_0} t, & t < t_0 \\ u_0, & t > t_0 \end{cases}, \tag{4.46}$$

where u_0 is the steady state displacement of the driver pulley.

In the first example, Model 1, Young's modulus is $1.0 \cdot 10^7$ N/m^2 and the initial displacement u_0 of the driver pulley is 0.0025 m. The solution for the angular velocity of the driven pulley obtained using 16 plate elements (288 degrees of freedom) is shown in Figure 4.10. The low value of Young's modulus can be seen as a noticeable difference between the angular velocities of the driver and driven pulleys due to the slipping during the acceleration period. This result agrees well with the results reported in the section of the two-dimensional belt-drive, where the connections between the velocities of the driver and driven pulleys, Young's modulus and the coefficient v_s were presented.

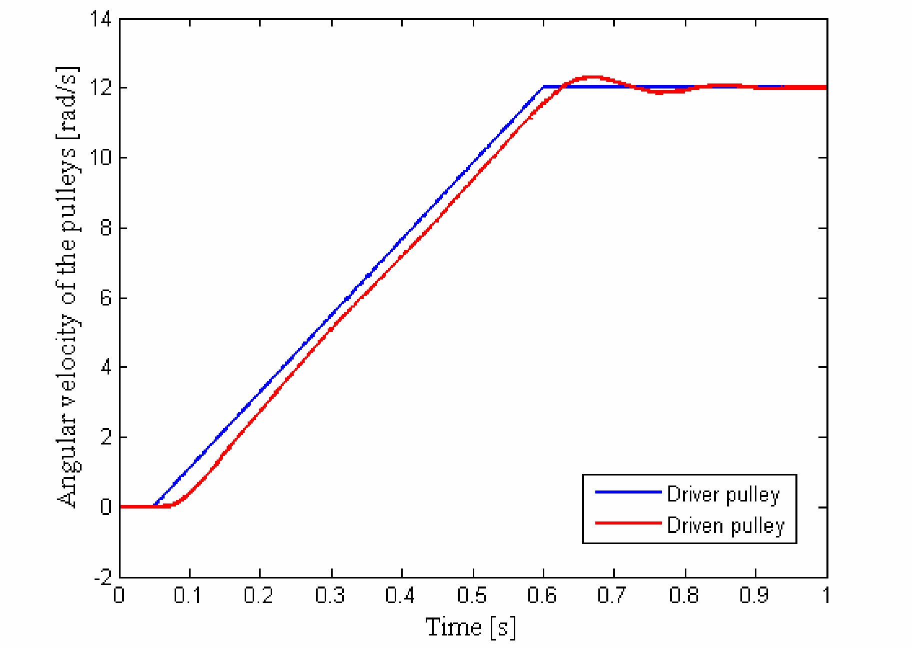

Figure 4.10 Angular velocity of the driven pulley using 16 plate elements [61].

In order to study the dynamics of the high-speed belt-drive, the parameters of Model 2 are used with Young's modulus of $1.6667 \cdot 10^6\ \text{N/m}^2$. The effect of the bending deformation is neglected in this example due to the thinness of the belt. In addition, the initial tension, i.e. the axial force, of the belt is obtained by using a belt length shorter than the length required by the drive geometry instead of moving the driven pulley. According to Reference [5], the initial axial force in the belt is 50 N. The opposite torque T_a is applied to the driven pulley using the following trigonometric expression:

$$T_a = \begin{cases} 0, & \text{if} \quad t \le 0.05 \\ 1 - \cos\dfrac{\pi t}{1.0}, & \text{if} \quad 0.05 < t \le 1.0\ . \\ 2, & \text{if} \quad 0.6 < t \end{cases} \tag{4.47}$$

The analytical belt tension according to Reference [5] is illustrated in Figure 4.11, while Figure 4.12 shows the belt tension obtained using 20 plate elements (360 degrees of freedom) with three different strain descriptions. The analytical result and the finite element prediction of the belt speed distribution are displayed correspondingly in Figures 4.14 and 4.15. Strain and speed distributions are computed along the belt edge ($y = 0$) using 20 points on each element of the belt.

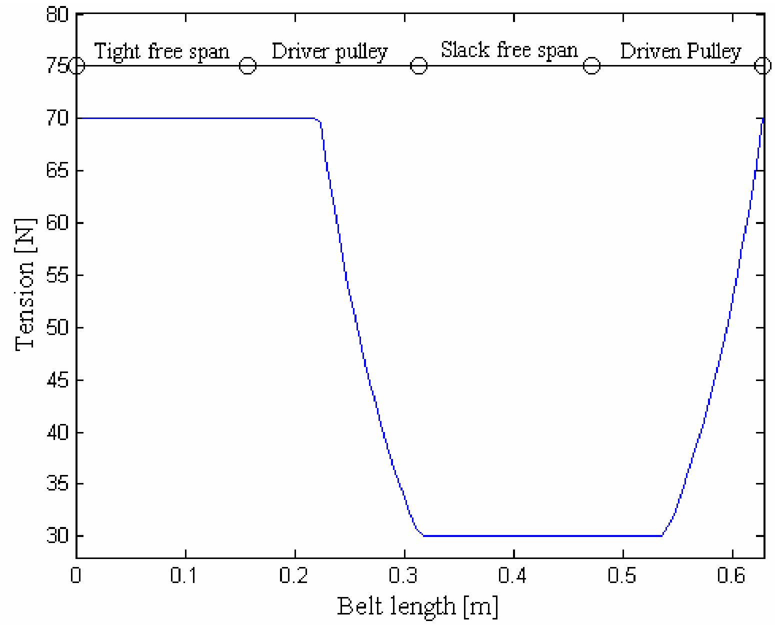

Figure 4.11 Analytical distribution of tension for a compliant belt ($k = 0.2$ kN), Model 2 [5].

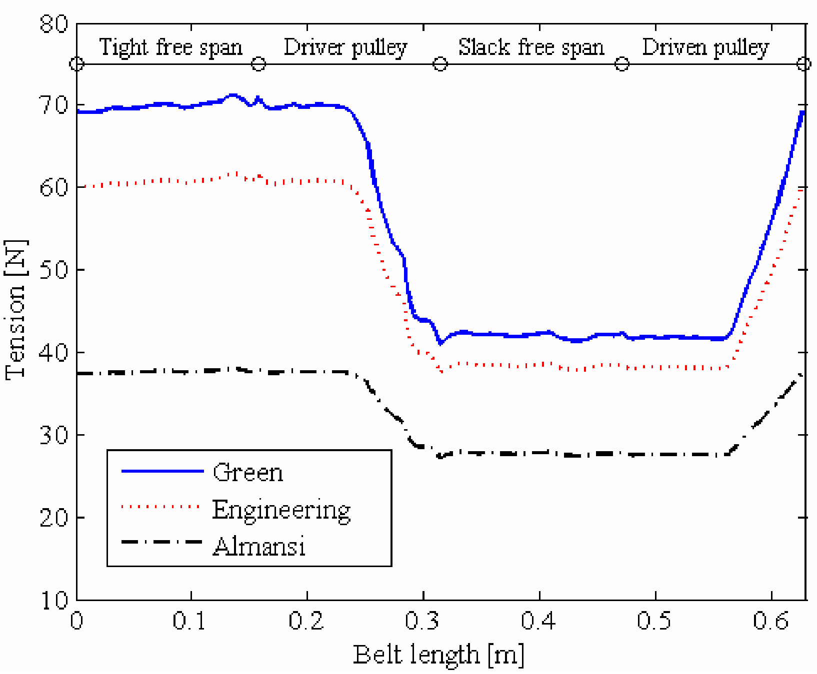

Figure 4.12 Tension on the belt for a compliant belt (k = 0.2 kN) using different strain definitions, Model 2 [61].

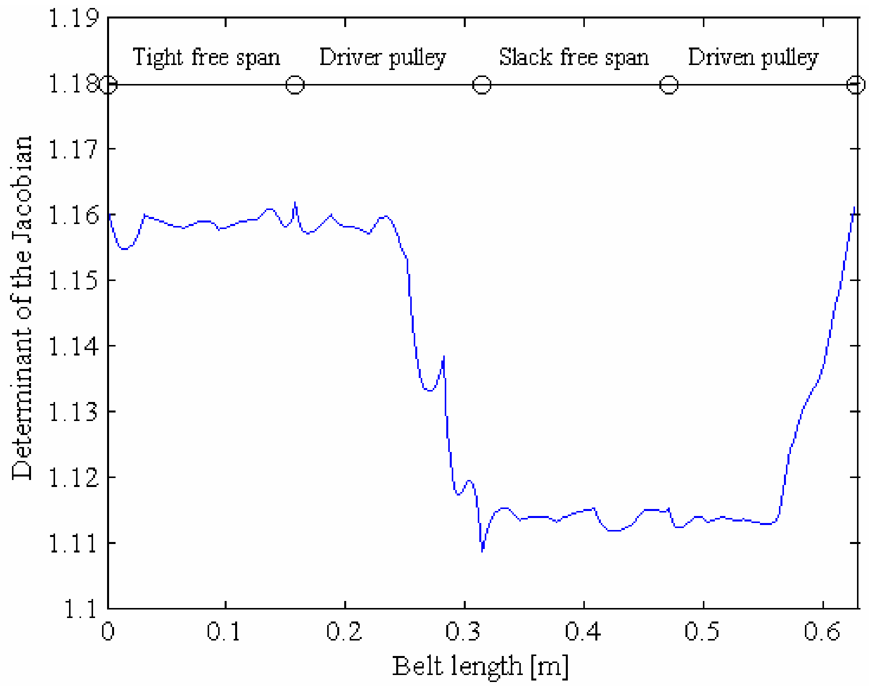

Figure 4.13 Determinant of the Jacobian, Model 2 [61].

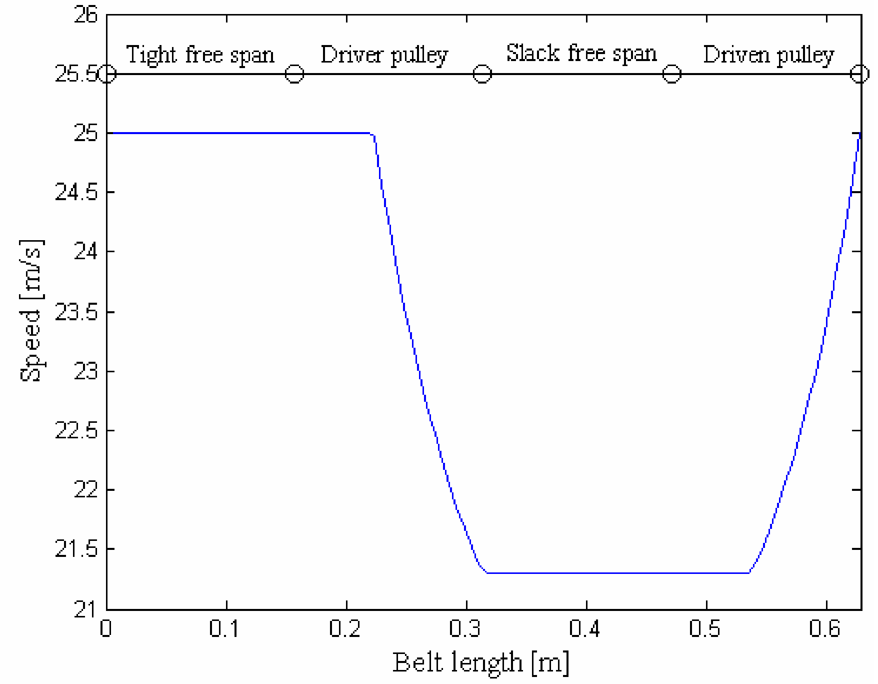

Figure 4.14 Analytical distribution of belt speed for a compliant belt (*k* = 0.2 kN), Model 2 [5].

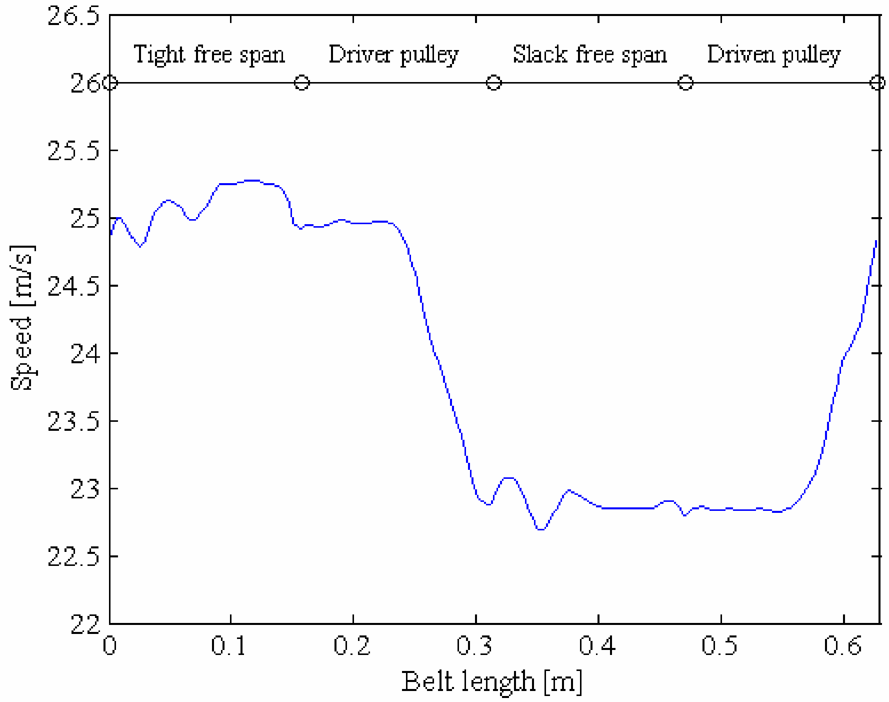

Figure 4.15 Belt speed distribution of the belt-drive model for a compliant belt (*k* = 0.2 kN), Model 2 [61].

Figures 4.11…4.15 illustrate that the belt-drive model predicts higher values of the tension and speed of the belt for the slack free span region, but otherwise the results agree satisfyingly. The different assumptions in the analytical and numerical models can be seen as the main source for the differences in the results. As usual, the behavior of the belt-drive model is not as stable as predicted by the analytical model; some oscillation can be perceived in the results of Figures 4.12 and 4.15. The remarkable differences between the three strain definitions used can be explained by the large deformations in the belt. It is commonly known that the strain measures may lead to significant differences in cases of large deformation. The determinant of the Jacobian, shown in Figure 4.13, illustrates the magnitude of the deformation along the belt length. The more the value of the determinant differs from 1, the more deformation and larger differences between different strain measures exist. It can also be noted, that the tensions provided by the different strain measures do not satisfy the torque equilibrium of the driven pulley with the applied opposing torque of 2 Nm. The Green strain measure provides only the torque of 1.4 Nm while the other measures predict even smaller values of the torque. Due to the constant velocity of the driven pulley during the steady state, it can be concluded that the contact model used produce higher torque on the driven pulley than depicted by the tension distributions of the belt.

The results presented in Figure 4.16 show clearly that the belt is not able to transmit the moment required by the opposing torque without considerable slipping between the belt and driven pulley. The angular velocity of the driven pulley in the steady state is approximately 10 % lower in comparison to the corresponding value of the driver pulley. In Reference [5] it is assumed that the belt attaching the driver or driven pulley does not slip and therefore the angular velocity of the pulleys are determined as follows:

$$\omega_{driver} = \frac{v_{tight}}{R}, \quad \omega_{driven} = \frac{v_{slack}}{R} \quad . \tag{4.48}$$

In Equation (4.48) v_{tight} and v_{slack} are the speeds of tight and slack free spans, respectively. According to Figure 4.14 and Equation (4.48), the angular velocity of the driven pulley in the steady state condition can be found to be approximately 14.6 % lower than the angular velocity of the driver pulley. Therefore, the analytical model predicts even more slipping on the driven pulley than the numerical belt-drive model.

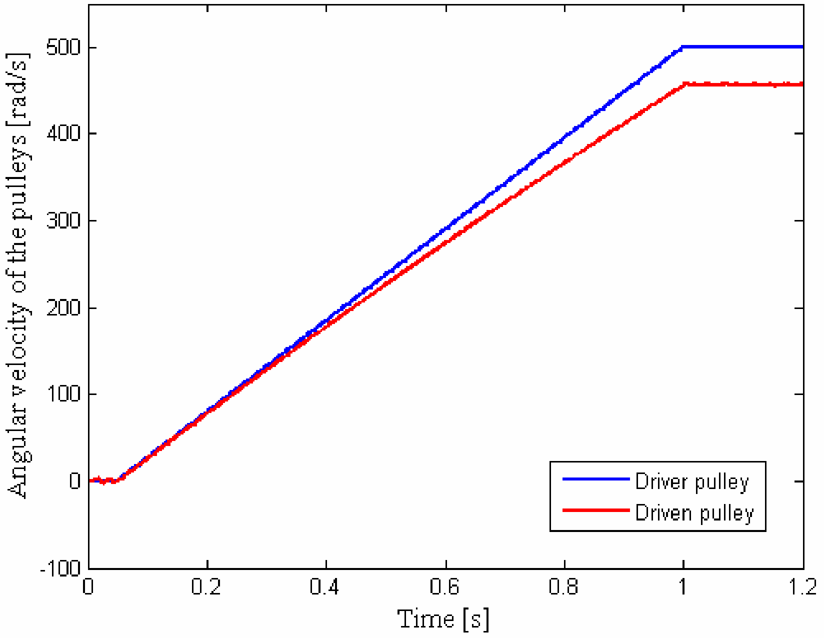

Figure 4.16 Angular velocity of the pulleys of the belt-drive model, Model 2 [61].

The distributions of the friction and normal contact forces over the belt length of the belt-drive using two different analytical models and the plate element formulation are illustrated in Figures 4.17…4.18. The difference between the analytical full and capstan models is that in the analytical capstan model the inertia contributions in the momentum equations are neglected. The force distributions are computed along the centreline of the element (y = 0.02 m). As can be seen, there exist some oscillation of the friction force provided by the numerical model, and the force distributions of the numerical model agree more accurately with the analytical capstan model than the analytical full model. It is important to note, that when the friction force is integrated over the active contact area of the driven pulley and multiplied by the radius of the pulley, the moment corresponding to the applied opposing torque is achieved. The overshoots of the normal force distribution of the numerical model are due to negative damping forces and do not have an impressive effect to the global response as explained in Reference [5].

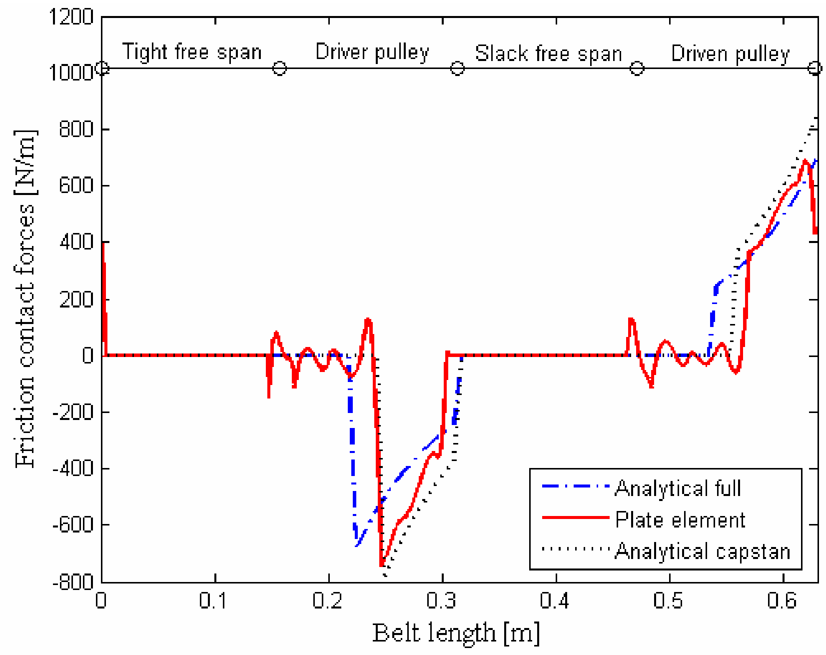

Figure 4.17 Friction force distributions for the analytical and numerical models for a compliant belt ($k = 0.2$ kN), Model 2 [5], [61].

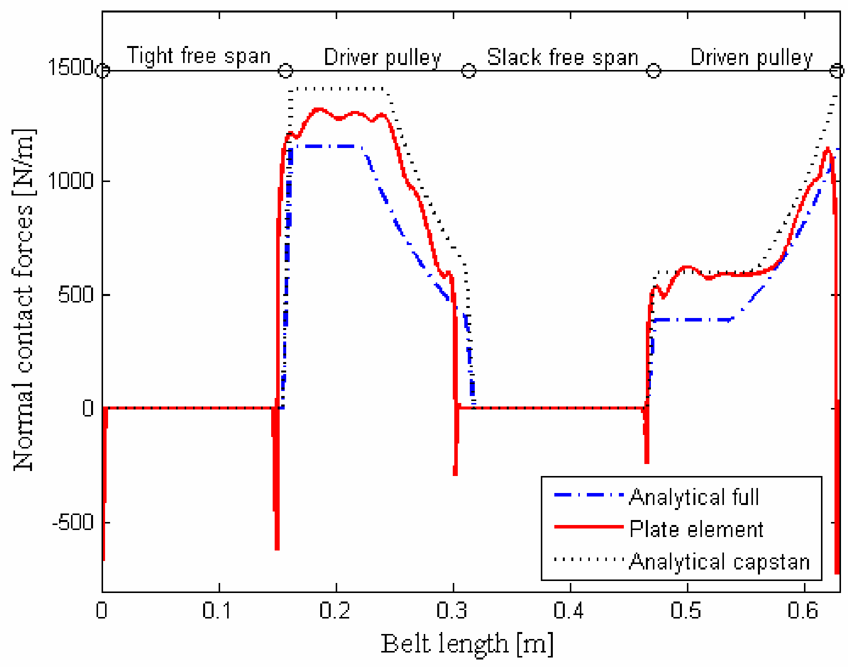

Figure 4.18 Normal force distributions for the analytical and numerical models for a compliant belt ($k = 0.2$ kN), Model 2 [5], [61].

Based on the results presented in this section, it can be concluded that by using the thin plate element based on the absolute nodal coordinate formulation, belt-drives can be modeled with a significantly low number of elements. In the future, the belt-drive with stiffer belt modeled using the plate elements would be worth of studying in order to find out the effect of the strain magnitude to the results, especially to tension distributions. However, with the advanced features of the absolute nodal coordinate formulation, the models of the belt-drives become more efficient in comparison to the models with traditional finite elements and also with the plate elements based on the general absolute nodal coordinate formulation that employ full parameterization.

5 CONCLUSIONS

The first objective of this study was to develop a computationally efficient two-dimensional shear deformable beam element based on the absolute nodal coordinate formulation. It was perceived that although the displacement field of the previously proposed beam element based on the absolute nodal coordinate formulation includes a cubic interpolation polynomial in the axial direction of the displacement, the element exhibits linear bending behavior, i.e. a constant bending moment distribution along the longitudinal coordinate. Therefore, the advantage of the third-order polynomial expansion is debatable. The proposed beam element uses a linear displacement field neglecting higher-order terms and a reduced number of nodal coordinates, which leads to fewer degrees of freedom in a finite element. In the proposed element, the expression of the elastic forces is nonlinear. The accompanying defects of the phenomenon known as shear locking were avoided through the adoption of selective integration within the numerical integration method. For the proposed element, integration in closed form was used to evaluate the contribution of normal and shear strains over the cross-section of the element while the numerical integration method with one Gauss point was used to evaluate the contribution of strains in the axial direction. By using this combination, the element locking was eliminated and an accurate and fast convergence was achieved. In addition, the use of complicated cross-sections of the elements was not restricted.

Several numerical examples, including both static and dynamic tests, were used to demonstrate the functionality and usability of the proposed beam model. The results were compared to the results of a commercial finite element code ANSYS, the results of the previously published beam element model by Omar and Shabana and analytical results. Generally, the results in the cases of linear and non-linear deformations were in good agreement. On the other hand, it is clear that neither the proposed elements nor the element of Omar and Shabana achieve good results with one element. However, the use of elements as simple as possible is popular due to their straightforward implementation and computational efficiency. For non-linear deformations, the discrepancies between the different models increased when the height of the beam simultaneously with the role of shear strain was increased. In the studied cases, the computing times of the iterations were two times faster using the proposed elements than using the elements of Omar and Shabana.

In the case of a simple pendulum, the results of the proposed beam element demonstrated good functionality. The energy balance of the dynamic model remained exactly constant, and the results were in good agreement with the beam model of Omar and Shabana with less computational effort. The results of the spinning beam showed that realistic modeling of large rigid body motion and a capability of automatic accounting of the centrifugal stiffening effect of a spinning beam were reached by using the proposed elements. For these reasons, the proposed beam element is potential and provides groundwork for future development of the absolute nodal coordinate formulation.

The second objective of this study was to find out the applicability of the absolute nodal coordinate formulation to model the simple belt-drive system as two- and three-dimensional cases. The general requirements for the successful and efficient analysis of the belt-drive system are the exact modeling of the rigid body inertia during an arbitrary rigid body motion, the consideration of the effect of the shear deformation, the exact description of the highly nonlinear deformations and a simple and realistic description of the contact. All these requirements were fulfilled by utilizing a recently proposed two-dimensional shear deformable beam element [54]. Based on this element, a belt-like element was developed in this study. The new element allows the user to control the axial and bending stiffness through the use of two parameters. Thus the new element is capable of presenting a very high stiffness in axial solicitation as well as of opposing a small resistance to bending, just as a piece of a typical belt. The formulations of two three-dimensional shear deformable beam elements, which could be applied to the modeling of V-belts, were also presented.

The use of a thin plate element based on the absolute nodal coordinate formulation in the nonlinear dynamic analysis of belt-drives was also studied in this work. This reduced order element has a constant mass matrix and is able to describe an arbitrary rigid body displacement. Therefore it can be used with a non-incremental solution procedure and can be implemented in general purpose flexible multi-body algorithms. The effect of bending can be included or excluded and the element provides additional degrees of freedom that can be important in the future in the study of three-dimensional dynamics phenomena that result, for example, from the rotation of the belt about its longitudinal axis. The plate formulation also allows using a surface distribution of the contact forces which can not be obtained using beam elements since these elements are represented by their centerline.

The implementation in flexible multi-body algorithms is crucial, particularly when more general belt- drive configurations and loading conditions are considered. The equations of motion of the belt-drive were developed using the Lagrangian formulation. The contact between the belt and the pulleys was modeled using an elastic approach which is based on a tri-linear Coulomb-like friction model previously proposed in the literature. This procedure uses the penetration of the belt inside the pulley to calculate the normal and friction forces involved in contact. Therefore, no constraint equations need to be added to the equations of motion of the system. Due to the use of high order elements, the contact forces can be distributed along the length of the beam and along the surface of the plate element instead of concentrating them at the nodes as it has been done in the literature [1, 23, 25]. With this contribution to the contact model there was no need to use a high number of nodes for the realistic representation of the boundary of the pulley.

Several numerical examples, including both static and dynamic tests, were used to demonstrate the functionality and usability of the absolute nodal coordinate formulation in the modeling of the belt-drive system. The numerical results showed that by using the distributed contact forces and high order elements based on the absolute nodal coordinate formulation, the realistic behavior of the belt-drives can be obtained with a significantly smaller number of elements and degrees of freedom in comparison to the previously published finite element models of belt-drives. The results of the examples demonstrated a good functionality and suitability of the absolute nodal coordinate formulation for the computationally efficient and realistic modeling of belt-drives.

It is interesting to notice the analogy between the belt-drives and calendaring in the paper making process. There are many critical and challenging applications in paper and metal industry, where the passage of an elastic strip or sheet of material through the nip between different kinds of rollers is included. The theory and methods used in modeling the belt-drives are potentially utilizable and worth extending to the modeling of calendering in the paper making process. It is clear that further studies of more complex belt-drive applications require also investing energy in the development of numerical procedures, especially in the area of numerical integration methods, and extensive and careful verifications of the responses from the numerical and analytical models with measurements from suitable prototypes. In addition, more realistic friction descriptions and the models of composite materials are the essential areas of the research in the future.

REFERENCES

[1] Leamy, M. J., and Wasfy, T. M., 2002, “Transient and Steady-State Dynamic Finite Element Modeling of Belt-Drives”, *Journal of Dynamic Systems, Measurement and Control*, **124**, pp. 575-581.

[2] Alciatore, D. G., and Traver, A. E., 1995, “Multipulley Belt Drive Mechanics: Creep Theory vs Shear Theory”, *Journal of Mechanical Design*, **117**, pp. 506-511.

[3] Fawcett, J. N., 1981, “Chain and Belt Drives- A Review”, *Shock and Vibration Digest*, **13**, pp. 5-12.

[4] Johnson, K. L., 1985, *Contact Mechanics*, Cambridge University Press, Cambridge.

[5] Bechtel, S. E., Vohra, S., Jacob, K. I., and Carlson, C. D., 2000, “The Stretching and Slipping of Belts and Fibers on Pulleys”, *Journal of Applied Mechanics*, **67**, pp. 197-206.

[6] Gerbert, G. G., 1996, “Belt Slip- A Unified Approach”, *Journal of Mechanical Design*, **118**, pp. 432-438.

[7] Townsend, W. T., and Salisbury, J. K., 1988, “The Efficiency Limit of Belt and Cable Drives”, *Journal of Mechanisms, Transmissions and Automation in Design*, **110**, pp. 303-307.

[8] Kim, H., and Marshek, K. M., 1987, “The Effect of Belt Velocity on Flat Belt Drive Behavior”, *Mechanism and Machine Theory*, **22**, pp. 523-527.

[9] Kim, H., and Marshek, K. M., 1990, “Force Distribution for a Flat Belt Drive with a Concentrated Contact Load”, *Mechanism and Machine Theory*, **25**, pp. 667-677.

[10] Kim, H., Ahn, H., and Marshek, K. M., 1991, “Friction Characteristics for Concentrated Load Area on a Flat Belt Drive”, *Mechanism and Machine Theory*, **26**, pp. 351-358.

[11] Hwang, S. J., Perkins, N. C., Ulsoy, A. G., and Mecstroth, R. J., 1994, “Rotational Response and Slip Prediction of Serpentine Belt Drive Systems”, *Journal of Vibration and Acoustics*, **116**, pp. 71-78.

[12] Beikmann, R. S, Perkins, N. C., and Ulsoy, A. G., 1996, ”Free Vibration of Serpentine Belt Drive Systems”, *Journal of Vibration and Acoustics*, **118**, pp. 406-413.

[13] Beikmann, R. S, Perkins, N. C., and Ulsoy, A. G., 1996, ”Nonlinear Coupled Vibration Response of Serpentine Belt Drive Systems”, *Journal of Vibration and Acoustics*, **118**, pp. 567-574.

[14] Beikmann, R. S, Perkins, N. C., and Ulsoy, A. G., 1997, ”Design and Analysis of Automotive Serpentine Belt Drive Systems for Steady State Performance”, *Journal of Mechanical Design*, **119**, pp. 162-168.

[15] Leamy, M. J., and Perkins, N. C., 1998, “Nonlinear Periodic Response of Engine Accessory Drives with Dry Friction Tensioners”, *Journal of Vibration and Acoustics*, **120**, pp. 909-916.

[16] Kraver, T. C., Fan, G. W., and Shah, J. J., 1996, “Complex Modal Analysis of a Flat Belt Pulley System with Belt Damping and Coulomb-Damped Tensioner”, *Journal of Mechanical Design*, **118**, pp. 306-311.

[17] Kong, L., and Parker, R. G., 2003, “Equilibrium and Belt-Pulley Vibration Coupling in Serpentine Belt Drives”, *Journal of Applied Mechanics*, **70**, pp. 739-750.

[18] Kong, L., and Parker, R. G., 2004, “Coupled Belt-Pulley Vibration in Serpentine Belt Drives With Belt Bending Stiffness”, *Journal of Applied Mechanics*, **71**, pp. 109-119.

[19] Kong, L., and Parker, R. G., 2005, “Steady Mechanics of Belt-Pulley Systems”, *Journal of Applied Mechanics*, **72**, pp. 25-34.

[20] Leamy, M. J., Barber, J. R., and Perkins, N. C., 1998, “Distortion of a Harmonic Elastic Wave Reflected from a Dry Friction Support”, *Journal of Applied Mechanics*, **65**, pp. 851-857.

[21] Leamy, M. J., Barber, J. R., and Perkins, N. C., 1998, “Dynamics of Belt/Pulley Frictional Contact”, *Proceedings of IUTAM Symposium on Unilateral Multibody Contacts*, Munich, August, Kluwer academic Press, pp. 277-286.

[22] Leamy, M. J., 1998, *The Influence of Dry Friction in the Dynamic Response of Accessory Belt Drive Systems*, Doctoral Dissertation, University of Michigan.

[23] Leamy, M. J., and Wasfy, T. M., 2002, “Analysis of Belt-Drive Mechanics Using a Creep-Rate-Dependent Friction Law”, *Journal of Applied Mechanics*, **69**, pp. 763-771.

[24] Wasfy, T. M., 1996, “A Torsional Spring-Like Beam Element for the Dynamic Analysis of Flexible Multibody Systems”, *International Journal for Numerical Methods in Engineering*, **39**, pp. 1079-1096.

[25] Wasfy, T. M., and Leamy, M. J., 2002, “Effect of Bending Stiffness on the Dynamic and Stead-State Responses of Belt-Drives”, *ASME 2002 Design Engineering Technical Conferences,* Montreal, Canada, September 29-October 2.

[26] Chen, W.-H., and Shieh, C.-J., 2003, “On Angular Speed Loss of Flat Belt Transmission System by Finite Element Method”, *International Journal of Computational Engineering Science*, **4**, pp. 1-18.

[27] Shieh, C.-J., and Chen, W.-H., 2001, “Three-Dimensional Finite Element Analysis of Frictional Contact for Belt Transmission Systems”, *The Chinese Journal of Mechanics*, **17**, pp. 189-199.

[28] Yu, D., Childs, T. H. C., and Dalgarno, K. W., 1998, “Experimental and Finite Element Studies of the Running of V-Ribbed Belts in Pulley Grooves”, *Proceedings of the Institution of Mechanical Engineers*, *Journal of Mechanical Engineering Science*, **212** (C), pp.343-354.

[29] Wilson, E. L., Taylor, R. L., Doherty, W. P., and Ghaboussi, J., 1973, “Incompatible Displacement Modes”, *Numerical and Computer Methods in Structural Mechanics*, pp. 43-57.

[30] Shieh, C.-J., and Chen, W.-H., 2002, “Effect of Angular Speed on Behavior of a V-Belt Drive System”, *International Journal of Mechanical Sciences*, **44**, pp. 1879-1892.

[31] Kerkkänen, K. S., García-Vallejo, D., and Mikkola, A. M., 2006, ”Modeling of Belt-Drives Using a Large Deformation Finite Element Formulation”, *Nonlinear Dynamics*, **43**, pp. 239-256.

[32] Shabana, A. A., 1998, *Dynamics of Multibody Systems*, Cambridge University Press, Cambridge.

[33] Shabana, A. A., 1998, “Computer Implementation of the Absolute Nodal Coordinate Formulation for Flexible Multibody Dynamics”, *Nonlinear Dynamics*, **16**, pp. 293-306.

[34] Escalona, J. L., Hussien H. A., and Shabana A. A., 1998, “Application of the Absolute Nodal Coordinate Formulation to Multibody System Dynamics”, *Journal of Sound and Vibration*, **214**(5), pp. 833-851.

[35] Cardona, A., and Geradin, M., 1988, “A Beam Finite Element Non-Linear Theory with Finite Rotations”, *International Journal for Numerical Methods in Engineering,* **26**, pp. 2403-2438.

[36] Omar, M. A., and Shabana, A. A., 2001, “A Two-Dimensional Shear Deformation Beam for Large Rotation and Deformation”, *Journal of Sound and Vibration*, **243**, pp. 565-576.

[37] Shabana, A. A., and Yakoub, R. Y., 2001, “Three Dimensional Absolute Nodal Coordinate Formulation for Beam Elements: Theory”, *ASME Journal of Mechanical Design*, **123**, pp. 606-613.

[38] Yakoub, R. Y., and Shabana, A. A., 2001, “Three Dimensional Absolute Nodal Coordinate Formulation for Beam Elements: Implementation and Applications”, *ASME Journal of Mechanical Design*, **123**, pp. 614-621.

[39] Mikkola, A. M., and Shabana, A. A., 2003, ”A Non-Incremental Finite Element Procedure for the Analysis of Large Deformation of Plates and Shells in Mechanical System Applications”, *Multibody System Dynamics*, **9**, pp. 283-309.

[40] Berzeri, M., and Shabana, A. A., 2000, “Development of Simple Models for the Elastic Forces of the Absolute Nodal Coordinate Formulation”, *Journal of Sound and Vibration*, **235**, pp. 539-565.

[41] Sopanen, J. T., and Mikkola, A. M., 2003, ”Description of Elastic Forces in Absolute Nodal Coordinate Formulation”, *Nonlinear Dynamics*, **34**, pp. 53-74.

[42] Campanelli, M., Berzeri, M., and Shabana, A. A., 2000, “Performance of the Incremental and Non-Incremental Finite Element Formulations in Flexible Multibody Problems”, *Journal of Mechanical Design*, **122**, pp. 498-507.

[43] García-Vallejo, D., Mikkola, A. M., and Escalona, J. L., 2006, *A Study on Locking Phenomenon in Shear Deformable Elements Based on the Absolute Nodal Coordinate Formulation*, Research report 62, Department of Mechanical Engineering, Lappeenranta University of Technology.

[44] Kerkkänen, K. S., Sopanen, J. T., and Mikkola, A. M., 2005, "A Linear Beam Finite Element Based on the Absolute Nodal Coordinate Formulation", *Journal of Mechanical Design*, **127**, pp. 621-630.

[45] Hughes, T. J. R., 2000, *The Finite Element Method: Linear Static and Dynamic Finite Element Analysis*, General Publishing Company, Ontario.

[46] Rhim, J., and Lee, S. W., 1998, "A Vectorial Approach to Computational Modeling of Beams Undergoing Finite Rotations", *International Journal for Numerical Methods in Engineering*, **41**, pp. 527-540.

[47] Hauptmann, R., Doll, S., Harnau, M., and Schweizerhof, K., 2001, "Solid-Shell Elements with Linear and Quadratic Shape Functions at Large Deformations with Nearly Incompressible Materials", *Computers and Structures*, **79**, pp. 1671-1685.

[48] Sharf, I., 1999, "Nonlinear Strain Measures, Shape Functions and Beam Elements for Dynamics of Flexible Beams", *Multibody System Dynamics*, **3**, pp. 189-205.

[49] Cook, R. D., 1981, *Concepts and Applications of Finite Element Analysis*, Wiley, New York.

[50] Bucalem, M. L., and Bathe, K.-J., 1995, "Locking Behavior of Isoparametric Curved Beam Finite Elements", *Applied Mechanics Reviews*, **48**, pp. 25-29.

[51] Reddy, J. N., 1997, "On Locking-Free Shear Deformable Beam Finite Elements", *Computer Methods in Applied Mechanics and Engineering*, **149**, pp. 113-132.

[52] Shabana, A. A., 1994, *Computational Dynamics*, Wiley, New York.

[53] ANSYS User's Manual, 2001, Theory, Twelfth Edition, SAS IP, Inc. ©.

[54] Dufva, K. E., Sopanen, J. T., and Mikkola, A. M., 2005, "A Two-Dimensional Shear Deformable Beam Element Based on the Absolute Nodal Coordinate Formulation", *Journal of Sound and Vibration*, **280**, pp. 719-738.

[55] Wu, S.-C., and Haug, E. J., 1988, "Geometric Non-linear Substructuring for Dynamic of Flexible Mechanical Systems", *International Journal for Numerical Methods in Engineering*, **26**, pp. 2211-2226.

[56] Berzeri, M., Campanelli, M., and Shabana, A. A., 2001, "Definition of the Elastic Forces in the Finite-Element Absolute Nodal Coordinate Formulation and the Floating Frame of Reference Formulation", *Multibody System Dynamics*, **5**, pp. 21-54.

[57] Simo, J. C., and Vu-Quoc, L., 1986, "On the Dynamics of Flexible Beam under Large Overall Motions – The Plane Case: Part II", *Journal of Applied Mechanics*, **53,** pp. 855-863.

[58] Berzeri, M., and Shabana, A. A., 2002, "Study of the Centrifugal Stiffening Effect Using the Finite Element Absolute Nodal Coordinate Formulation", *Multibody System Dynamics*, **7**, pp. 357-387.

[59] García-Vallejo, D., Mayo, J., Escalona, J. L., and Domínguez, J., 2004, "Efficient Evaluation of the Elastic Forces and the Jacobian in the Absolute Nodal Coordinate Formulation", *Nonlinear Dynamics*, **35**, pp. 313-329.

[60] Sugiyama, H., and Shabana, A. A., 2004, “On the Use of Implicit Integration Methods and the Absolute Nodal Coordinate Formulation in the Analysis of Elasto-Plastic Deformation Problems”, *Nonlinear Dynamics*, **37**, pp. 245-270.

[61] Dufva, K. E., Kerkkänen, K. S., Maqueda, L., and Shabana, A. A., “Nonlinear Dynamics of Three-Dimensional Belt-Drives Using the Finite Element Method”, *Nonlinear Dynamics*, in review.

[62] Gerstmayr, J., and Shabana, A. A., 2005, “Analysis of Thin Beams and Cables Using the Absolute Nodal Coordinate Formulation”, Technical report MBS05-3-UIC.

[63] Dufva, K. E., and Shabana, A. A., 2005, “Analysis of Thin Plate Structures Using the Absolute Nodal Coordinate Formulation”, *Proceedings of the Institution of Mechanical Engineers*, *Journal of Multi-body Dynamics*, **219** (K), pp. 345-356.

[64] Chia, C. Y., 1980, *Nonlinear Analysis of Plates*, McGraw-Hill, Inc., USA.

[65] Dmitrochenko, O. N., and Pogorelov, D. Y., 2003, “Generalization of Plate Finite Elements for Absolute Nodal Coordinate Formulation”, *Multibody System Dynamics*, **10**, pp. 17-43.

[66] Dufva, K. E., Sopanen, J. T., and Mikkola, A. M., ”Three-Dimensional Beam Element Based on a Cross-Sectional Coordinate System Approach”, *Nonlinear Dynamics*, in press.

ACTA UNIVERSITATIS LAPPEENRANTAENSIS

194. SALLINEN, PETRI. Modeling dynamic behavior in tilting pad gas journal bearings. 2004. 157 s. Diss.

195. HEILMANN, PIA. Careers of managers, comparison between ICT and paper business sectors. 2004. 262 s. Diss.

196. AHMED, MOHAMMAD. Sliding mode control for switched mode power supplies. 2004. U.s. Diss.

197. HUPPUNEN, JUSSI. High-speed solid-rotor induction machine – electromagnetic calculation and design. 2004. 168 s. Diss.

198. SALMINEN, PIA. Fractional slot permanent magnet synchronous motors for low speed applications. 2004. 150 s. Diss.

199. VARIS, JARI. Partner selection in knowledge intensive firms. 2004. U.s. Diss.

200. PÖYHÖNEN, AINO. Modeling and measuring organizational renewal capability. 2004. U.s. Diss.

201. RATAMÄKI, KATJA. Product platform development from the product lines´ perspective: case of switching platform. 2004. 218 s. Diss.

202. VIRTANEN, PERTTU. Database rights in safe European home: the path to more rigorous protection of information. 2005. 425 s. Diss.

203. Säädöksiä, systematiikkaa vai ihmisoikeuksia? Oikeustieteen päivät 19. – 21.8.2003. Toim. Marjut Heikkilä. 2004. 350 s.

204. PANTSAR, HENRIKKI. Models for diode laser transformation hardening of steels. 2005. 134 s., liitt. Diss.

205. LOHJALA, JUHA. Haja-asutusalueiden sähkönjakelujärjestelmien kehittäminen – erityisesti 1000 V jakelujännitteen käyttömahdollisuudet. 2005. 201 s., liitt. Diss.

206. TARKIAINEN, ANTTI. Power quality improving with virtual flux-based voltage source line converter. 2005. U.s. Diss.

207. HEIKKINEN, KARI. Conceptualization of user-centric personalization management. 2005. 136 s. Diss.

208. PARVIAINEN, ASKO. Design of axial-flux permanent-magnet low-speed machines and performance comparison between radial-flux and axial-flux machines. 2005. 153 s. Diss.

209. FORSMAN, HELENA. Business development efforts and performance improvements in SMEs. Case study of business development projects implemented in SMEs. 2005. 209 s. Diss.

210. KOSONEN, LEENA. Vaarinpidosta virtuaaliaikaan. Sata vuotta suomalaista tilintarkastusta. 2005. 275 s. Diss.

211. 3rd Workshop on Applications of Wireless Communications. 2005. 62 s.

212. BERGMAN, JUKKA-PEKKA. Supporting knowledge creation and sharing in the early phases of the strategic innovation process. 2005. 180 s. Diss.

213. LAAKSONEN, PETTERI. Managing strategic change: new business models applying wireless technology as a source of competitive edge. 2005. 142 s. Diss

214. OVASKA, PÄIVI. Studies on coordination of systems development process. 2005. U.s. Diss.

215. YANG, GUANGYU. Control and simulation of batch crystallization. 2005. U.s. Diss.

216. MUSTONEN–OLLILA, ERJA. Information system process innovation adoption, adaptation, learning, and unlearning: a longitudinal case study. 2005. U.s. Diss.

217. SAINIO, LIISA-MAIJA. The effects of potentially disruptive technology on business model – a case study of new technologies in ICT industry. 2005. 205 s. Diss.

218. SAINIO, TUOMO. Ion-exchange resins as stationary phase in reactive chromatography. 2005. 175 s. Diss.

219. CONN, STEFFEN. Software tools to support managers: development and application to new product development and strategic alliance management. 2005. 168 s. Diss.

220. TYNJÄLÄ, TERO. Theoretical and numerical study of thermomagnetic convection in magnetic fluids. 2005. U.s. Diss.

221. JANTUNEN, ARI. Dynamic capabilities and firm performance. 2005. 210 s. Diss.

222. KOLA-NYSTRÖM, SARI M. In search of corporate renewal: how to benefit from corporate venturing? 2005. 190 s. Diss.

223. SARÉN, HANNU. Analysis of the voltage source inverter with small DC-link capacitor. 2005. 143 s. Diss.

224. HUUHILO, TIINA. Fouling, prevention of fouling, and cleaning in filtration. 2005. U.s. Diss.

225. VILJAINEN, SATU. Regulation design in the electricity distribution sector – theory and practice. 2005. 132 s. Diss.

226. AVRAMENKO, YURY. Case-based design method for chemical product and process development. 2005. U.s. Diss.

227. JÄRVINEN, KIMMO. Development of filter media treatments for liquid filtration. 2005. U.s. Diss.

228. HURMELINNA-LAUKKANEN, PIA. Dynamics of appropriability – finding a balance between efficiency and strength in the appropriability regime. 2005. U.s. Diss.

229. LAARI, ARTO. Gas-liquid mass transfer in bubbly flow: Estimation of mass transfer, bubble size and reactor performance in various applications. 2005. U.s. Diss.

230. BORDBAR, MOHAMMAD HADI. Theoretical analysis and simulations of vertically vibrated granular materials. 2005. U.s. Diss.

231. LUUKKA, PASI. Similarity measure based classification. 2005. 129 s. Diss.

232. JUUTILAINEN, ANNELI. Pienen matkailuyrityksen yrittäjän taival. Oppiminen yrittäjyysprosessissa. 2005. 191 s. Diss.

233. BJÖRK, TIMO. Ductility and ultimate strength of cold-formed rectangular hollow section joints at subzero temperatures. 2005. 163 s. Diss.

234. BELYAEV, SERGEY. Knowledge discovery for product design. 2005. U.s. Diss.

235. LEINONEN, KARI. Fabrication and characterization of silicon position sensitive particle detectors. 2006. U.s. Diss.

236. DUFVA, KARI. Development of finite elements for large deformation analysis of multibody systems. 2006. U.s. Diss.

237. RITVANEN, JOUNI. Experimental insights into deformation dynamics and intermittency in rapid granular shear flows. 2006. U.s. Diss.